Onset of Glaciation seen at the contact of the Makganyene and Griquatown Formations, South Africa

---

A thesis submitted in fulfilment of the requirements for the degree of

Master of Science

at

Utrecht University, the Netherlands

Supervisor: Prof. dr. Paul Mason

Second Supervisor: Dr. Harilaos Tsikos

2023

Abstract

The ca. 2.4 Ga Makganyene Formation of the Postmasburg Group, South Africa contains diamictite rocks that, together with similar deposits from the Huronian Supergroup, potentially record a global Paleoproterozoic glaciation. Traditionally the basal contact of the Makganyene Formation has been interpreted as an erosional contact. However, there is increasing support for a conformable interpretation of the contact. The nature of this contact is critical for models that attempt to explain the processes responsible for the onset of the glaciation using geochemical variations in the underlying stratigraphy. In this thesis, I have investigated the nature of the Griquatown-Makganyene contact at four different locations sampled during diamond drilling. A combination of optical microscopy, Electron Dispersive X-ray Spectroscopy, and laser ablation ICP-MS was used to identify lithological and chemical changes on either side of the contact. Mineralogical, textural, and chemical results indicate the Makganyene Formation was formed by reworking of material from the Griquatown Formation in an environment similar to what the Griquatown Formation was formed in. The material that was reworked was potentially semi-consolidated. The findings are consistent with more recent views on the Griquatown-Makganyene contact and build upon those views to describe a better constrained depositional model for the Makganyene Formation.

Declaration

I hereby declare that this thesis with the title: "Onset of Glaciation seen at the contact of the Makganyene and Griquatown Formations, South Africa" is my own original work, and all sources have been acknowledged in a proper way.

Contents

Acknowledgements

Many projects are reliant on a group of people to be successful, and this project is no exception. First of all, I would like to give a big thank you to Paul and Hari for first of all considering me for this project, but also for all the expertise, and for giving me a push in the right direction when I needed it. I very much enjoyed working on this project. The findings opened up new ideas to work on, so I am a little sad that this project had to come to an end eventually.

The lab technicians Tilly, Helen and Eric were of tremendous help while using the equipment needed for the chemical analysis. I want to thank them for their explanations, and for all of the suggestions for fine tuning the methods.

This project could not have happened without any funding and the Olaf Schuiling fund made it all possible. With the funding it was possible to have thin sections made, and chemical analysis to be done on the samples, which was all essential for this project.

Lastly, I would like to dedicate a part to my most important influences that led me to pursue a study in Earth Sciences. One of my main influences are my parents who brought me along on vacations and trips. They always supported me with my education, and I fondly remember the moments with them trying to find minerals, panning for gold or beautiful hikes in Austria (Though at that age I could not yet appreciate the hiking and beauty of the Austrian Alps yet). At a young age there was an interest in Geology, and I am convinced that with such activities my parents only cultivated my interests, that led up to me pursuing a degree in Geology.

During the final stages of writing my trusty comrade and dog I had since the end of primary school, Rebel, sadly passed away. She would support me in her own way while I was working my way through school and university. Even in her final weeks she remained by my side for the occasional pets, giving me important breaks from the sometimes frustrating text and spreadsheet editing software. We shared many beautiful and adventurous moments that I will cherish forever. Rest in peace my friend.

1. Introduction

Evidence for a glaciation, immediately prior to the onset of the great oxidation event (GOE), is provided by the extensive deposition of tillite diamictites (Visser, 1971). These diamictites are found in the Makganyene Formation, belonging to the ca. 2.4 Ga Postmasburg Group from South Africa. The Makganyene Formation was deposited during the correspondingly named Makganyene Glaciation (Beukes, 1983). Knowledge on the Makganyene Glaciation and its cause is still underdeveloped, but it coincides with the Ramsay Lake Formation from the Huronian Supergroup in Canada (Gumsley et al., 2017), linking the Makganyene Glaciation to the Huronian Glaciation (Young & Long, 1976; Gumsley et al., 2017).

Several triggers have been proposed for the cooling of Earth's atmosphere, ultimately leading to global glaciation. These include: (1) Lowered atmospheric CO_2 as a result of large-scale weathering (Young, 1991; Melezhik, 2006), (2) methane elimination due to oxidation with O_2 produced following the evolution of oxygenic photosynthesis (Pavlov et al., 2000). (3) A collapse of a methane greenhouse that followed large scale burial of organic material (Schrag et al., 2002) (4) A decline in methane production as the result of a decline in ocean Ni concentrations (Konhauser et al., 2009) and (5) Widespread deposition of carbonate platforms (Moore et al., 2001).

Previously it was thought that the contact between the Makganyene Formation and the underlying Griquatown Formation is a major regional unconformity. This was partly based on the absence of the Koegas Subgroup that locally is present between the Makganyene and Griquatown Formations that presumably was removed by glacial erosion (e.g., Visser, 1971; Beukes, 1983). More modern insights have suggested the presence of a conformable contact based on textural and geochemical data (Moore et al., 2001; Polteau et al., 2006; Oonk, 2017; Siahi et al., 2020).

The Makganyene Formation is interpreted to be part of a global glaciation (Gumsley et al., 2017). However, we do not know what triggered the glaciation. Rocks from the Asbestos Hills Subgroup in South Africa that are situated directly underneath the Makganyene Formation potentially provide information about changing conditions immediately prior to the glaciation. A major problem is that we do not know if the contact is conformable or not. A conformable contact would enable changing chemical composition at the top of the

Asbestos Hills Subgroup to potentially be linked to processes that led to the glaciation, such as the major shift in Mn/Fe ratios seen in the uppermost part of the Griquatown Formation, as elsewhere in the Koegas Formation, immediately below the Makganyene Formation (Oonk, 2017). In this thesis the basal contact will be investigated to determine if it is conformable.

1.1 Geological background

1.1.1 Banded Iron Formations

James (1954) defined Banded Iron Formations (BIF) as a type of chemical sediment, typically thin-bedded or laminated, containing 15 percent or more iron of sedimentary origin, and commonly but not necessarily containing layers of chert. Typically, levels of detritus in BIF are expected to be low (Drever, 1974, Klein, 2005), as recorded by Al_2O_3 concentrations (<1
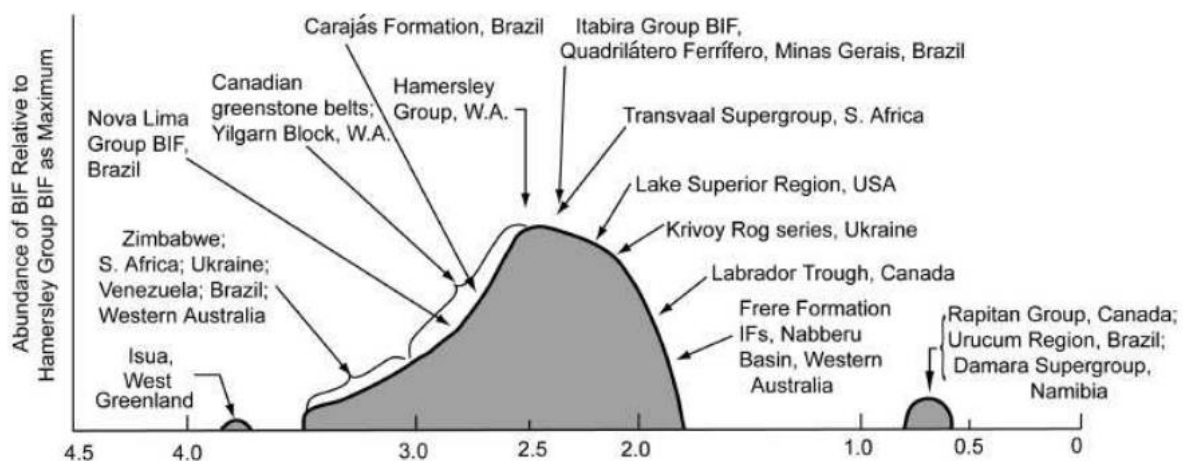
Figure 1 - Age and relative abundance of specific iron formations found around the world From Klein (2005).

wt%) (Planavsky et al., 2010). Texturally it is possible to characterize some iron formations as either banded (BIF) or granular iron formations (GIF). GIFs lack the characteristic banding and contain granules of IF forming minerals (Konhauser et al., 2017). Iron Formation rocks typically have a mineralogy containing around 50% iron oxides, which adds up to around 25% to 35% iron. The rest of the rock consists of mostly iron-carbonates and iron silicates. Minerals in IF are usually fine grained and concentrated in alternating bands of iron rich, and silica rich bands (Trendall, 2002).

1.1.2 Deposition

The oldest known BIF is found in the Isua Greenstone Belt on Greenland and has been dated at 3.7 Ga (Kamber et al., 2005). The deposition of the Hamersley Group in Australia and Transvaal supergroup in South Africa marks the period of peak BIF deposition around 2.5 to 2.4 Ga ago (Figure 1). After the deposition of these rocks, the relative abundance of IF started to decline and came to a near halt after about 1.7 Ga. BIFs were deposited again in the Neoproterozoic at around 0.7 Ga (Klein, 2005). Traditionally it is thought that the chert in IF is derived from a siliceous gelatinous precipitate (Ayres, 1972). BIFs most likely formed from either of two precursor phases (Konhauser et al., 2017). The first likely precursor phases are Fe(III)-oxyhydroxides formed by reaction with free O_2 or through the activity of iron oxidizing bacteria (Konhauser et al., 2002; Kappler et al., 2005). Bacteria are able to oxidize Fe(II) either through anoxygenic photoautotrophic ways (Kappler et al., 2005) or chemolithoautotrophic ways (Konhauser et al., 2005). The proposed reaction for anoxygenic photoautotrophic iron reduction is:

$$4Fe^{2+} + CO_2 + 11H_2O + h\upsilon \rightarrow [CH_2O] + 4Fe(OH)_3 + 8H^+ \text{ (Ehrenreich \& Widdel, 1994)}$$
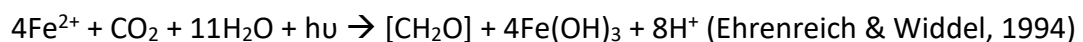
The reaction for the chemolithoautotrophic oxidation of Fe(II) is:

$$6Fe^{2+} + 0.5O_2 + CO_2 + 16H_2O \rightarrow [CH_2O] + 6Fe(OH)_3 + 12H^+ \text{ (Konhauser 2002).}$$
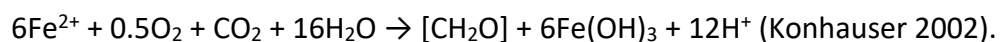
The oxygen required for the chemolithoautotrophic oxidation of Fe was most likely supplied by oxygen producing cyanobacteria which are likely to have evolved as early as 3 Ga (Cloud, 1973; Kaufman, 2014).

The second precursor phase stated as a likely precursor for the formation of BIFs is amorphous Fe(III)-Si. Fe(II) and Si nucleated in anoxic seawater to form silica nanoparticles that could function as nucleation sites for amorphous silica (e.g., Percak-Dennett et al., 2011; Rasmussen et al., 2015; Zheng et al., 2016)

Dodd et al. (2022) suggests an abiotic model for BIF production. In their model they argue for the precipitation of ferrous hydroxides, which decompose to a ferrous-ferric green rust.

Another abiotic model for oxidizing Fe involves UV-light. Either by direct Fe photo-oxidation (Cairns-Smith, 1978) or by the production of UV-derived oxidants (Pecoits et al., 2015). In the Cairns-Smith (1978) model, UV sunlight in the 200 to 300 nm range oxidizes Fe^{2+} in the

photic zone of the marine environment. The reaction looks as follows:

$$Fe^{2+} + 2H^+ + h\upsilon \rightarrow Fe^{3+} + H_2$$
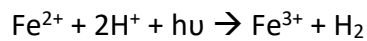
The Pecoits et al. (2015) model suggests that UV light formed hydrogen peroxide (H_2O_2) in a photochemical reaction. In turn, the H_2O_2 oxidizes Fe^{2+} through various possible reactions.

Another abiotic pathway for BIF deposition is the formation of ferrous-ferric hydroxy salts as a precursor phase, also known as green rust. These form in marine oxygen poor environments (Halevy et al., 2017). Halevy (2017) argues that green rust formation potentially had a major contribution to BIF deposition throughout the Precambrian.

Most pathways suggested for the formation of BIF suggest the presence of a precursor phase before the formation of typical BIF mineralogy. Biologically mediated precipitation of goethite or magnetite has been recognized in modern day Fe(II) oxidizing bacterial species (Jiao et al., 2005). Bauer et al. (2020) has demonstrated the reduction of biologically reactive Fe(III) mineral phases occurred in the water column to form primary magnetite.

Cyclicity was observed in the Precambrian Brockman Iron Formation more than 50 years ago (Trendall & Blockley, 1970). The cyclicity in the Kuruman Formation and Brockman Formation were recently shown to be linked to Milankovitch cycles for the first time. The 2.48 Ga Kuruman Formation shows signs of eccentricity cycles of 405 ka, and 1.4 to 1.6 Ma (Lantink et al., 2019). Additionally, patterns in the Brockman Formation were interpreted as cycles that have been linked to precession cycles (Lantink et al., 2023).

1.1.3 Mineralogy

The mineral assemblage typically found in the least metamorphosed types of BIF consist of magnetite and/or rare hematite as the iron oxide phases, microcrystalline quartz (chert), the carbonates ankerite and siderite, and iron silicates including greenalite, minnesotaite, stilpnomelane and riebeckite, plus rare pyrite (Klein, 2005). The most common primary precipitate is generally considered to be the Fe(III)-oxyhydroxides (Beukes & Gutzmer, 2008) that might be directly preserved as hematite (e.g., Morris, 1980; Sun et al., 2015). Some studies have reported primary siderite (Klein & Beukes 1989), or high-magnesium calcite as primary precipitates (Siahi et al., 2020). Common minerals present in BIF such as greenalite, stilpnomelane, riebeckite, ankerite and pyrite most likely formed during diagenetic and

metamorphic processes as the result of fluid flow and temperature and pressure increase (Klein, 2005; Konhauser et al., 2017).

1.1.4 Source of the iron

Iron formations required large quantities of Fe transported through the oceans to explain their widespread distribution (Konhauser et al., 2017). The soluble nature of Fe^{2+} at circumneutral pH and under anoxic conditions allows it to remain in solution and enables dispersal over large areas before being oxidized and precipitating as the Fe^{3+} phase ferrihydrite (Cloud, 1973). Hydrothermal and continental sources are proposed as the main suppliers of iron to the oceans (Konhauser et al., 2017). Early ideas included volcanic activity in and around the depositional basins (e.g., Trendall & Blockley, 1970), weathering of continental crust (Lepp & Goldich, 1964), or a deep-marine source of Fe (Holland, 1973). Nowadays it is generally accepted that the source of the iron in BIF was predominantly of hydrothermal origin (Isley, 1995; Konhauser et al., 2017). Holland (1973) argued for a deep-marine source for the Fe found in BIF. At the time calculations indicated this to be more plausible than a continental or volcanic source. Nowadays, a hydrothermal source for iron is widely accepted as the main contributor of Fe (Jacobsen & Pimentel-Klose, 1988; Isley 1995). Mantle plumes have been linked to BIF deposition based on the timing of mantle plume activity and peak BIF deposition (Isley & Abbott, 1999). Though hydrothermal activity is seen as the main source of iron, a continental input for BIF has been found in multiple BIFs (Haugaard et al., 2016; Li et al., 2015), indicating that the source can be mixed. Horstmann & Hälbich (1995) found that the Griquatown and Kuruman Formations, belonging to the Asbestos Hills Subgroup BIF were formed from Fe and Si supplied to the basin by hydrothermal sources. The overall Al_2O_3 content of the rock is low. However, Horstmann & Hälbich (1995) also reported elevated levels of Al_2O_3 in intercalated stilpnomelane lutites, which they link to intermittent clastic contamination. Or being derived from volcanic ash input (Beukes, 1980).

1.1.5 Great Oxygenation Event (GOE)
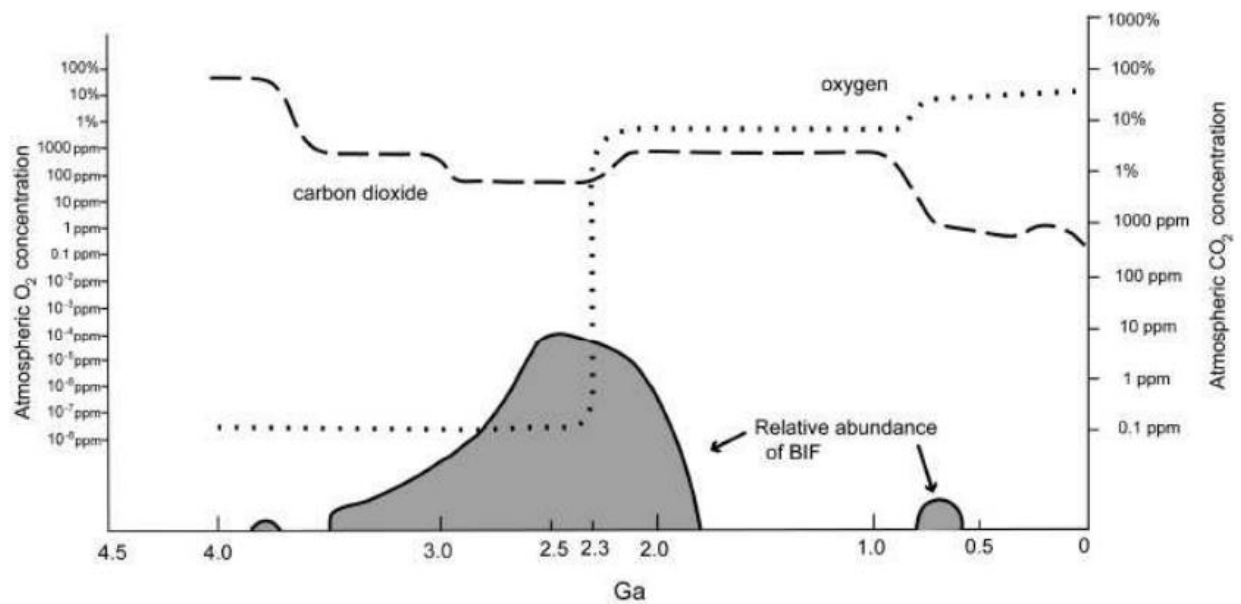
Figure 2 - Visualization of the oxygen and carbon dioxide concentration in the atmosphere with the relative abundance of Banded Iron Formations. From Klein 2005.

Between 2.460 to 2.426 Ga a major increase in oxygen on Earth occurred, now known as the Great Oxygenation Event (GOE) (Farquhar et al., 2000; Gumsley et al., 2017). The GOE is one of the most important events on Earth and saw a change from anoxic to oxygenic conditions in the atmosphere and oceans. This is seen in the loss of Mass-independent sulfur isotope Fractionation (Farquahar et al., 2000). The oxygenation of the Earth's atmosphere was a gradual process and continued until 2.060 Ga (Gumsley et al., 2017). The increase in oxygen is related to the increase in multicellularity and diversification rates of cyanobacteria (Schirrmeister et al., 2013). Three phases are recognized in the oxygenation of the Earth. The first phase is characterized by an anoxic environment. The second phase includes little oxygen in the atmosphere and surface waters. The third phase recognizes free oxygen in both the ocean and atmosphere systems (Karting, 1991).

Estimates of when the oxygenation of Earth started exactly is still debated. Different timings have been suggested. Different ways of constraining the onset of oxygenation on Earth give different timings. The oldest suggested timing of the GOE is 3.7 Ga. This suggestion is based on strongly fractionated C isotopes attributed to highly productive plankton, meaning that oxygenic photosynthesis had evolved by that time (Rosing & Frei, 2004). Research on the

redox-sensitive transition metals molybdenum and rhenium suggests 'whiffs of oxygen' around 2.5 Ga. The molybdenum is thought to be supplied to the oceans after being weathered on land under oxidative conditions (Bertine & Turekian, 1973; Anbar et al., 2007). Based on the fractionation of molybdenum as a result of adsorption to Mn, a timing of 2.95 Ga was found for the emergence of oxygen in shallow marine settings. In this case they looked at δ^{98}Mo values, which are close to -2.7‰ when adsorbed to Mn-oxyhydroxides, and -1.1‰ when adsorbed to Fe-oxyhydroxide (Planavsky et al., 2014).

The age of deposition of the Griquatown and Makganyene Formations occurred during the oxygenation of the Earth between 2.460 Ga and 2.060 Ga. Immediately prior to the main increase in oxygen (See Figure 2)(Nelson et al., 1999; Moore et al., 2012; Senger et al., 2023; Gumsley et al., 2017). The increase in oxygen on Earth could therefore be related to the temperature decrease leading up to the deposition of the Makganyene Formation. However, other evidence suggests that not only the increase in oxygen, but also a change in the carbon cycle could be the cause for global glaciation. This caused the Earth to transition from a CO_2 greenhouse to a less stable methane greenhouse (Schrag et al., 2002). Increasing oxygen levels prior to global glaciation caused the methane greenhouse to collapse (Kopp et al., 2005). However, the end of the global glaciation saw a cyanobacterial bloom, causing a drastic increase in oxygenation on Earth (Kirschvink et al., 2000).

1.1.6 Griquatown Formation

The oldest formation that will be examined in this project is the Griquatown Formation, dated as 2431 ± 31 Ma (Nelson et al., 1999). The Griquatown Formation is part of the Asbestos Hills Subgroup and is characterized by shallow-water sedimentation and has undergone little deformation since deposition. Three members are distinguished in the Griquatown Formation: The Danielskuil Member is the Lowest of the members, followed by the Skietfontein Member, and the Pietersberg Member on top (Beukes, 1983). Interbedding between orthochemical and allochemical iron formation units is seen in the Griquatown Formation. The Danielskuil and Skietfontein members are characterized by siderite and greenalite lutites that are interbedded with grainstone, grainlutite and disclutite. The Pietersberg member consists of chert bands containing greenalite lutites, grading upwards into chloritic claystones, siltstones and quartzwacke (Beukes, 1984). Most of the Mn present in the Griquatown Formation is hosted by carbonates (Johnson et al., 2013). This increase in

Mn has been linked to the increase in oxygen production. Manganese carbonates are formed in the oxygenated surface waters and deposited under anoxic conditions below the chemocline (Calvert & Pedersen, 1996). Stilpnomelane has been shown to host Mn as well, but in significantly smaller concentrations. (Oonk et al., 2017)

Prior research on carbonates from the Griquatown Formation has indicated the presence of the so-called High-Magnesium Calcite (HMC) in the AARPAN and ERIN cores. These HMC minerals are characterized by Mg contents of around 10%, while the Ca and Mn contents show a negative correlation. In Backscattered electron images these HMC minerals often show a lighter rim of angular ankerite around the rounded HMC core (Figure 3) (Siahi et al., 2020).
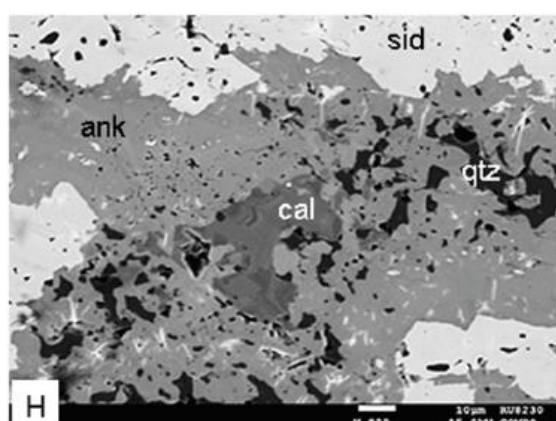

Figure 3 (left) - High-magnesium calcite replaced by ankerite. From Siahi et al. (2020)

Figure 4 (right) - Exposed lithologies of the Transvaal Supergroup. The colored dots indicate the locations for the HEX, ERIN, AARPAN, and LONDON drill cores used for this project. From Tsikos et al. (2022)
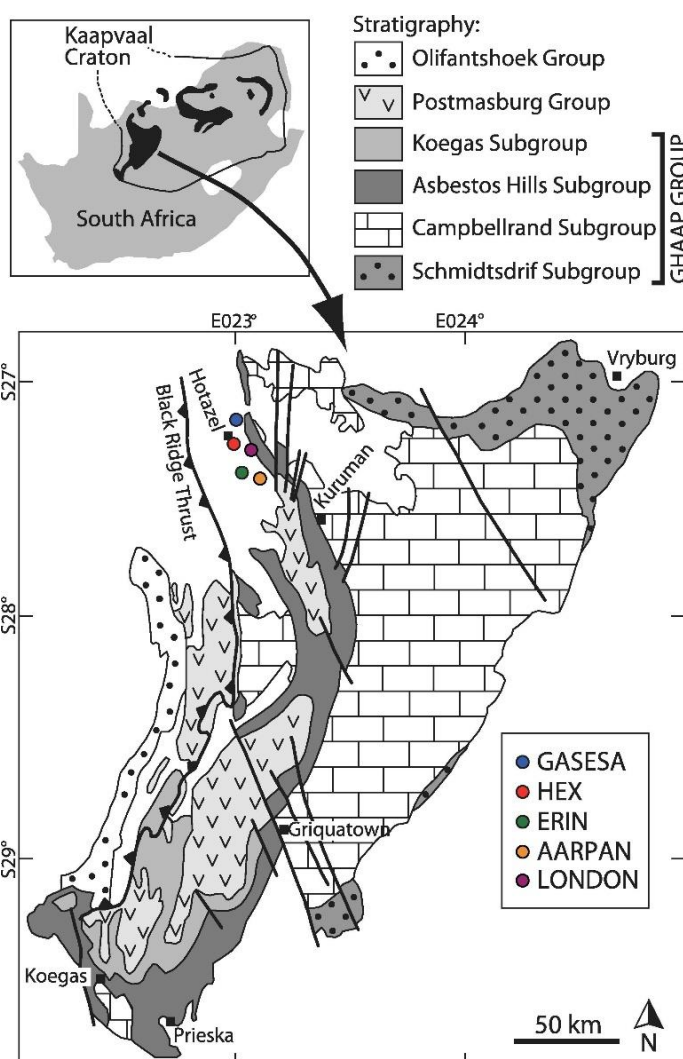
1.1.7 Koegas Subgroup

The Koegas Subgroup is only observed south of the Griquatown Fault Zone, between the towns of Koegas and Griquatown, see Figure 4. Rocks in the Koegas consist of deltaic chloritic claystones, siltstones and quartzwackes. The U-Pb zircon age determined from tuff beds in the Koegas Subgroup yielded a maximum age of deposition around 2415 ± 6 Ma (Gutzmer & Beukes, 1998). The Koegas is often stratigraphically depicted as being deposited between the Griquatown and Makganyene Formations (Beukes, 1983). However, the Griquatown Formation and Koegas Subgroup might have a lateral correlation. The presence of Mn in both the Griquatown Formation and Koegas Subgroup might be evidence for synchronous deposition (Siahi et al., 2020). The evidence for the synchronous deposition includes the mineral content of the Formations (Beukes, 1984), presence of glacial diamictite lenses in the Koegas Subgroup (Polteau et al., 2006), and the high Mn content that is common to the upper Griquatown and Koegas Subgroup (Siahi et al., 2020).

1.1.8 Makganyene Formation

The Makganyene Formation directly overlies the Griquatown Formation in areas where the Koegas Formation is not present (e.g., Polteau et al., 2006; Oonk, 2017), and belongs to the Postmasburg Group (Moore et al., 2012). The Makganyene Formation has a glacial origin as supported by textural evidence and structures related to deposition at ground zone wedges. Evidence for these ground zone wedges were found in the HEX core, which is one of the cores partly analyzed during this project (Visser, 1971; Le Heron et al., 2022). A combination of CA-ID-TIMS on LA-ICP-MS analysis on detrital and volcanic zircons estimated the age of the Makganyene Formation to be 2423 ± 1 Ma and belongs to the Postmasburg Group (Senger et al., 2023).

The formation is described as containing shale, mudstone, limestone, and chert, interbedded with diamictite and stromatolite bioherms (Polteau et al., 2006). Coarsening upward motifs in the Makganyene diamictite represent a complex development of an ice grounding zone wedge (Le Heron et al., 2022). The thickness of the Makganyene Formation varies greatly from 3 m to up to 500 m depending on the location (Visser, 1971; Moore et al., 2001; Polteau et al., 2006). The Makganyene Formation is overlain by the volcanic Ongeluk Formation. Originally, the Makganyene Formation was deposited on the Kaapvaal Craton. At the time of deposition, the Kaapvaal Craton was situated at a paleolatitude of

around 11 ± 5° (Evans et al., 1997). The low paleolatitude is one of the main pieces of evidence to argue for global glaciation happening during the deposition of the Makganyene Formation (Gumsley et al., 2017).

A prior report on the origin of the clasts in the Makganyene formation suggests these clasts are mainly derived from Asbestos Hills Subgroup BIF (Polteau et al., 2006). But more chemical data could potentially narrow this down to specific formations.

1.1.9 Paleoproterozoic glaciation

Indications for glaciations on Earth can be traced back as far as 2.9 Ga in the Pongola Supergroup of the Kaapvaal Craton in South Africa. These glacial deposits are often identified by dropstone textures around clasts (Thomas & Summers, 1981), faceted or striated clasts related to the transport of the clasts by the ice sheet (Von Brunn & Gold, 1993).

The cause for the glaciation in the Pongola Supergroup has been accounted to be the drawdown of CO_2. Newly forming cratons underwent significant amounts of weathering, and in turn causing enough drawdown of CO_2 out of the atmosphere to reduce Earth's greenhouse effect. This reduced greenhouse effect triggered low enough temperatures for glaciation to develop (Young, 1991; Young et al., 1998).

Many other causes for glaciation have been proposed and can range from processes on Earth to extra-terrestrial causes. Steiner & Grillmair (1973) give a few different extra-terrestrial causes for glaciations on Earth. The main cause given involves solar orbital motions parallel to the galactic plane (The plane containing the majority of a galaxy's mass). This is seen as a basic trigger mechanism for glacial episodes with a periodicity of between 0.16 and 0.4 Ga. A different mechanism involves solar orbital motion perpendicular to the galactic plane. In itself the perpendicular motion will not cause glaciations but can operate as a reinforcing mechanism. Different extra-terrestrial causes can include Milankovitch cycles (e.g., Imbrie et al., 1992; Markonis & Koutsoyiannis, 2013).

Terrestrial causes given include large scale (explosive) volcanism releasing enormous dust clouds into the atmosphere. The dust clouds block incoming solar radiation, causing a cooling effect at Earth's surface (Rampino & Self, 1992). However, volcanic eruptions can also erupt large amounts of CO_2 into the air, increasing the greenhouse effect and producing

an opposite warming effect. The deposition of large carbonate platforms has been suggested as a mechanism to draw down CO_2 from the atmosphere (Roberts, 1976). Large carbonate platforms deposited around 2.65 to 2.50 Ga such as the Malmani and Cambellrand Subgroups have a size large enough to be considered a major sink for CO_2 (Moore et al., 2001).

Instead of the CO_2 drawdown by weathering carbonate rocks, silicate rocks can also draw down a significant portion of CO_2 out of the atmosphere. The weathering rate is a function of temperature and will therefore be lower at high latitudes. When massive landmasses are concentrated at low latitudes, these weathering rates can become significantly higher. The cause for glaciation is therefore more dependent on the arrangement of continents, air and ocean currents. Rather than extra-terrestrial influences, which is more probable to cause glacial stages (Crowell, 1978; Marshall et al., 1988; Dessert et al., 2003; Melezhik, 2006). These 'forward weathering' reactions can also be muted due to 'reverse weathering' reactions that consume bicarbonate, metal hydroxides, cations and silica and produce cation-poor clays and CO_2. Reverse weathering is thought to have contributed to climate stability by buffering changes in $p$$CO_2$ (Isson & Planavsky, 2018).

1.1.10 Makganyene glaciation

The Makganyene Glaciation has been suggested to be a low latitude glaciation, based on paleomagnetic data of the conformally overlying Ongeluk volcanics (Evans et al., 1997). At the time of glaciation, deposition of the glacial diamictite took place at latitudes of around $11 \pm 5°$. The Makganyene glaciation has been correlated to the Huronian Ramsay Lake Formation. This suggests that the Makganyene glaciation is part of the snowball Earth event (Kirschvink 1992; Kirschvink et al., 2000; Gumsley et al., 2017). Mechanisms that triggered the Makganyene glaciation are poorly constrained. The main change in environmental conditions prior to the Makganyene glaciation is possibly the emergence of an oxygenated atmosphere prior to glaciation (Kopp et al., 2005). This is indicated by the disappearance of Mass-independent fractionation of sulfur (MIF-S) (Farquhar et al., 2000; Hoffman, 2013).

The emergence of cyanobacteria prior to the Makganyene glaciation is given as a reason for the emergence of free atmospheric oxygen. Oxygen is thought to have reacted with methane in the atmosphere to form water and CO_2 through the reaction of:

$$CH_4 + 2 O_2 \rightarrow CO_2 + 2 H_2O$$
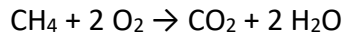
Thus, eliminating a strong greenhouse gas to form a weaker greenhouse gas. The result would have been a lowering of the temperature on Earth (Kirschvink, 2005).

2. Method

2.1 Sample description

Four diamond drill core samples, produced during exploration activity in Hotazel, South Africa were used in this study, the locations are given in Figure 4. These drill cores are named AARPAN, ERIN, HEX and LONDON. The drill core samples are each approximately 40 cm long and intersect the contact between the Griquatown and Makganyene Formations. The Griquatown-Makganyene contact in the AARPAN core sample is at a depth of 483.1 meters. In the ERIN core the contact is found at 367.5 meters. For the HEX core a range of 646.45 to 646.90 meters is give for the contact. The depth of the contact in the LONDON core is not provided with the samples. In all of these cores, the contact was intersected well-below the surface weathering horizon.

Photographs of the drill cores were taken prior to cutting (Appendix I) Thin sections were then made across what was identified as the contact between the Griquatown and Makganyene Formations (Appendix III). For locations of the thin sections I would like to refer to Appendix VII.

2.2 Data Collection

2.2.1 Computer tomography

Computer tomographic scans (CT scans) of the drill cores were made using the medical CT scanner in the Earth Simulation Lab of Utrecht University. Images are in grey scale from black to white, representing increasing radiodensities. In general materials with a relatively high radiodensity are iron oxides, minerals like carbonates and quartz generally have a

lower radiodensity. The program used for the imaging of the CT scans is the Weasis Medical Viewer software. Weasis Medical Viewer was able to show slices of the drill cores over 3 different axes. To be able to compare the drill cores a standard brightness and contrast setting was used. For that, a custom preset was created with window/level settings of 9000/5000.

2.2.2 Optical microscopy

The first step in analyzing the samples was transmitted light optical microscopy. For that a total of 25 thin sections were made that capture regions of interest in the samples. The mineralogy of the drill cores was determined from the thin sections using optical microscopy, as well as photomicrographs of structures and minerals were made. Digital scans of all thin sections were made.

2.2.3 Energy dispersive X-ray spectroscopy (EDS)

Mineral chemical microanalysis was conducted using Energy Dispersive X-Ray Spectroscopy (EDS) with a JEOL JXA 8530F Electron Probe Microanalyzer. EDS provided a quick and easy overview of the Mn content and changes in the samples. The EDS analysis was done at a voltage of 15 kV, the probe current was 17 nA. If possible multiple crystals were analyzed at the top, middle, and bottom of the thin section. Mainly carbonate phases were targeted using EDS. Values for element oxides gathered with EDS were automatically normalized to 100%, only counting the cation part of the mineral phases. The values for element oxides were only calculated after they were automatically detected by the software, or after manual selection. Main carbonate phases expected in the samples were calcite, dolomite, ankerite, and siderite. Therefore, Ca, Mg, Mn and Fe were manually selected, if not already detected, for every carbonate mineral that was analyzed.

Greenalite and stilpnomelane can both have a green colour in transmitted light microscopy depending on the redox state of the iron in stilpnomelane (Oonk, 2017). Because the minerals have a different chemical composition it was possible to identify the minerals using EDS analysis.

2.2.4 Laser ablation ICP-MS

Bulk compositions of clasts in the Makganyene Formation were estimated using Laser ablation ICP-MS. This analysis was conducted using a ThermoFischer Scientific Element 2

magnetic sector ICP-MS. The laser used for ablating the samples was a Lambda Physik Excimer laser. During the 2-day analysis a change in the settings was implemented as a result of ablating the material too fast during the first day. During the first day the laser was set to 26kV at 10 Hz. Setting the laser to 23 kV and 7 Hz proved to be more suitable for the soft material in the samples. Most measurements were not used due to too low scan counts that reduced the reliability of the measurement. This problem was partly caused by the thin sections being too thin for LA-ICP-MS. Only measurements with scan counts of 30 and up were used for plotting and calculating. Additionally, chert measurements were often incomplete and produced strange signatures. In most cases it was unclear if these measurements failed, and a glass signature was shown. In these cases, the measurements were also scrapped from the figures and calculations but will of course be present in Appendix V. Shale normalization was done using Post Archean Average Shale (PAAS) values from Bolhar et al. (2005). Microscopic observations have led to the suspicion that the matrix of the Makganyene Formation part of the AARPAN core was replaced by chert and calcite due to secondary veining. Therefore, no chemical analysis was done on this part as it would most likely not have provided data useful for this research.

2.3 Evaluation

Minerals such as quartz and stilpnomelane were readily identified by optical microscopy. In contrast, it was not possible to identify specific carbonate, iron silicate, and sulfide species using optical microscopy. Electron microprobe EDS analysis made discrimination possible for these phases. Carbonates were readily distinguished based on their Ca, Mg, Mn and Fe contents reflecting variable amounts of calcite, ankerite, and siderite. Iron silicates by the K, Na, and Ca content, and sulfides by the amount of Cu.
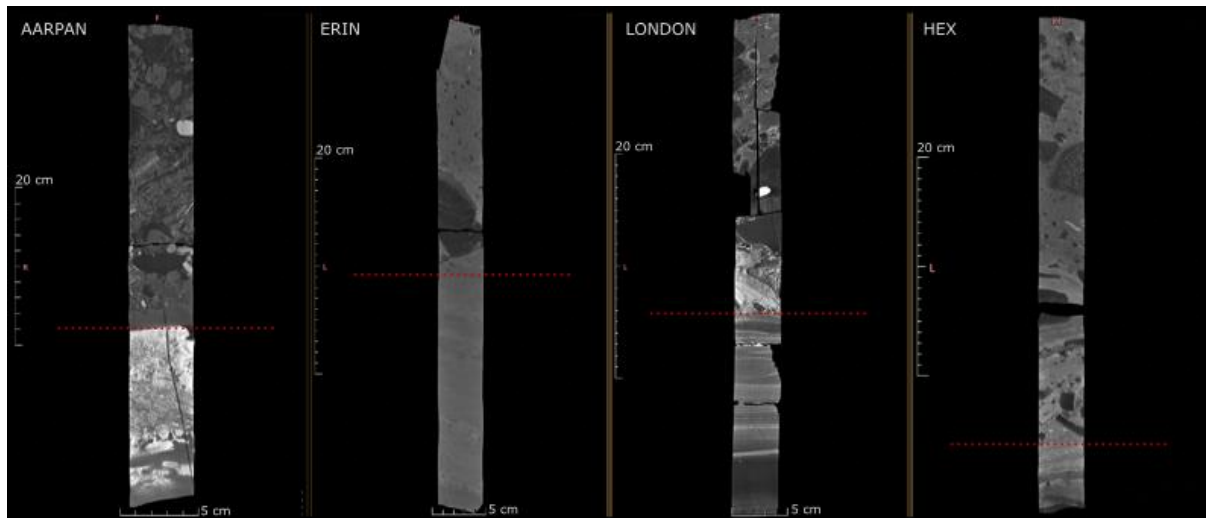
Figure 5 - whole scans of the AARPAN, ERIN, LONDON, and HEX cores. Brighter parts have a higher radiodensity. The brighter parts are generally richer in iron oxides. The red dotted lines indicate the proposed Griquatown-Makganyene contact.

3. Results

3.1 CT scans

Scans of the drill cores can be seen in their entirety in Figure 5. The scans show the different nature of the drill cores. A more detailed description of each drill core is given in the following sections.

3.1.1 AARPAN CT scan

The CT scan of the AARPAN core shows a clear difference in radiodensity between the upper part (Makganyene Formation) that appears darker, and the lower part (Griquatown Formation) that appears lighter (Figure 5). The radiodensities within the upper and lower parts are heterogeneously dispersed. In the Makganyene part, the heterogeneously dispersed radiodensities are mostly seen in the form of different radiodensities of clasts present in that section.

The Griquatown part of the AARPAN scan shows a heterogeneous, but overall radio denser character compared to the upper part of the drill core. Two less radio dense (sub)-horizontal bands in the lowest 3 cm of the core and a vein running diagonally through the core are observed.

A CT cross section at the contact between the radio dense and radiolucent part shows that the contact is not sharp. But rather shows a more irregular contact (Figure 6).
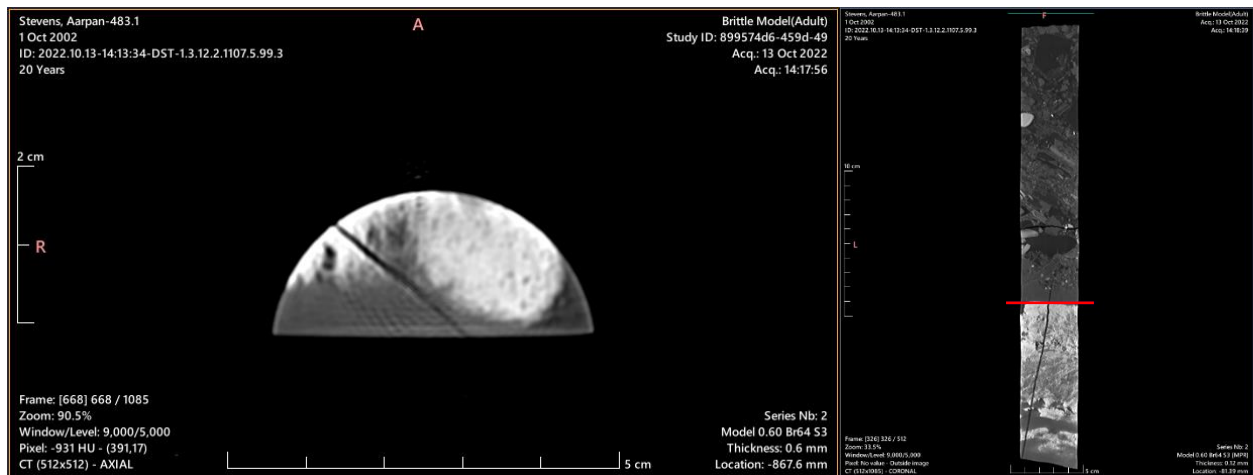
Figure 6 - Cross section of the AARPAN CT scan (left image). The cross section is taken at the contact indicated with the red line (right image).

3.1.2 ERIN CT scan

The CT scan of the ERIN core shows a minimal difference in the radiodensity between the lower and upper parts. The matrix is filled with smaller clasts of approximately 5 mm, with a bigger clast approximately halfway where the core is also fractured.

There is little difference in radiodensities in the matrix. Radiodensities in the clasts vary from a lower to higher radiodensity than the matrix. The larger clasts generally show a lower radiodensity than the matrix. Clasts with a higher radiodensity are present but are generally smaller in size than the other clasts.

3.1.3 HEX CT scan

The radiodensity of the HEX core matrix is highest in the lower part of the drill core. But can differ between smaller layers of the matrix. The clasts in the HEX core differ from low to moderate radiodensity, not reaching the high radiodensity of the iron oxides. The CT scans show layers bending around the clasts (Figure 7). The whole scan is given in Figure 5.
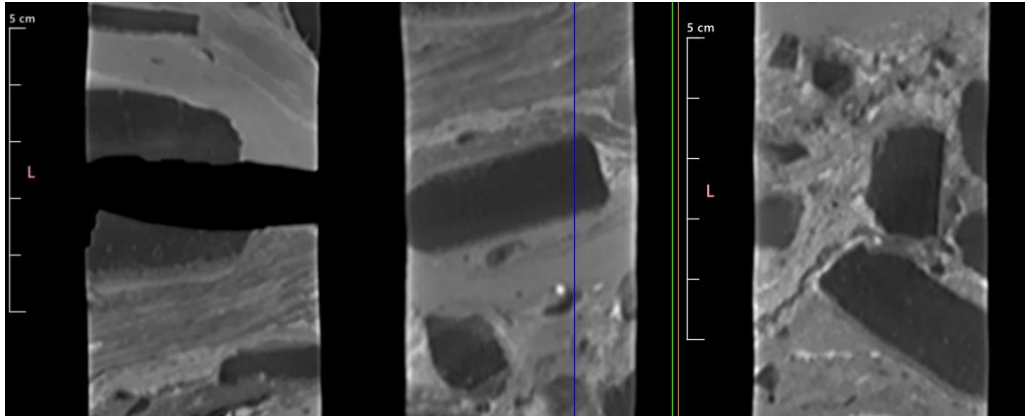
Figure 7 - CT scans showing clasts in the HEX core. The matrix around the clasts is distorted.

3.1.4 LONDON CT scan

The CT scan of the LOS core shows a fine-grained matrix containing clasts with varying sizes and radiodensities (Figure 8) in the upper part of the core. The middle part shows vertical fold-like structure and a homogeneous distribution of the radiodensity that mostly follows the layers. This layer is also more radio dense compared to the overlying diamictite, and the underlying fine-grained layers.

The lower part of the core shows clear (sub)-horizontal banding shown as layers with varying degrees of radiodensity. A cross section at the contact between the fine-grained rock and the diamictite reveals an irregular contact between the two lithologies. One of the clast pokes through the contact into the fine-grained matrix of the underlying BIF.
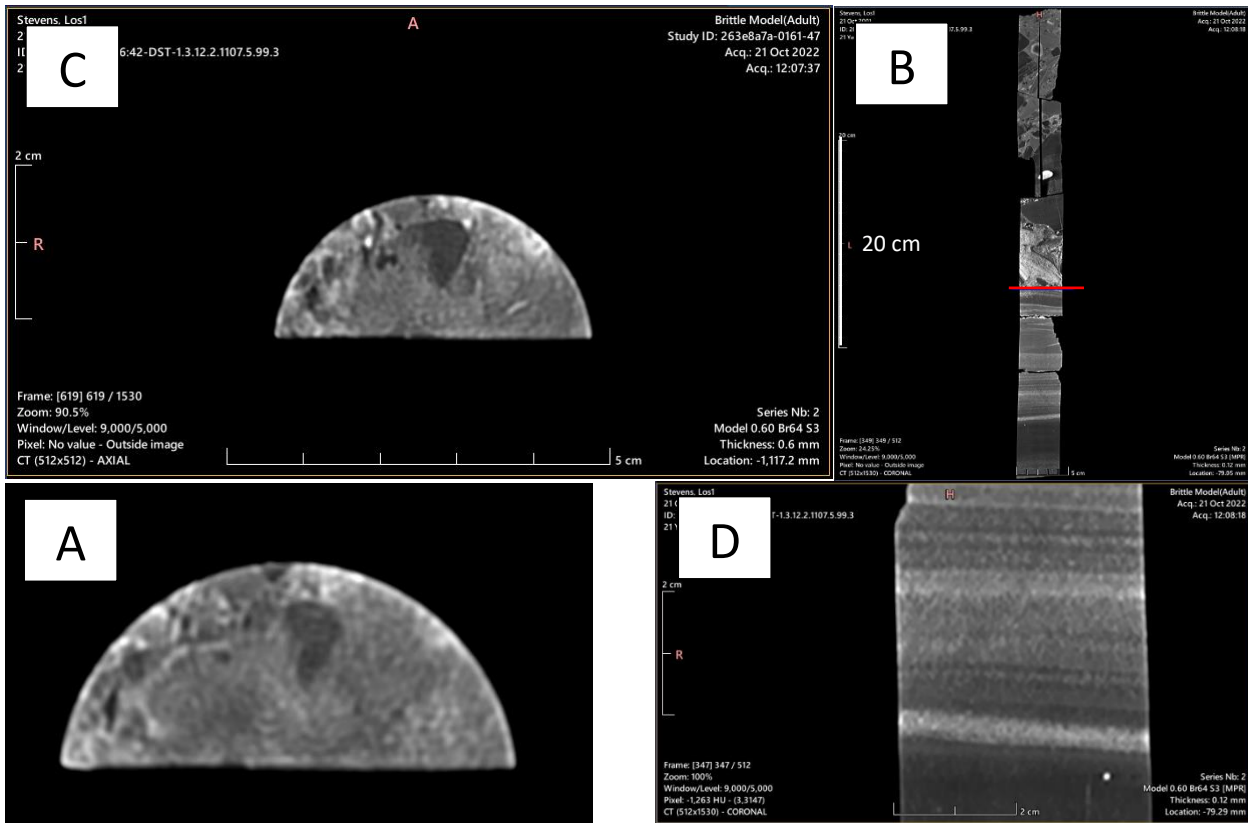
Figure 8 - CT scans of the LONDON core. A) darker clast piercing through the Griquatown/Makganyene contact B) Whole scan of the LONDON core with a red line at the slice of image A. C) Another slice at a different depth of the clast piercing through the contact. D) Banded and clast poor bottom part of the LONDON sample.

3.2 Mineralogy

Phases found in the cores are mainly stilpnomelane, quartz, and carbonates. Carbonates could not be readily distinguished based on petrographic microscopy. As the EDS data shows later in this section, the composition of the carbonates varies greatly, and most carbonates coexist within the same matrix. The opaque phases are mainly magnetite and small amounts of pyrite. A green mica is also often seen in the carbonate rich layers. However, all four drill cores show differences. More detailed descriptions of the mineralogy in the individual drill cores are given in the following sections. Scans of all thin sections are shown in Appendix III.

3.2.1 AARPAN core

The matrix of the Makganyene Formation of the AARPAN core (Thin sections 1, 2 and 3) consists of chert and calcite. Clasts found in thin sections 1, 2 and 3 consist of primarily chert and carbonates. Some clasts contain stilpnomelane in varying degrees, with few clasts consisting of only stilpnomelane. Some clasts in the Makganyene Formation of the AARPAN core show calcite matrix material through the clast. This can be seen as the calcite twinning lamellae with same orientations in the matrix crossing the clast material (Figure 9). The Griquatown part of the AARPAN core (Thin sections 3, 4, and 5) mainly consists of (dark) brown and grey layers. Brown layers are rich in stilpnomelane, the dark brown layers often contain mostly of opaque minerals, which are identified as mainly magnetite, and stilpnomelane. The grey layers have a carbonate rich matrix that contains minor amounts of opaque minerals and a green mica that is also likely to be stilpnomelane. A fracture can be traced through the drill core that crosses all 5 AARPAN thin sections. The fracture in the drill core consists of carbonates and quartz.

3.2.2 ERIN core

The Makganyene Formation of the lower part of the ERIN core shows a stilpnomelane-rich matrix filled with various types of clasts (Thin sections 6 and 7). Few opaques are observed in the matrix. Clasts found in this drill core mainly consist of carbonate minerals. A few clasts are made of chert, and combined carbonate and chert are also found. The basal part of thin section 8 contains small clasts that are scattered around the matrix. A part of a bigger clast is found at the top of thin section 8. Going up the stratigraphy from thin section 8 to 6, an increase in the packing density of the clasts is seen. The Griquatown part of the ERIN core (thin sections 9, 10, and 11) mainly consists of carbonate rich material containing stilpnomelane, quartz and small amounts of opaques. In the thin sections, stilpnomelane rich parts are interfingered with the carbonate rich parts.
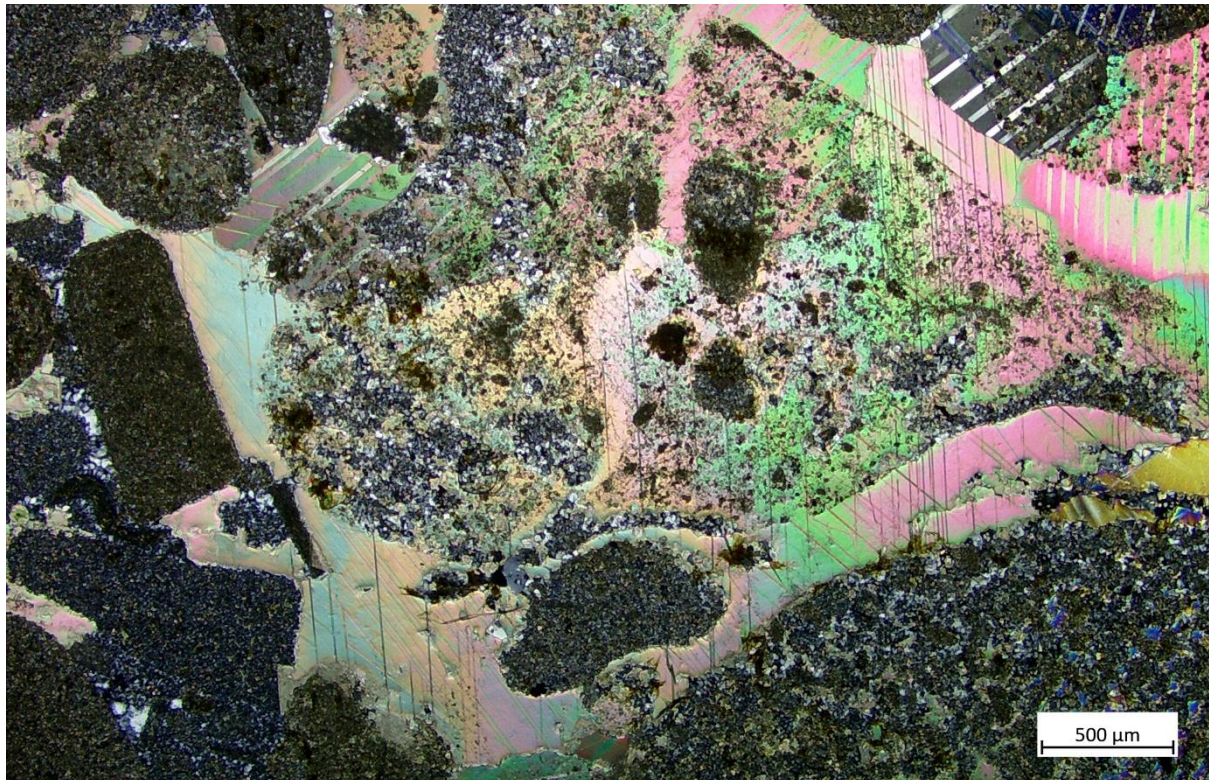
Figure 9 - Calcite matrix in the AARPAN core, also incorporated into a clast containing chert and stilpnomelane.

3.2.3 LONDON core

Thin sections 12 and 13 are densely packed with a variety of clasts, consisting of chert and mixed carbonate, as well as chert stilpnomelane. In addition, thin section 12 contains a clast with carbonate rich bands that contains stilpnomelane, quartz and opaques. Thin section 14 contains a large clast at the top covering approximately a third of the thin section, and a patch of clasts at the bottom of the thin section. The rest of the thin section is mostly made up of a stilpnomelane and carbonate matrix. Thin section 15 contains one layer with clasts, the bands show different compositions of stilpnomelane-rich lithologies with opaques, quartz, and carbonates. At the base of thin section 15 some chalcopyrite was identified. The banding continues in thin sections 16 and 17. Thin section 16 contains only stilpnomelane rich bands with opaque minerals and varying quartz and carbonate content. A major part of the matrix consists of stilpnomelane in thin sections 12 to 16. Thin section 17 contains significantly less stilpnomelane as thin section 16 and contains a few quartz rich layers with varying carbonate, opaque and stilpnomelane content.

3.2.4 HEX core

Thin sections from the HEX core show clasts in thin sections 18 to the top part of thin section 24. The clasts mainly consist of chert and carbonate, with varying degrees of stilpnomelane. In addition to the chert, carbonate and mixed clasts, also single crystal quartz clasts are found. The single crystal quartz crystals are less common in the other 3 drill cores. Thin sections 18, 19 and 20 mainly have a carbonate matrix with patches of stilpnomelane, with an occurrence of pyrite in thin sections 19 and 20. Going down the stratigraphy, thin section 21 shows the first signs of banding in the piece of the HEX core. However, these bands are irregular and wavy. Most bands in thin sections 21 to 24 mainly consist of carbonates with varying opaque, stilpnomelane and quartz and opaques content. Thin section 25 contains mostly chert bands with varying opaque, carbonates and stilpnomelane content.

3.3 EDS data

Carbonates throughout the drill cores show varying compositions (Figures 10 and 11). that can be classified into four compositional groups. The first group consists of carbonate with a high Ca content of around 80% to 90%. These are mainly found in the matrix of thin sections 1 and 2, corresponding to the Makganyene Formation of the AARPAN core. The second type contains high amounts of Fe. The mass percentage of Fe in these carbonates goes up to around 80%. Most of the remaining cations are Ca, Mg and Mn. A third carbonate group contains around 50% Ca, and can have Fe contents around 35%, Mg around 11% and Mn contents usually stay below 10%. However, Mn contents in the carbonates of the AARPAN core are exceptionally high compared to the LONDON, HEX and ERIN cores (Figures 12 and 13), and in a few instances exceeded the 18%. The fourth type of carbonate found in the drill cores has a calcium content of around 60% and will have a magnesium content of around 30 to 40%. These carbonates usually contain a rim of a carbonate mineral with a composition of the third type (Figure 14). In backscattered electron images, these minerals can be identified by a darker colour in the middle of the grain and a lighter rim. The compositions found with EDS analysis suggest the carbonate phases in the drill cores are mainly ankerite and siderite, with more minor amounts that have a dolomitic composition and, in some instances, (nearly) pure calcite.
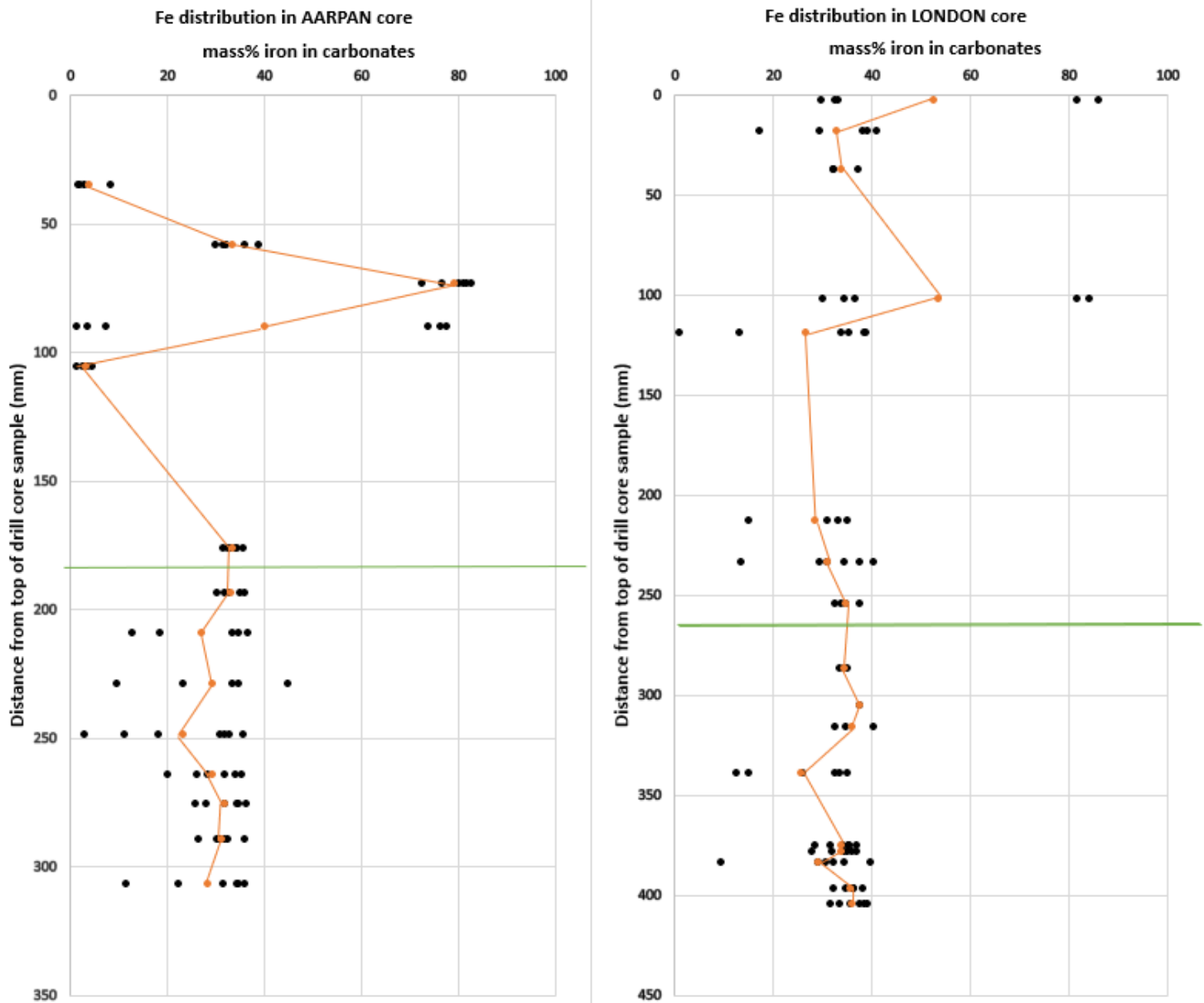
Figure 10 - Iron content of carbonates in the drill cores. Average values are given in orange. The green line represents the proposed Griquatown-Makganyene contact. Cation wt% data is normalized to 100%
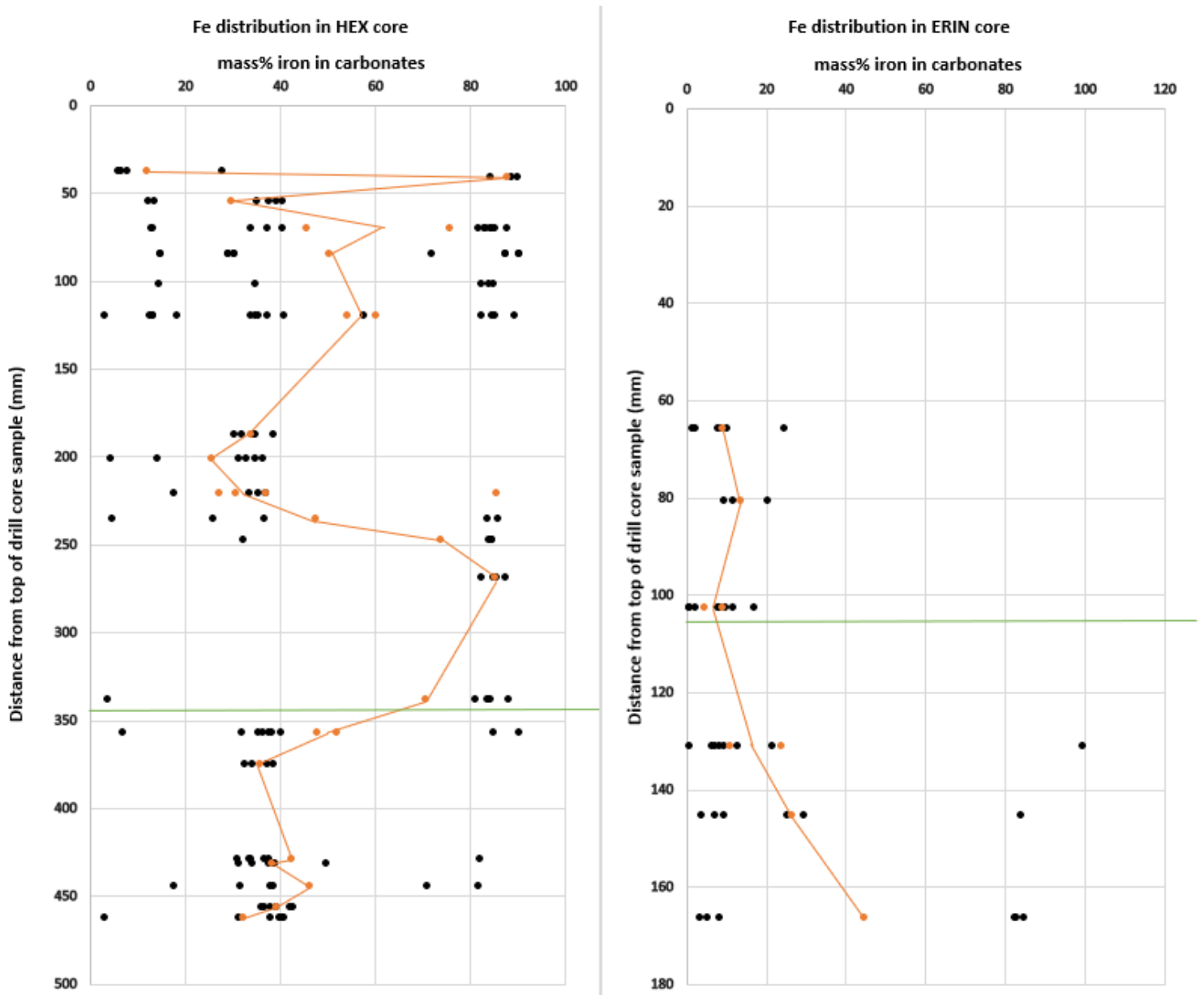
Figure 11 - Iron content of carbonates in the drill cores. Average values are given in orange. The green line represents the proposed Griquatown-Makganyene contact. Cation wt% data is normalized to 100%
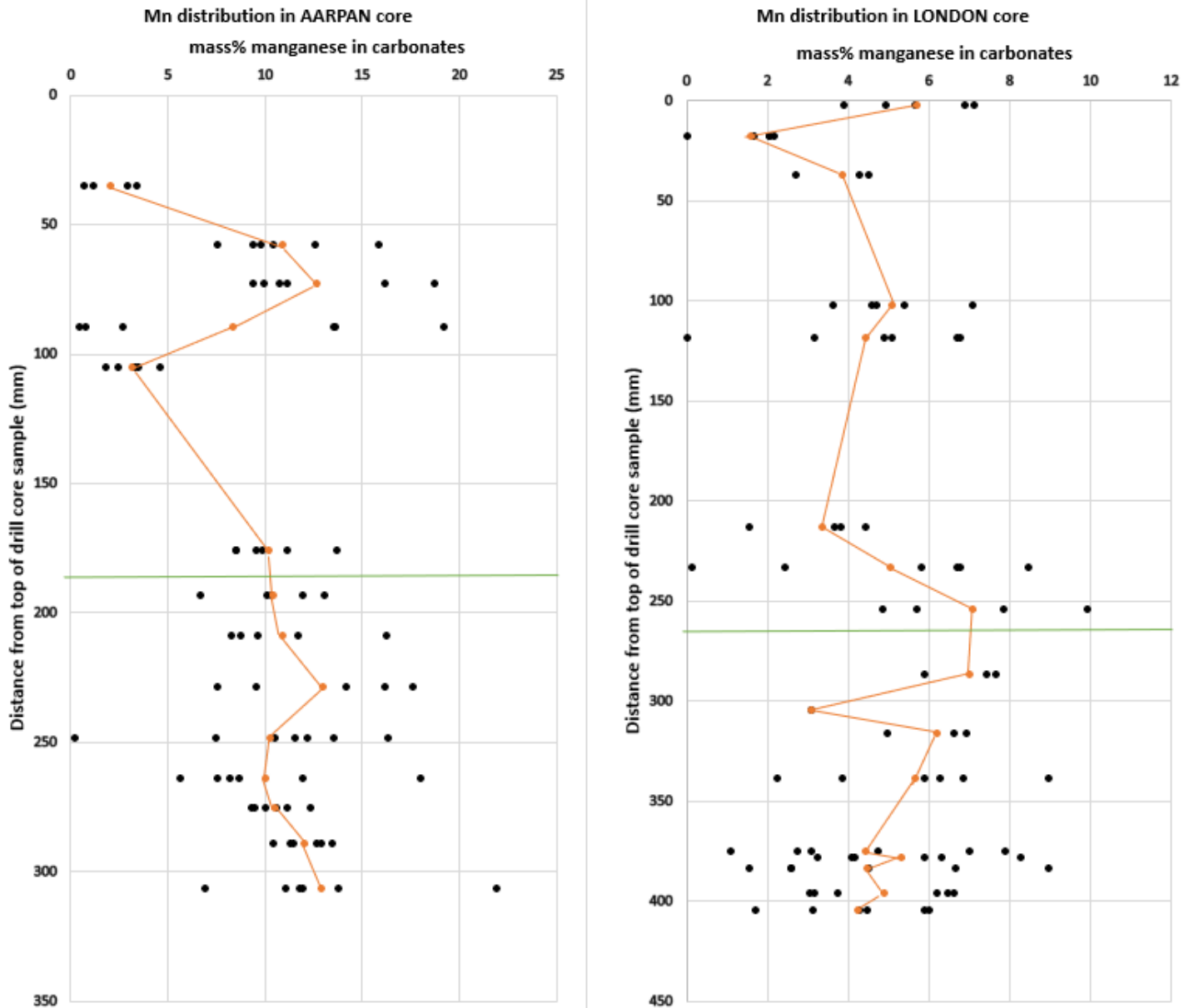
Figure 12 - Manganese content of carbonates in the AARPAN and LONDON drill cores. Average values are given in orange. The green line represents the proposed Griquatown-Makganyene contact. Cation wt% data is normalized
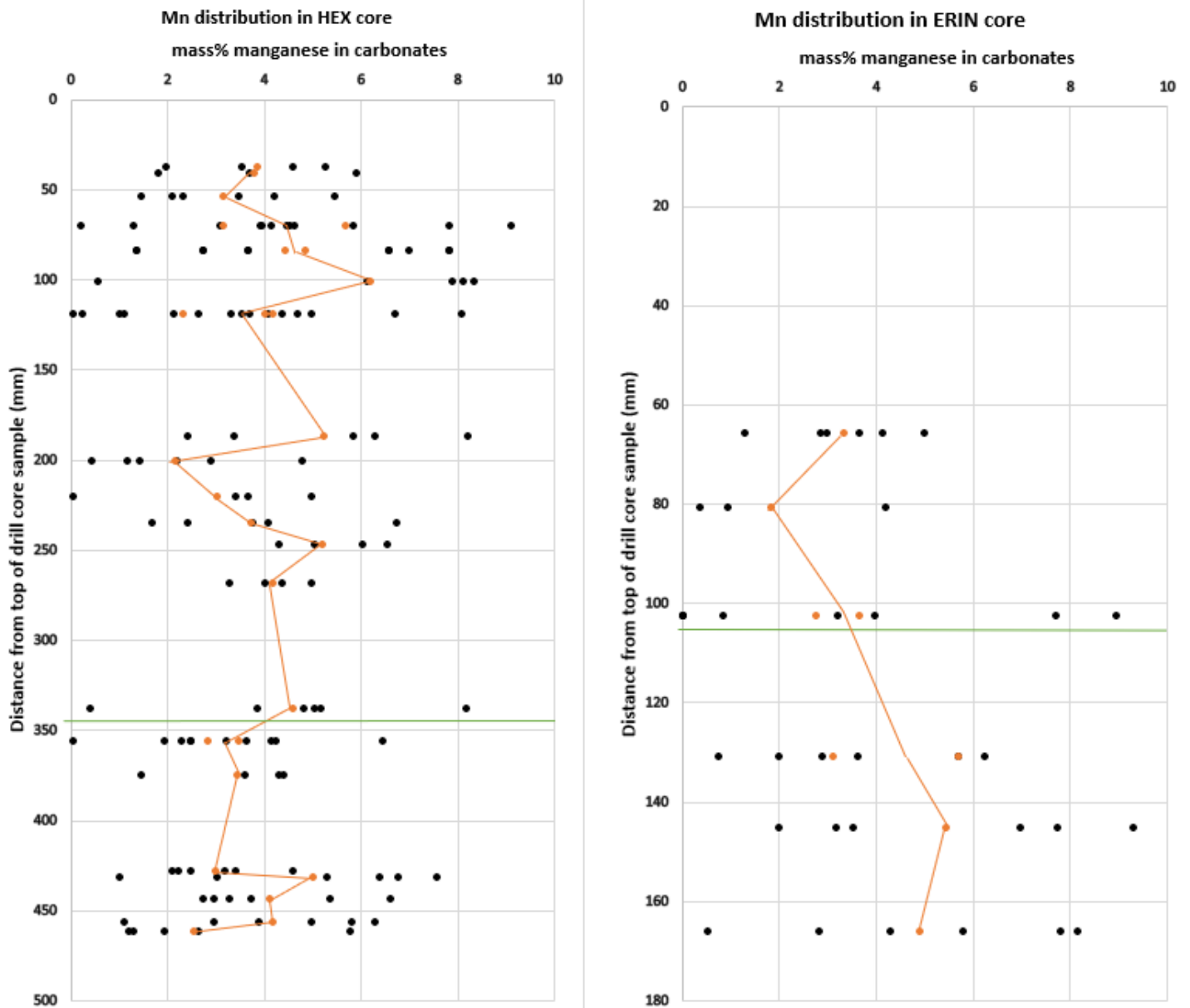
Figure 13 - Manganese content of carbonates in the HEX and ERIN drill cores. Average values are given in orange. The green line represents the proposed Griquatown-Makganyene contact. Cation wt% data is normalized to 100%

Figure 14 - Image of the suspected "High-magnesium calcites". Note the darker centre of the HMC with the lighter grey rim of ankerite.
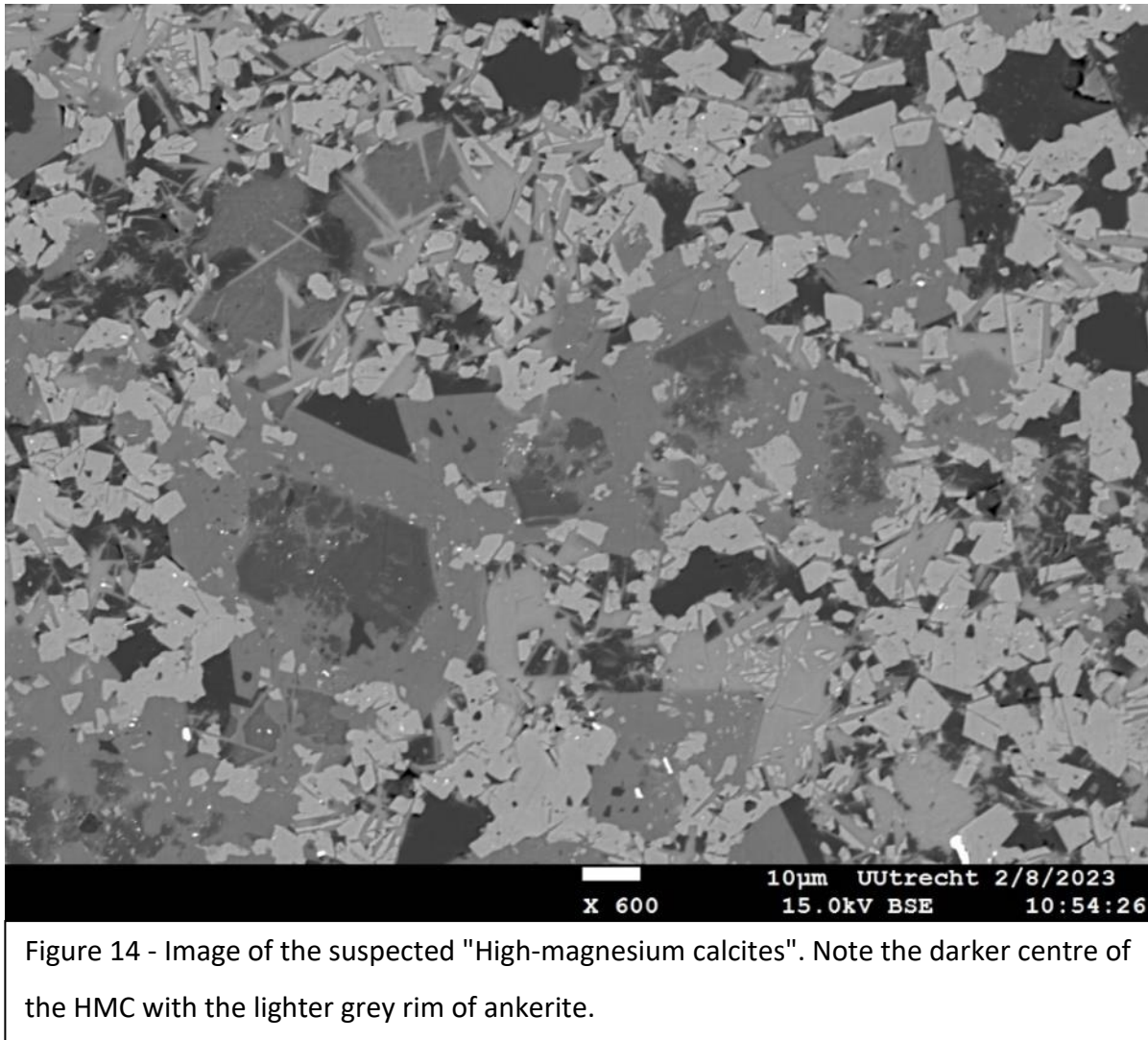
3.4 Clasts

3.4.1 Textures

All four drill cores have an upper part containing clasts and a lower part with few or absent clasts. The transition from a clast-poor to a clast-rich matrix is rather sharp in the AARPAN core, but more gradual in the ERIN, LONDON, and HEX cores. At the contact there is a minimal change in the mineralogy of the matrix. However, at the transition from clast-poor to clast-rich in the AARPAN core, the mineralogy also changes to a mainly chert and carbonate rich matrix, with minor amounts of stilpnomelane and opaques.

Some clasts show deformed layers around them. These deformed layers are mainly observed at and around the contact where clasts are not as densely packed. The magnitude of deformation differs per situation. The most obvious deformation of the layers is found in

the AARPAN core where a tail of the grey carbonate rich layer in the middle of the thin section bends down into the underlying stilpnomelane rich layer (Figure 15A). At the end of the tail an oval clast of stilpnomelane of approximately 1-2 mm can be seen. The clast is difficult to see in the overview image, so a photomicrograph of the clast is given in Figure 15B.

The HEX core contains a few fine examples of layers bending around a clast. Thin section 21 contains the clast found in Figure 15C, which has distorted matrix around the clast. Layers bend around the clast and pinch out towards the clast. Figure 15D shows a clast in thin section 22 which also distorts the matrix around it. Layers bend around the clast, most easily visible in the layers deposited over the clast.
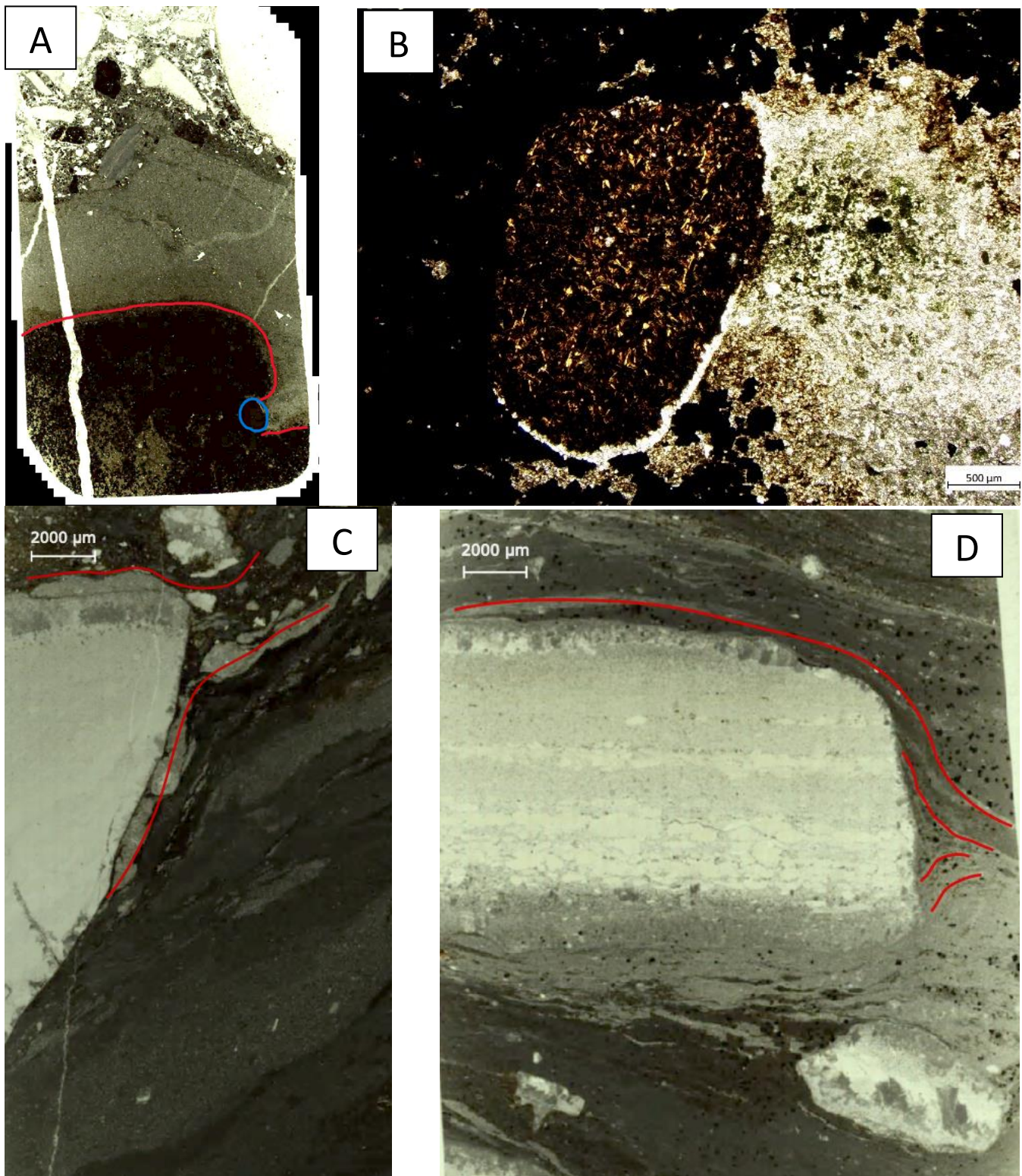
Figure 15 - Clasts found in the drill cores with distorted matrix around them. The red lines indicate the layering of the matrix. A) whole scan of TS3 of the AARPAN core. The contact between two layers forms a tail and is indicated with a red line. Encircled in blue is a stilpnomelane clast at the end of the tail. B) The stilpnomelane clast at the end of the tail. C) and D) Soft sediment deformation structures around clasts in the HEX core.

3.4.2 Clast mineralogy

AARPAN

The most common clast found in thin sections 1 and 2 in the AARPAN core contains predominantly chert with small 10 - 20 μm carbonate crystals homogeneously dispersed throughout (Figure 16). Stilpnomelane is also present in these clasts, often clumped together and less homogeneously dispersed than the carbonates. These clasts are also found in thin section 3. However, thin section 3, which is closer to the contact, contains more carbonate clasts, microcrystalline carbonate clasts, stilpnomelane rich clasts, and few opaque clasts. In addition to a few chert clasts.
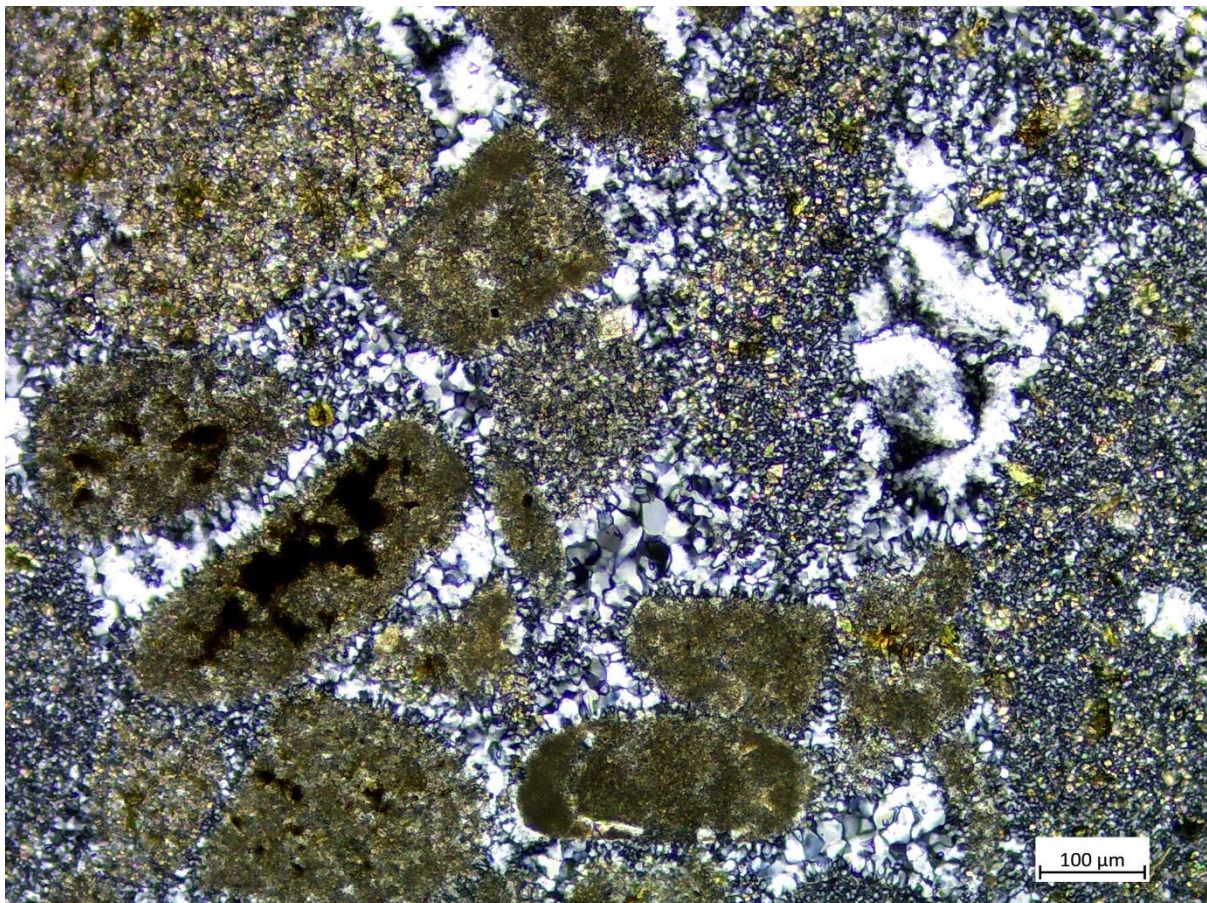
Figure 16 - The general mineralogy of the clasts in the AARPAN core. The fine grained grey material is chert, the yellow material are the carbonates, and the brown material is mainly stilpnomelane. The matrix consists of larger grained chert/quartz. Image from thin section 2.

ERIN

Clasts found in the ERIN core are mostly fine grained carbonates (Figure 17). Small amounts of chert, mixed chert and carbonate clasts, and few quartz clasts are present. At the top of thin section 8 a large clast was found. The large clast mainly consists of chert, is rimmed with carbonates, and contains smaller areas with opaques and carbonates. One clear example of stilpnomelane ingrowths can be seen in thin section 7 from the ERIN drill core (See Figure 18).

LONDON

Thin section 12 of the LONDON core contains a variety of clast. In addition to chert and carbonate clasts, like the ones seen in ERIN core, the LONDON core also contains mixed stilpnomelane and carbonate clasts. These clasts vary in composition from mainly stilpnomelane with few euhedral carbonate crystals homogeneously spread around the clast, to clasts rich in carbonates with the stilpnomelane homogeneously spread around the clast. Stilpnomelane-rich clasts often contain opaque minerals too. Some Opaque rich clasts are present. Chert rich clasts dominate thin section 13 (Figure 19). Additional minerals in the chert rich clasts can be carbonates, stilpnomelane and opaques. A large clast occurs at the top of the thin section containing almost equal portions of carbonate, stilpnomelane, chert and lesser amounts of opaques. Thin section 14 only contains a few clasts, which are chert-rich and contain few carbonate grains. A stilpnomelane and carbonate clast in thin section 12 looks similar to material found in thin sections 15 and 16 in the Griquatown Formation of the same drill core.
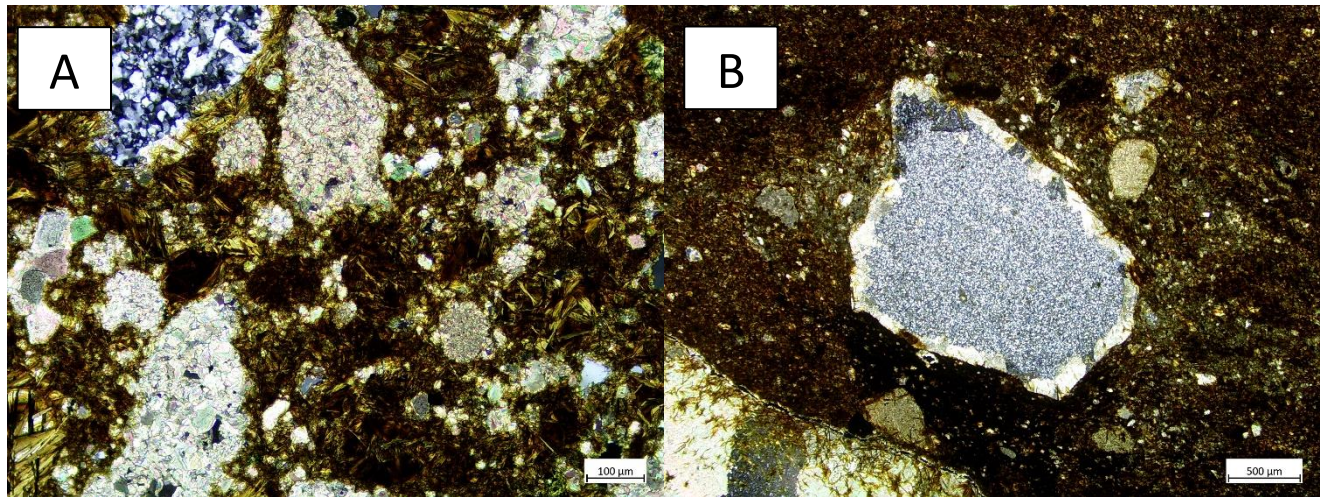
Figure 17 - Commonly found clasts in the ERIN core (A). Chert clast rimmed with a carbonate rim (B). The matrix is dominated by stilpnomelane, hence the brown colour. Images from thin sections 6 (A) and 8 (B).
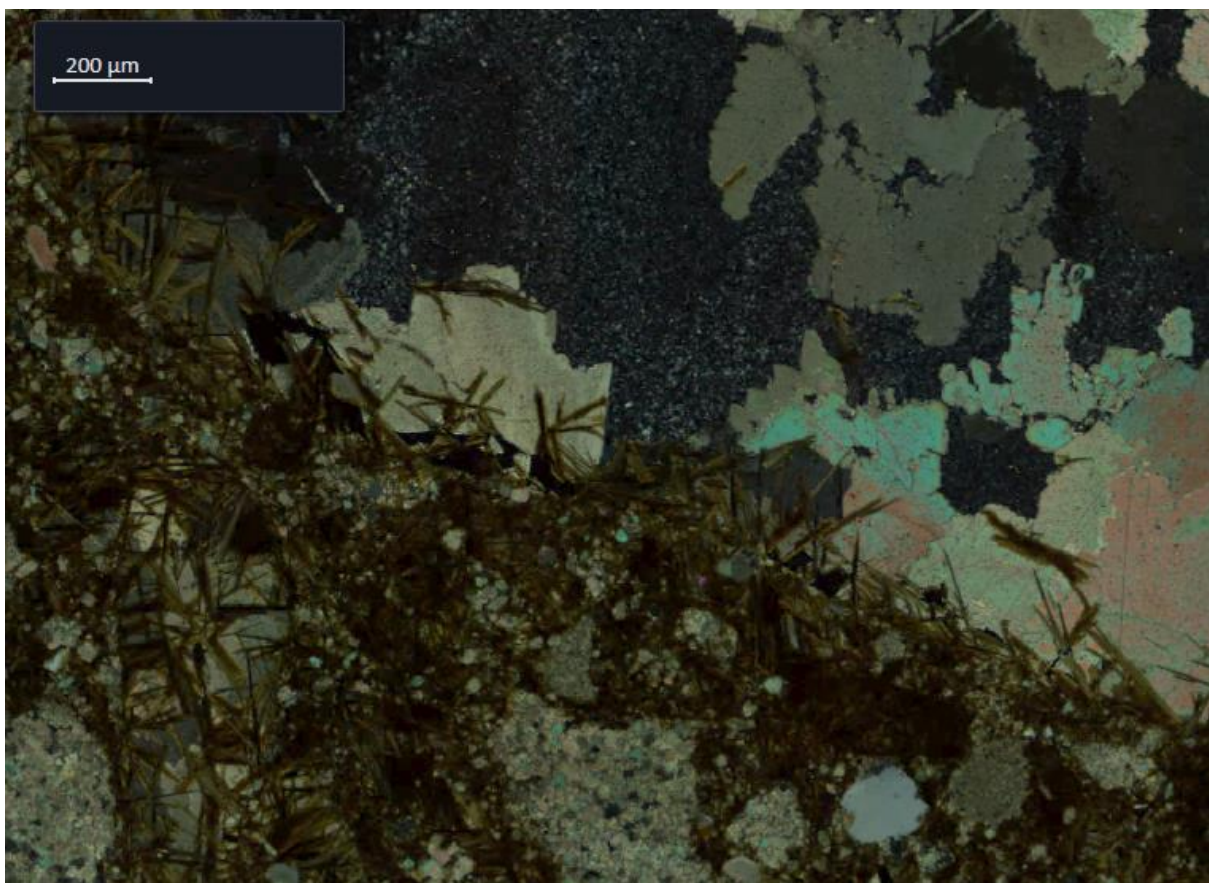
Figure 18 - This photomicrograph shows a part of thin section 7 of the ERIN core. Part of a clast is seen in the top half, the bottom half shows a stilpnomelane rich matrix with carbonate clasts. This shows a clear example of the ingrowth of the brown stilpnomelane into the chert and carbonate rich clast.
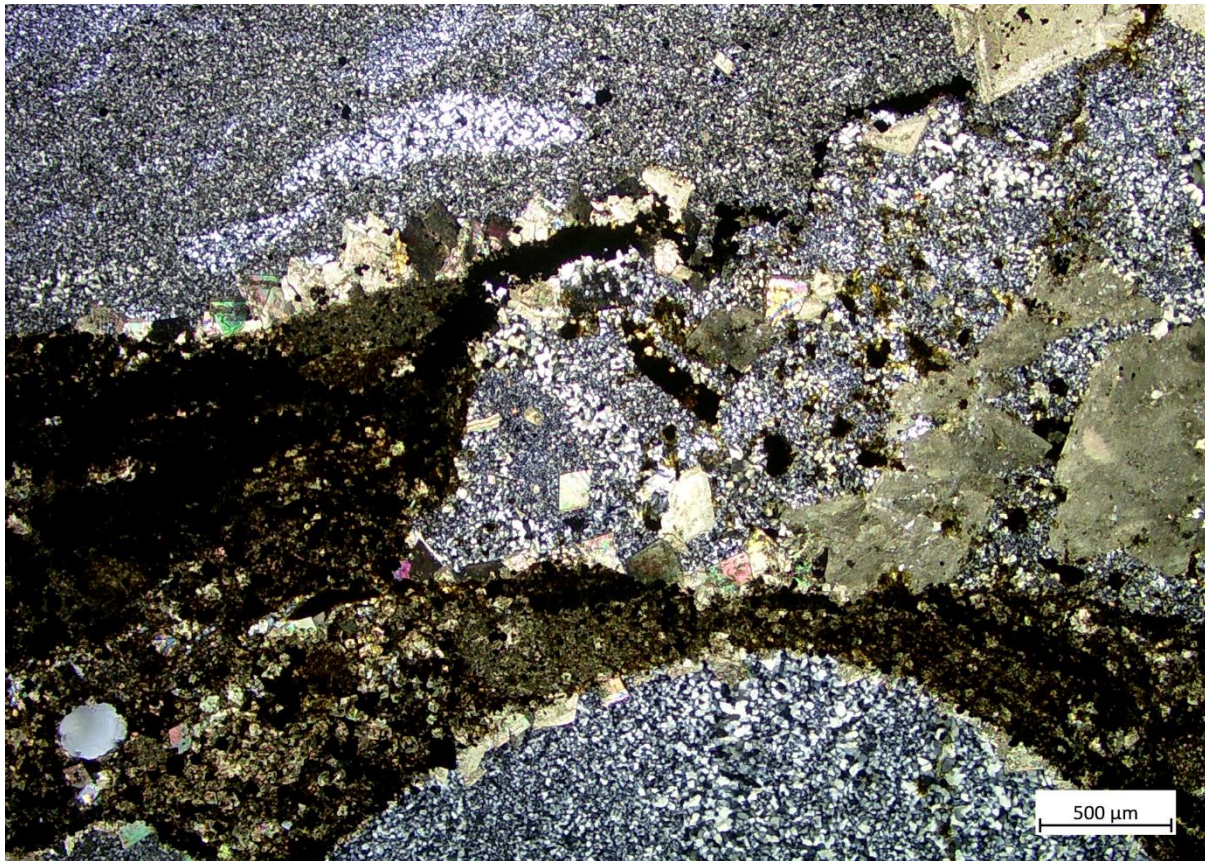
Figure 19 - The common mineralogy of the clasts in the LONDON core. Chert clasts containing carbonates and varying degrees of stilpnomelane in a stilpnomelane rich matrix. Image from thin section 13.

HEX

The HEX core contains chert, carbonates, and chert carbonate clasts in thin section 18. Multiple chert clasts are found which are rimmed, or partly rimmed with carbonate minerals. In thin section 19 the clasts roughly have the same mineralogy as in thin section 18, with the addition of more stilpnomelane rich clasts. Thin section 20 contains quite a lot of quartz grains, the clasts consist of mostly carbonate rimmed chert and stilpnomelane rimmed carbonates, and a few stilpnomelane clasts (Figure 20). Thin section 21 mainly contains chert clasts with carbonate rims similar to what is described before. In the clast poor bottom part of the thin section there is one larger clast also of chert rimmed with carbonates. These clasts are also found in the clast poor thin sections 22 and 23. Thin section 24 then contains some carbonate rich clasts at the top of the thin section before clasts disappear.

Figure 20 - Commonly found clasts in the HEX core. More common in this drill core compared to AARPAN, ERIN or LONDON are the single grain quartz crystals like the few on the left of the image. Also note the angular chert and rounded carbonate clast in the middle and right respectively. Image form thin section 20.

3.5 Laser ablation ICP-MS
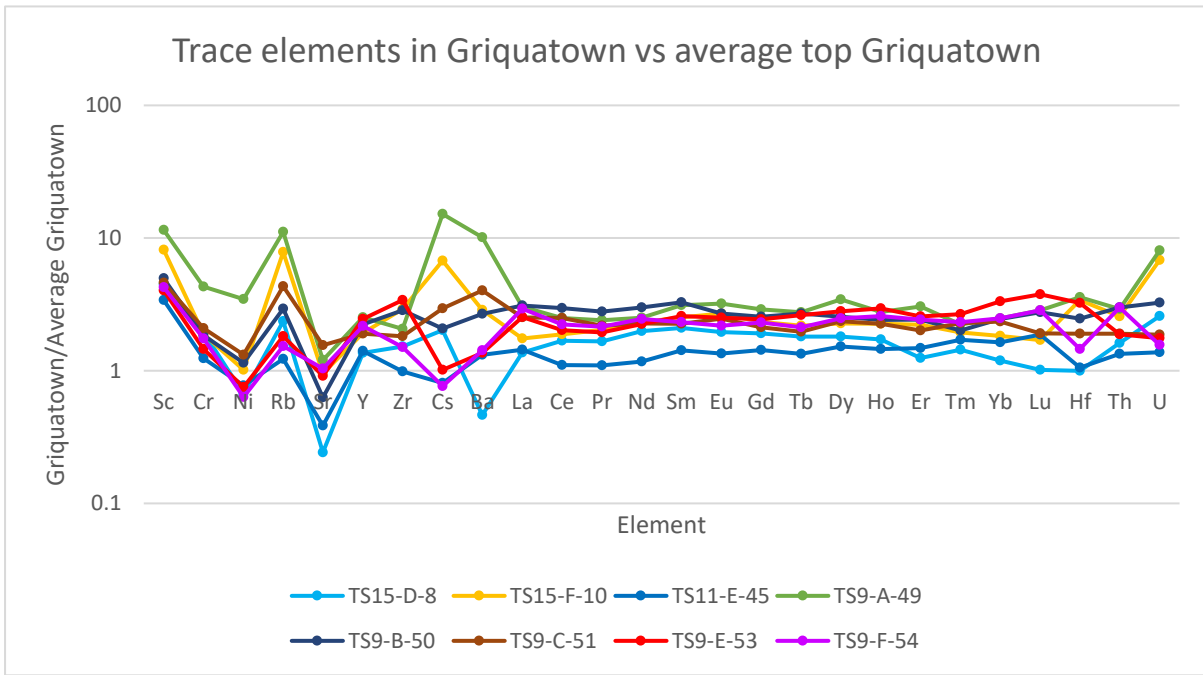
Figure 21 - Griquatown Formation trace element data normalized to top of Griquatown data from Oonk (2017).
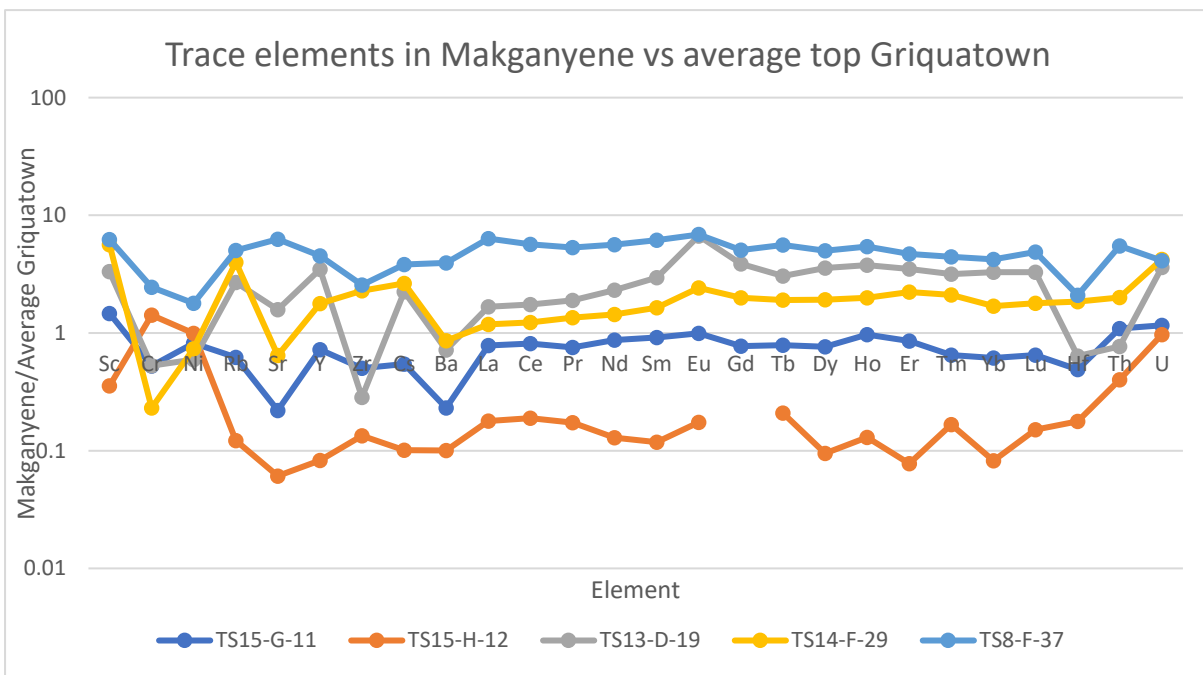
Figure 22 - Makganyene Formation trace element data normalized to top of Griquatown data from Oonk (2017).
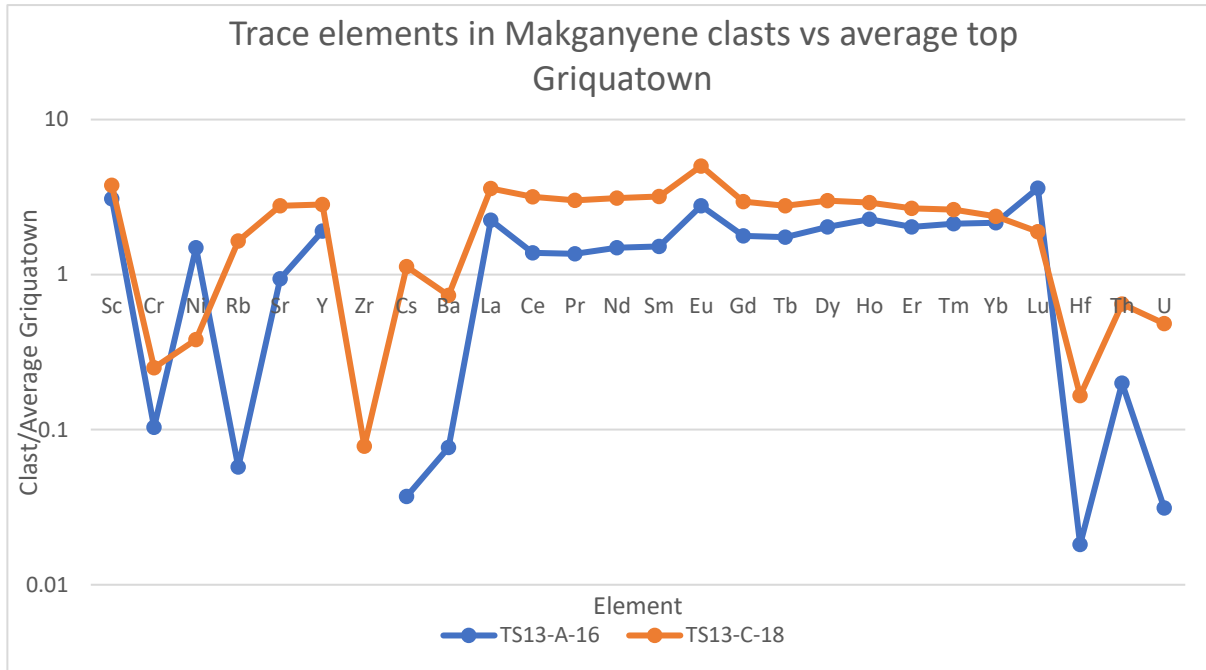
Figure 23 - Trace element data from clasts in the Makganyene Formation, normalized to top of Griquatown data from Oonk (2017).

Element plots were made for the Griquatown Formation (Figure 21). These plots are normalized to average Griquatown values from Oonk (2017). In the Griquatown Formation the chemical variability is mostly seen in elements other than REE. Enrichments in Sc are present in most measurements. Uranium enrichments are seen in measurements TS15-D, TS15-F and TS9-A.

The Makganyene Formation also shows some enrichment in Sc and U in some measurements (Figure 22). TS13-D and TS14-F show an enrichment in Eu. The Makganyene Formation is also not enriched in elements like Zr and Hf compared to the Griquatown.

Clasts in the Makganyene show clear depletions of Hf, and Zr in measurement TS13-C compared to the average Griquatown, as well as a slight Eu enrichment (Figure 23).
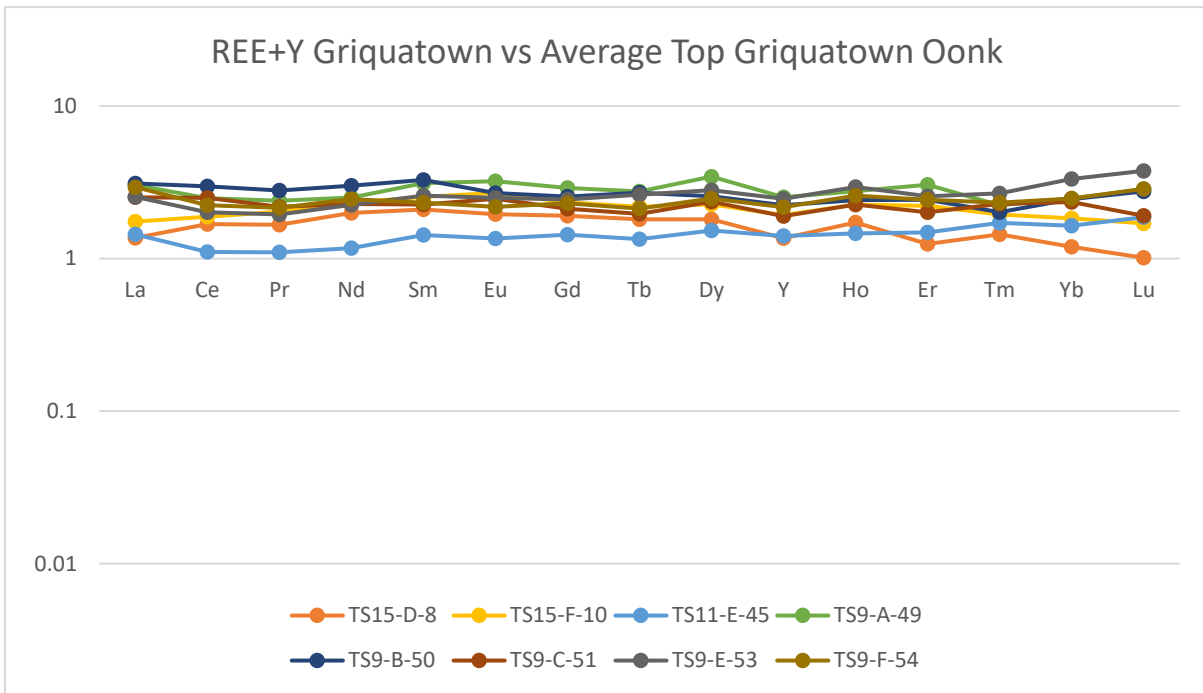
Figure 24 - REE+Y plot of Griquatown Formation matrix normalized to the average of the Griquatown Formation from Oonk (2017).
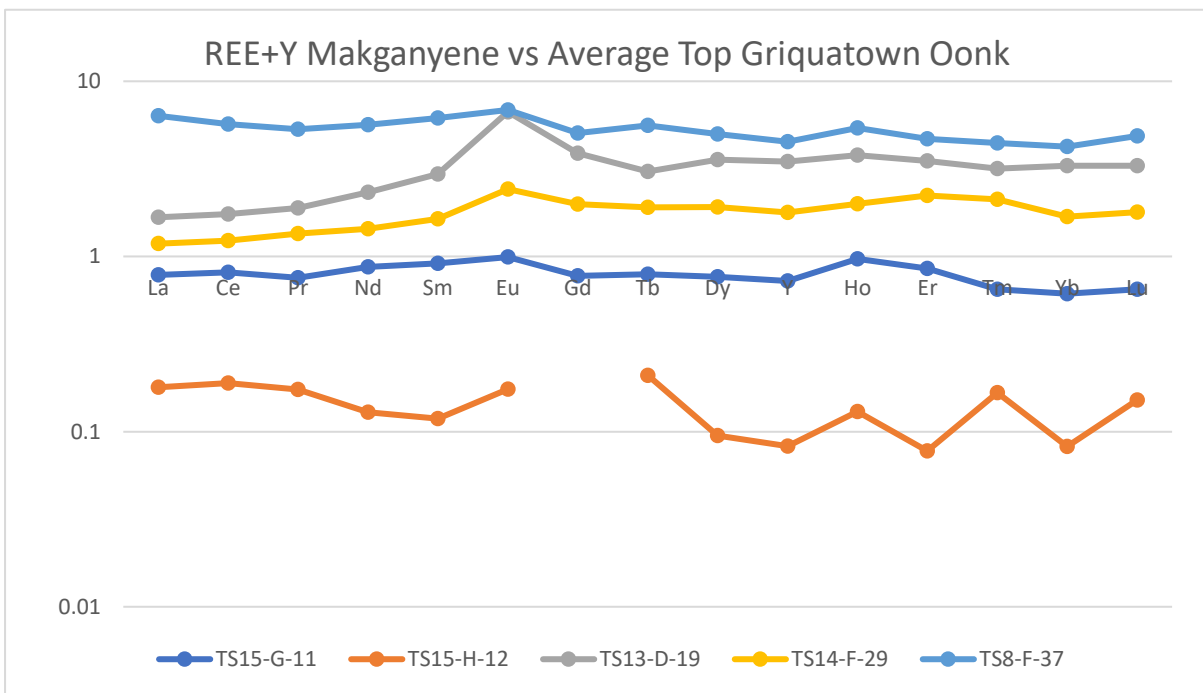
Figure 25 - REE+Y plot of Makganyene Formation matrix normalized to the average of the Griquatown Formation from Oonk (2017).
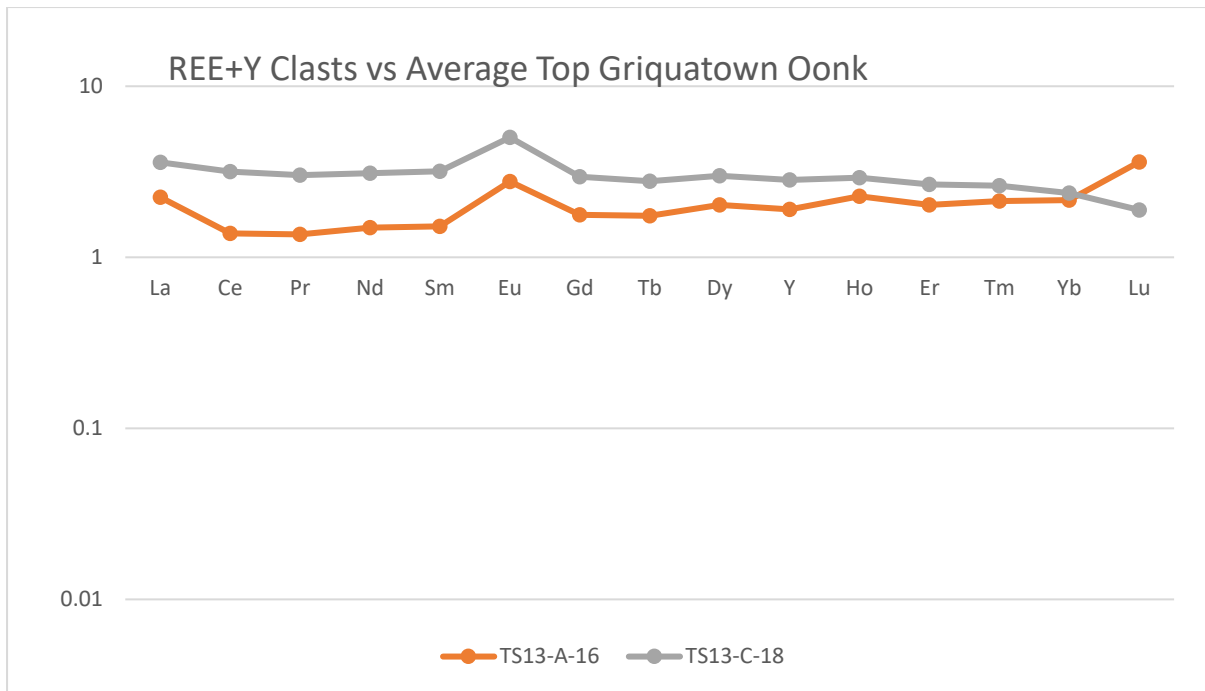
Figure 26 - REE+Y plot of clasts in the Makganyene Formation normalized to the average of the Griquatown Formation from Oonk (2017).

Separate Rare Earth element (REE+Y) have been made. These plots are also normalized to averages from the top of the Griquatown as found by Oonk (2017). The data shows relatively flat signatures (Figure 24). Also, the Makganyene Formation shows relatively flat signatures in the REE+Y patterns as can be seen in Figure 25. A slight Eu anomaly can be seen In the Makganyene Formation relative to the top Griquatown average. REE element signatures in the Makganyene clasts are flat and look similar to those of the Griquatown and Makganyene Formations (see Figure 26). Eu anomalies are present in the Makganyene clasts.
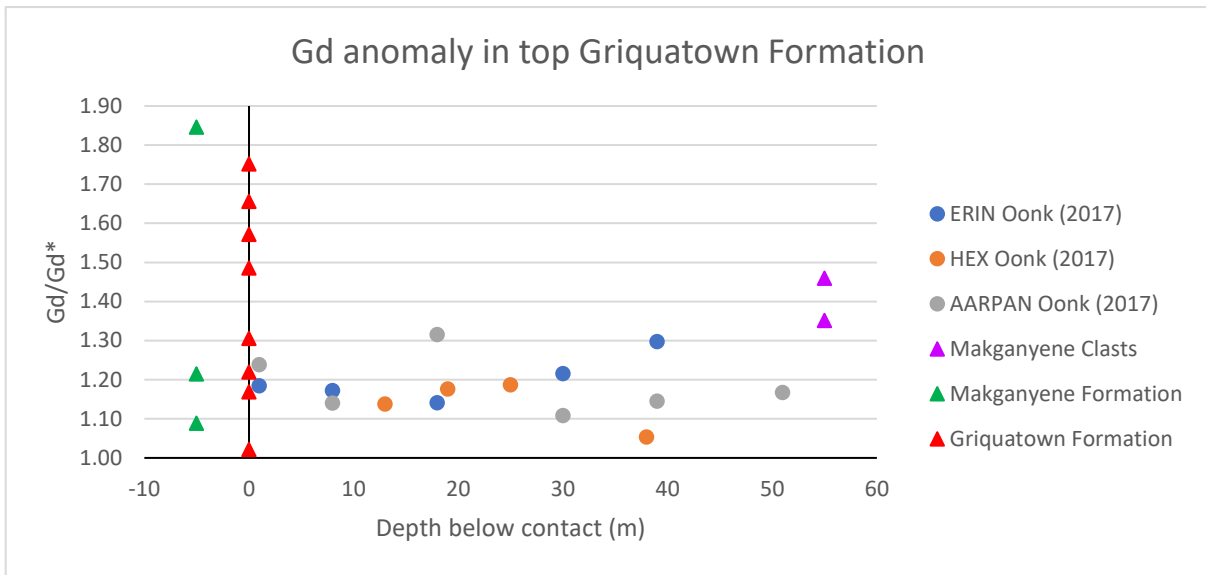
Figure 27 - Gd anomaly values plotted against the stratigraphic depth below the
Makganyene/Griquatown contact as interpreted by Oonk (2017).
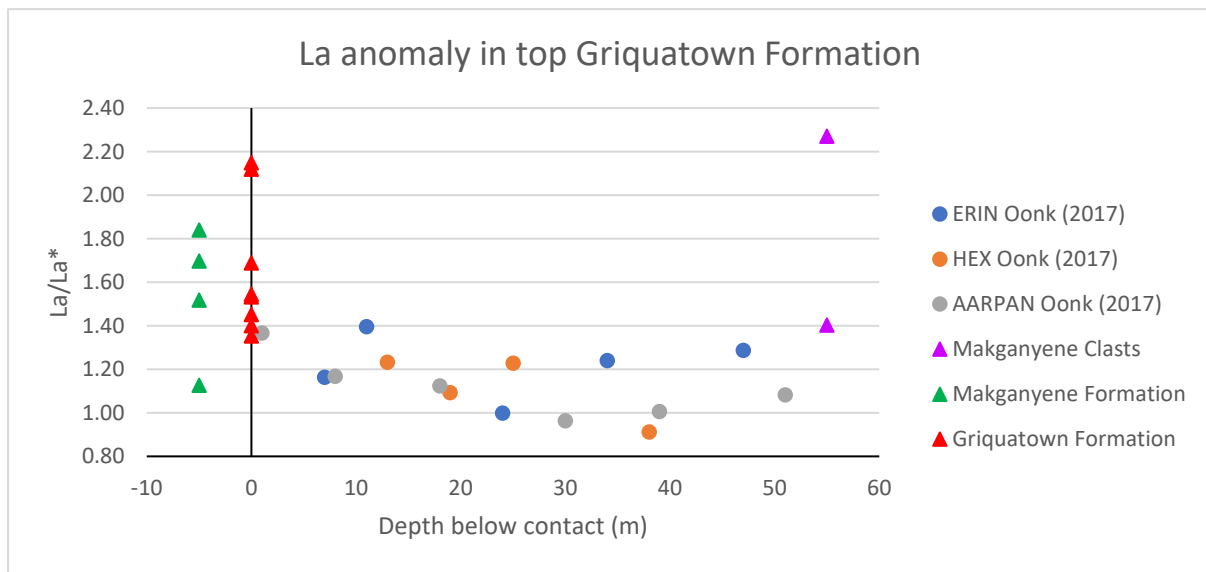
Figure 28 - La anomaly values plotted against stratigraphic depth below the
Makganyene/Griquatown contact as interpreted by Oonk (2017).
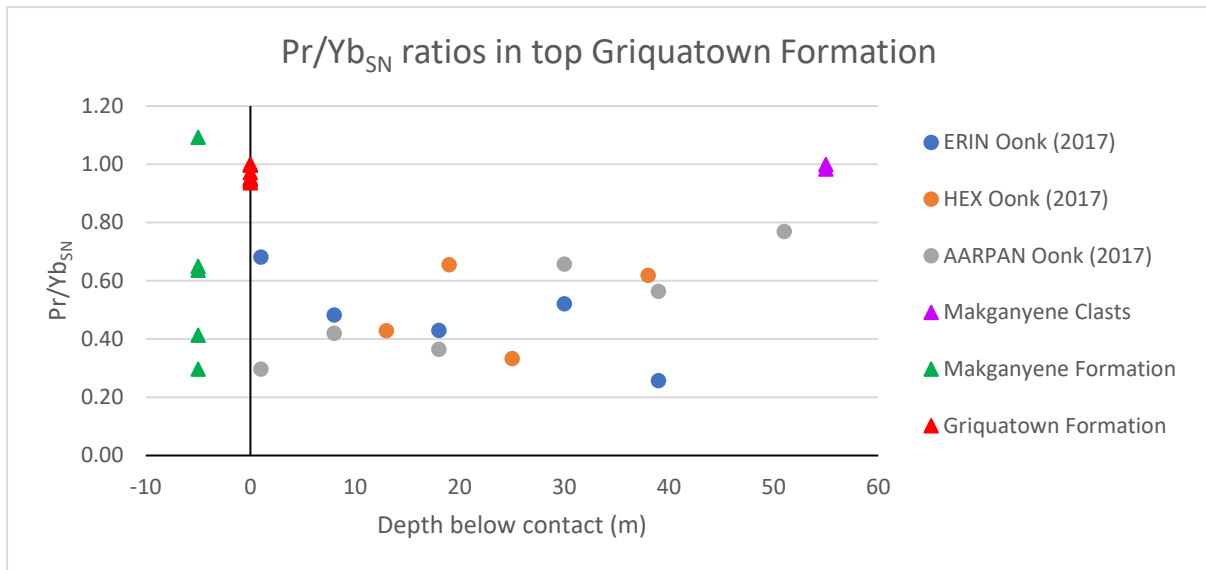
Figure 29 - Pr/Yb$_{SN}$ ratios of the Makganyene Formation and clasts in it, and Griquatown Formation compared to ratios from Oonk (2017).
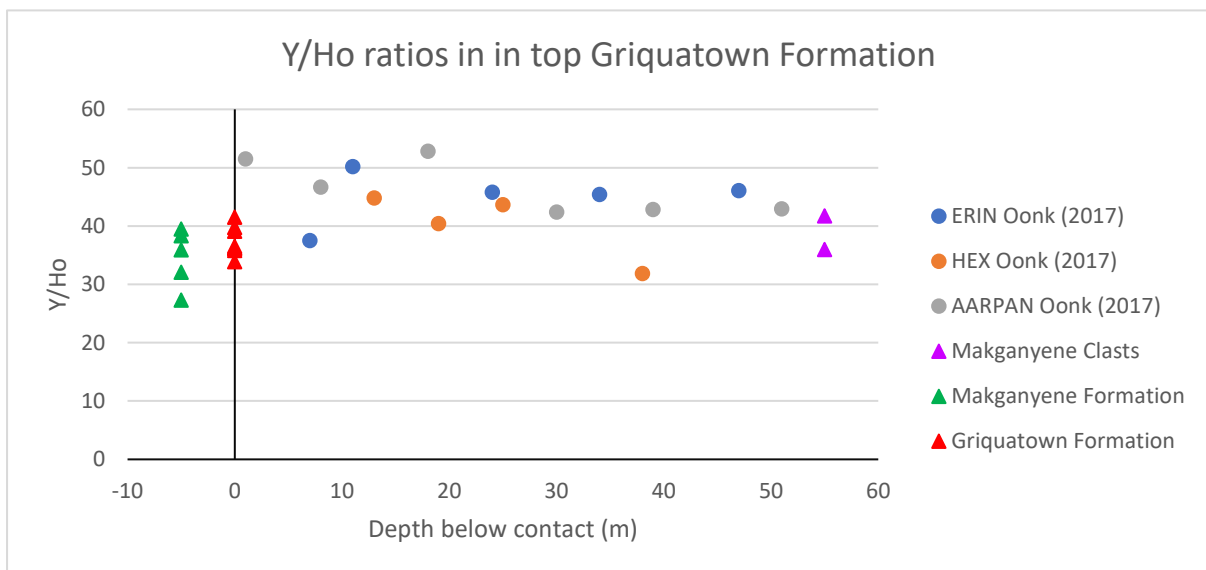
Figure 30 - Y/Ho ratios of this project, as well as Y/Ho values from Oonk (2017).

Anomaly data was plotted against depth for Oonk (2017) data. Data from this project got arbitrary depths assigned, partly based on stratigraphic position. Clasts from the Makganyene Formation got the arbitrary depth of 55 m.

Gadolinium anomalies are greater than 1 as can be seen in Figure 27. Gd/Gd* values for the Makganyene Formation can exceed 1.8. The Griquatown Formation has a maximum value between 1.7 and 1.8, and the clasts in the Makganyene Formation do not surpass 1.5. Meaning not all Gd/Gd* values from this project fall in the range of 1.0-1.3 found by Oonk (2017).

A similar signal can be seen in the La/La* values (Figure 28). La/La* from this project are all greater than 1. The maximum value in the Makganyene Formation is 1.8. The maximum La/La* value for the Griquatown is higher at 2.1. One La/La* value from a clast in the Makganyene Formation is even higher at 2.3. Again, these values do not completely fall in the range of La/La* data from Oonk (2017).

Pr/Yb$_{SN}$ values exceed 0.2 and go up to around 1.1 in the Makganyene Formation and up to 1.0 in the Griquatown Formation and the clasts in the Makganyene Formation. These values exceed the ones found in Oonk (2017) as can be seen in Figure 29. This means that the Griquatown and Makganyene are depleted in Light-REE (LREE) compared to Heavy-REE (HREE).

Y/Ho ratios can be seen in Figure 30. The values for The Makganyene start at 27 and go up to 39. For the Griquatown the Y/Ho ratios start at 34 and go up to 42. Y/Ho ratios in the Makganyene clasts are 36 and 42. Y/Ho ratios from this project fit well within the range of 32 to 53 as found by Oonk (2017).

4. Discussion

First observations of the drill cores already gave clues for a gradual Griquatown and Makganyene contact. The CT scan of the AARPAN core especially showed an uneven surface of the contact. The ERIN and HEX cores also show a uniform radiodensity that is linked to the abundance of stilpnomelane at both sides of the contact.

It appears that the matrix of the Makganyene Formation in the ERIN, LONDON and HEX cores contain considerable amounts of main BIF minerals. The same minerals that are present in the Makganyene Formation were already observed in the underlying Griquatown Formation. This might indicate that the depositional environment and conditions during deposition of the Makganyene Formation were similar to when the top of the Griquatown Formation was deposited. This is further supported by the rather consistent Mn contents observed in ankerite and siderite throughout the drill cores. Considering the ages of deposition for the two formations could further support the idea of synchronous deposition. A maximum age of 2432 ± 31 Ma (Nelson et al., 1999) for the Griquatown Formation, and an age of 2423 ± 1 Ma (Senger et al., 2023) for the Makganyene Formation shows that there is a possible overlap in the deposition of the two formations.

The AARPAN and HEX cores show layers that are bending around and towards clasts. These disturbances in the layering have been interpreted as dropstone textures caused by the deposition of dropstones. These dropstones were transported by glaciers during a glaciation. At a certain moment, these glaciers broke off and ended up floating in marine waters. The transported stones were gravitationally deposited when the ice melted, deforming the sediment as they land (Thomas & Summers, 1981). The presence of dropstones in the drill cores, as well as grounding zone wedges found in the HEX core (Le Heron et al., 2022), are typical characteristics for a glacial rainout deposit (Arnaud & Etienne, 2011). This is in favor of a gradational contact between the Griquatown and Makganyene contact as a rainout deposit typically has a conformable basal contact.

Additionally, positive anomalies for La and Gd have been found in the Makganyene Formations matrix, as well as a LREE depletion relative to HREE. These signals have been linked to a marine origin (Bolhar et al., 2004). Bolhar et al. (2004) also mentions Y/Ho ratios of ~26 being characteristic for terrestrial rocks, but generally being higher in marine rocks,

like ancient BIF. Comparing the data from the Griquatown and Makganyene Formations from this project shows similar REE signatures and anomalies. Therefore, it seems that the Makganyene Formation is formed with either reworked material derived from the Griquatown Formation, a continued deposition of Griquatown-like IF occurred, or a mix of both. Le Heron (2022) already coined the possibility that the Makganyene Formation was formed during a simultaneous precipitation of iron-rich material and the results from this research project support that idea.

Previous research based the model of an unconformable contact between the Griquatown Formation and Makganyene Formation on the absence of the Koegas Subgroup North of the Griquatown fault zone. It is argued that the Koegas Subgroup was removed prior to the deposition of the Makganyene Formation (Beukes, 1983). More recent research has linked part of the Koegas Subgroup to the Griquatown Formation in terms of being deposited synchronously (Siahi et al., 2020). This is supported by the bulk Mn content reported in the Koegas Subgroup ranging from 1% to 16.6% (Johnson et al., 2013). Compared to the bulk rock Mn content in the Griquatown Formation of 1% to 5%. The Koegas Subgroup may therefore be quite similar to the Griquatown Formation in a chemical sense (Siahi et al., 2020). If this is the case, the Koegas Subgroup was not deposited on top of the Griquatown Formation. But rather as a lateral equivalent of the Griquatown Formation. The regional absence of the Koegas Subgroup between the Griquatown and Makganyene Formations therefore does not mean there is an erosional contact at the base of the Makganyene Formation. Based on the mineralogical, textural, chemical and chronological data, it becomes plausible that the contact between the Griquatown and Makganyene Formations is a gradual transition in some way. Figure 30 shows the new proposed stratigraphic column, without an unconformable contact, but rather portrays the Koegas Subgroup as being deposited synchronously to the Griquatown Formation.

The Makganyene Formation shows no enrichment in Zr and Hf compared to the top 50 meters of the Griquatown Formation. As these elements are generally linked to the input of felsic material to the basin (Rao & Naqvi, 1995). This combined with comparable REE signatures clasts as the Makganyene and Griquatown, implies that most material supplied to the Makganyene Formation during deposition is of a similar composition. These clasts, based on the REE signatures, are likely coming from the Griquatown Formation, this is in line with Polteau et al. (2006), who argued that clasts in the Makganyene were coming from the Asbestos Hills Subgroup. The Makganyene Formation could be caused by reworking of material from the Griquatown Formation. Meaning that glacial activity in the area during the Makganyene Glaciation, brought in little to no vastly different material, or sampled Griquatown BIF from the area. A few LA-ICP-MS clast measurements gave vastly different signatures but were also incomplete. Because of that, those measurements were left out of the figures. Clasts do vary quite a bit in the mineral contents, and the chert was difficult to analyse. Therefore, it is not ruled out that the Makganyene contains clasts of other
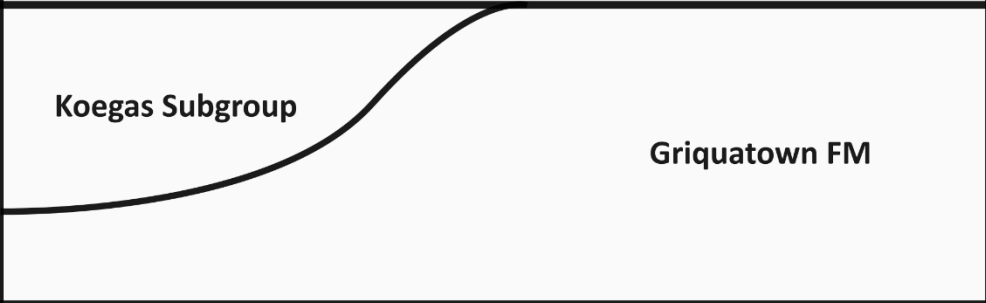
Stratigraphic column	Age (Ma)
Makganyene FM	**2423 ± 1**[a]
Koegas Subgroup **Griquatown FM**	**2415 ± 6**[b] **(Koegas)** **2432 ± 31**[c], **2480 ± 18**[b] **(Griquatown)**
Kuruman FM	**2460 ± 5**[d]

Figure 30 - Stratigraphic column of the proposed stratigraphy. This shows the synchronous deposition of the Griquatown Formation and the Koegas Subgroup. Ages of

Formations as well. But based on the mineralogy, other sources for clasts would likely be other IF. It would be expected to find vastly different clasts in the Makganyene Formation because glaciers can transport clasts over hundreds of kilometres. However, smaller scale transport over hundreds of meters is also possible in case of cirque glaciers (Kirkbride, 2002). Smaller scale transport would explain a less diverse assemblage of clasts in the diamictite. Finding only Griquatown-like rock in the Makganyene could mean that there was predominantly local sampling. However, in case of glacial sampling of other IF, this could mean that BIF were found over hundreds of kilometres at the time. More sampling would have to be done to identify these possible other sources of material as only a small sample size gave reliable data.

Clasts in the Makganyene Formation seem to have two different origins based on the textures. The first category of clasts has a regional origin. These clasts show sharp contacts between the clast and matrix, and in some cases show soft sediment deformation textures in the matrix around the clast.

The second category of clasts likely have a local origin. These clasts have ingrowths of stilpnomelane along the margins that could be related to internal reworking of sediments. These clasts were likely reworked before consolidating. The semi-consolidated nature of the clasts allowed the stilpnomelane to grow into these clasts. The idea of internal reworking fits well in the model described by Le Heron (2022). Le Heron (2022) links an episodic development of a marine terminating grounding zone wedge to the formation of the Makganyene Formation. In this scenario it is not unlikely that material on the seafloor was pushed around by the ice sheet, causing disturbances, and mixing of material. Therefore, an accumulation of immiscible material, followed by mineral growth and consolidation seems plausible for the formation of clasts showing ingrowths of stilpnomelane. Chemically these should have a similar compositions to the Griquatown or Makganyene matrix. For this, a more clasts-targeted research with more data points would be needed to verify this.

Putting the information together suggests that the formation of the Makganyene Formation happened as follows. The Makganyene Formation was likely formed following the Griquatown Formation with little to no change in the depositional environment as indicated by the mineralogical, textural, and chemical data, but rather reflects a change in surface temperatures linked to the glaciation. This glaciation, that is correspondingly named the

Makganyene Glaciation, saw the development of a grounding zone wedge that reworked sediments from the Griquatown Formation, while simultaneous deposition of new material with similar characteristics as the underlying Griquatown Formation, formed the Makganyene Formation. Clasts present in the Makganyene Formation belong to one of two categories. Clasts are either dropped in as a result of glacial activity, or form as a result of internal reworking of semi-consolidated sediments. The clasts present in the Makganyene could be partly derived from the Griquatown Formation as indicated by a similar REE signature. These semi-consolidated sediments allow for stilpnomelane to grow into the clast, prior to consolidating.

5. Conclusion

This project was carried out with the intention of determining the nature of the contact of the Griquatown Formation and the overlying Makganyene Formation and indicating the changes happening around the contact.

Mineralogical, textural, and chemical data suggests the matrix of the Makganyene Formation is made of internally reworked material from the Griquatown Formation, with synchronously deposited material with Griquatown-like signatures. This is further supported by the chemical composition of clasts present in the Makganyene Formation. Little to no change occurred in the depositional environment in the transition from the Griquatown to Makganyene Formation. Reworking was most likely caused by episodic disturbances by glacial progression and retreat.

The findings of this research project are contradicting earlier works (e.g., Visser, 1971; Beukes 1983), but are in line with more recent publications (e.g., Polteau et al., 2006; Siahi et al., 2020; Le Heron et al., 2022). Therefore, this project has the potential to provide an important piece of information in the onset of the Makganyene Glaciation and paves the way for more focussed research on the provenance of the clasts in the Makganyene Formation.

6. References

Anbar, A. D., Duan, Y., Lyons, T. W., Arnold, G. L., Kendall, B., Creaser, R. A., Kaufman, A. J., Gordon, G. W., Scott, C., Garvin, J. & Buick, R. (2007). A whiff of oxygen before the great oxidation event?. *Science*, *317*(5846), 1903-1906. https://doi.org/10.1126/science.1140325

Arnaud, E., & Etienne, J. L. (2011). Chapter 3 Recognition of glacial influence in Neoproterozoic sedimentary successions. *Geological Society, London, Memoirs*, 36(1), 39-50. doi:10.1144/m36.3

Ayres, D. E. (1972). Genesis of iron-bearing minerals in banded iron formation mesobands in the Dales Gorge Member, Hamersley Group, Western Australia. *Economic Geology*, *67*(8), 1214-1233. https://doi.org/10.2113/gsecongeo.67.8.1214

Bauer, K. W., Byrne, J. M., Kenward, P., Simister, R. L., Michiels, C. C., Friese, A., ... & Crowe, S. A. (2020). Magnetite biomineralization in ferruginous waters and early Earth evolution. *Earth and Planetary Science Letters*, 549, 116495. https://doi.org/10.1016/j.epsl.2020.116495

Bertine, K. K., & Turekian, K. K. (1973). Molybdenum in marine deposits. *Geochimica et Cosmochimica Acta*, *37*(6), 1415-1434. https://doi.org/10.1016/0016-7037(73)90080-X

Beukes, N. J. (1980). Lithofacies and stratigraphy of the Kuruman and Griquatown iron-formations, northern Cape Province, South Africa. *South African Journal of Geology*, 83(1), 69-86. https://doi.org/10.1016/0301-9268(84)90069-X

Beukes, N. J. (1983). Palaeoenvironmental setting of iron-formations in the depositional basin of the Transvaal Supergroup, South Africa. *Developments in Precambrian Geology* (Vol. 6, pp. 131-198). Elsevier. https://doi.org/10.1016/S0166-2635(08)70043-4

Beukes, N. J. (1984). Sedimentology of the Kuruman and Griquatown iron-formations, transvaal supergroup, Griqualand West, South Africa. *Precambrian Research, 24*(1), 47-84. https://doi.org/10.1016/0301-9268(84)90069-X

Beukes, N. J., & Gutzmer, J. (2008). Origin and paleoenvironmental significance of major iron formations at the Archean-Paleoproterozoic boundary. https://doi.org/10.5382/Rev.15.01

Bolhar, R., Kamber, B. S., Moorbath, S., Fedo, C. M., & Whitehouse, M. J. (2004). Characterisation of early Archaean chemical sediments by trace element signatures. *Earth and Planetary Science Letters*, 222(1), 43-60. https://doi.org/10.1016/j.epsl.2004.02.016

Bolhar, R., Kamber, B. S., Moorbath, S., Whitehouse, M. J., & Collerson, K. D. (2005). Chemical characterization of earth's most ancient clastic metasediments from the Isua Greenstone Belt, southern West Greenland. *Geochimica et Cosmochimica Acta*, 69(6), 1555–1573. doi:10.1016/j.gca.2004.09.023

Cairns-Smith, A. G. (1978). Precambrian solution photochemistry, inverse segregation, and banded iron formations. *Nature*, *276*(5690), 807-808. http://doi.org/10.1038/276807a0

Calvert, S. E., & Pedersen, T. F. (1996). Sedimentary geochemistry of manganese; implications for the environment of formation of manganiferous black shales. *Economic Geology*, *91*(1), 36-47. https://doi.org/10.2113/gsecongeo.91.1.36

Cloud, P. (1973). Paleoecological significance of the banded iron-formation. *Economic Geology*, *68*(7), 1135-1143. https://doi.org/10.2113/gsecongeo.68.7.1135

Crowell, J. C. (1978). Gondwanan glaciation, cyclothems, continental positioning, and climate change. *American Journal of Science*, *278*(10), 1345-1372. https://doi.org/10.2475/ajs.278.10.1345

Danielson, A., Möller, P., & Dulski, P. (1992). The europium anomalies in banded iron formations and the thermal history of the oceanic crust. *Chemical geology*, *97*(1-2), 89-100. https://doi.org/10.1016/0009-2541(92)90137-T

Dessert, C., Dupré, B., Gaillardet, J., François, L. M., & Allègre, C. J. (2003). Basalt weathering laws and the impact of basalt weathering on the global carbon cycle. *Chemical Geology*, *202*(3-4), 257-273. https://doi.org/10.1016/j.chemgeo.2002.10.001

Dodd, M. S., Wang, H., Li, C., Towner, M., Thomson, A. R., Slack, J. F., Wan, Y., Pirajno, F., Manikyamba, C., Wang, Q. & Papineau, D. (2022). Abiotic anoxic iron oxidation, formation of Archean banded iron formations, and the oxidation of early Earth. *Earth and Planetary Science Letters*, *584*, 117469. https://doi.org/10.1016/j.epsl.2022.117469

Drever, J. I. (1974). Geochemical model for the origin of Precambrian banded iron formations. *Geological Society of America Bulletin*, *85*(7), 1099-1106. https://doi.org/10.1130/0016-7606(1974)85<1099:GMFTOO>2.0.CO;2

Ehrenreich, A., & Widdel, F. (1994). Anaerobic oxidation of ferrous iron by purple bacteria, a new type of phototrophic metabolism. *Applied and environmental microbiology*, 60(12), 4517-4526. https://doi.org/10.1128/aem.60.12.4517-4526.1994

Evans, D. A., Beukes, N. J., & Kirschvink, J. L. (1997). Low-latitude glaciation in the Palaeoproterozoic era. *Nature*, *386*(6622), 262-266. https://doi.org/10.1038/386262a0

Farquhar, J., Bao, H., & Thiemens, M. (2000). Atmospheric influence of Earth's earliest sulfur cycle. *Science*, *289*(5480), 756-758. http://doi.org/10.1126/science.289.5480.756

Gumsley, A. P., Chamberlain, K. R., Bleeker, W., Söderlund, U., De Kock, M. O., Larsson, E. R., & Bekker, A. (2017). Timing and tempo of the Great Oxidation Event. *Proceedings of the National Academy of Sciences*, *114*(8), 1811-1816. https://doi.org/10.1073/pnas.1608824114

Gutzmer, J., & Beukes, N. J. (1998). High-grade manganese ores in the Kalahari manganese field: Characterisation and dating of ore-forming events. *Unpublished Report. Rand Afrikaans University, Johannesburg*. http://doi.org/10.13140/RG.2.2.11342.66887

Halevy, I., Alesker, M., Schuster, E. M., Popovitz-Biro, R., & Feldman, Y. (2017). A key role for green rust in the Precambrian oceans and the genesis of iron formations. *Nature Geoscience*, 10(2), 135-139. https://doi.org/10.1038/ngeo2878

Haugaard, R., Ootes, L., Creaser, R. A., & Konhauser, K. O. (2016). The nature of Mesoarchaean seawater and continental weathering in 2.85 Ga banded iron formation, Slave craton, NW Canada. *Geochimica et Cosmochimica Acta*, *194*, 34-56. https://doi.org/10.1016/j.gca.2016.08.020

Hoffman, P. F. (2013). The Great Oxidation and a Siderian snowball Earth: MIF-S based correlation of Paleoproterozoic glacial epochs. *Chemical Geology*, *362*, 143-156. https://doi.org/10.1016/j.chemgeo.2013.04.018

Holland, H. D. (1973). The oceans; a possible source of iron in iron-formations. *Economic Geology*, *68*(7), 1169-1172. https://doi.org/10.2113/gsecongeo.68.7.1169

Horstmann, U. E., & Hälbich, I. W. (1995). Chemical composition of banded iron-formations of the Griqualand West Sequence, Northern Cape Province, South Africa, in comparison with other Precambrian iron formations. *Precambrian Research*, *72*(1-2), 109-145. https://doi.org/10.1016/0301-9268(94)00086-7

Imbrie, J., Boyle, E. A., Clemens, S. C., Duffy, A., Howard, W. R., Kukla, G., ... & Toggweiler, J. R. (1992). On the structure and origin of major glaciation cycles 1. Linear responses to Milankovitch forcing. *Paleoceanography*, *7*(6), 701-738. https://doi.org/10.1029/92PA02253

Isley, A. E. (1995). Hydrothermal plumes and the delivery of iron to banded iron formation. *The Journal of Geology*, *103*(2), 169-185. https://doi.org/10.1086/629734

Isley, A. E., & Abbott, D. H. (1999). Plume-related mafic volcanism and the deposition of banded iron formation. *Journal of Geophysical Research: Solid Earth*, 104(B7), 15461-15477. https://doi.org/10.1029/1999JB900066

Isson, T. T., & Planavsky, N. J. (2018). Reverse weathering as a long-term stabilizer of marine pH and planetary climate. *Nature*, 560(7719), 471-475. https://doi.org/10.1038/s41586-018-0408-4

Jacobsen, S. B., & Pimentel-Klose, M. R. (1988). A Nd isotopic study of the Hamersley and Michipicoten banded iron formations: the source of REE and Fe in Archean oceans. *Earth and Planetary Science Letters*, *87*(1-2), 29-44. https://doi.org/10.1016/0012-821X(88)90062-3

James, H. L. (1954). Sedimentary facies of iron-formation. *Economic Geology*, *49*(3), 235-293. https://doi.org/10.2113/gsecongeo.49.3.235

Jiao, Y., Kappler, A., Croal, L. R., & Newman, D. K. (2005). Isolation and characterization of a genetically tractable photoautotrophic Fe (II)-oxidizing bacterium, Rhodopseudomonas palustris strain TIE-1. *Applied and Environmental Microbiology*, 71(8), 4487-4496. https://doi.org/10.1128/AEM.71.8.4487-4496.2005

Johnson, J. E., Webb, S. M., Thomas, K., Ono, S., Kirschvink, J. L., & Fischer, W. W. (2013). Manganese-oxidizing photosynthesis before the rise of cyanobacteria. *Proceedings of the National Academy of Sciences*, *110*(28), 11238-11243. https://doi.org/10.1073/pnas.1305530110

Kamber, B. S., Whitehouse, M. J., Bolhar, R., & Moorbath, S. (2005). Volcanic resurfacing and the early terrestrial crust: zircon U–Pb and REE constraints from the Isua Greenstone Belt, southern West Greenland. *Earth and Planetary Science Letters*, *240*(2), 276-290. https://doi.org/10.1016/j.epsl.2005.09.037

Kappler, A., Pasquero, C., Konhauser, K. O., & Newman, D. K. (2005). Deposition of banded iron formations by anoxygenic phototrophic Fe (II)-oxidizing bacteria. *Geology*, *33*(11), 865-868. https://doi.org/10.1130/G21658.1

Kasting, J. F. (1991). Box models for the evolution of atmospheric oxygen: an update. *Global and planetary change*, *5*(1-2), 125-131. https://doi.org/10.1016/0921-8181(91)90133-H

Kaufman, A. J. (2014). Cyanobacteria at work. *Nature Geoscience*, *7*(4), 253-254. https://doi.org/10.1038/ngeo2128

Kirkbride, M. P. (2002). Processes of glacial transportation. *Modern and past glacial environments*, 147-169. https://doi.org/10.1016/B978-075064226-2/50009-X

Kirschvink, J. L. (1992). Late Proterozoic low-latitude global glaciation: the snowball Earth. https://resolver.caltech.edu/CaltechAUTHORS:20130117-100718783

Kirschvink, J. L. (2005). Red Earth, White Earth, Green Earth, Black Earth. *Engineering and Science*, *68*(4), 10-20. https://resolver.caltech.edu/CaltechAUTHORS:20130108-131707037

Kirschvink, J. L., Gaidos, E. J., Bertani, L. E., Beukes, N. J., Gutzmer, J., Maepa, L. N., & Steinberger, R. E. (2000). Paleoproterozoic snowball Earth: Extreme climatic and geochemical global change and its biological consequences. *Proceedings of the National Academy of Sciences*, *97*(4), 1400-1405. https://doi.org/10.1073/pnas.97.4.1400

Klein, C. (2005). Some Precambrian banded iron-formations (BIFs) from around the world: Their age, geologic setting, mineralogy, metamorphism, geochemistry, and origins. *American Mineralogist*, *90*(10), 1473-1499. https://doi.org/10.2138/am.2005.1871

Klein, C., & Beukes, N. J. (1989). Geochemistry and sedimentology of a facies transition from limestone to iron-formation deposition in the early Proterozoic Transvaal Supergroup, South Africa. *Economic Geology*, *84*(7), 1733-1774. https://doi.org/10.2113/gsecongeo.84.7.1733

Konhauser, K. O., Hamade, T., Raiswell, R., Morris, R. C., Ferris, F. G., Southam, G., & Canfield, D. E. (2002). Could bacteria have formed the Precambrian banded iron formations?. *Geology*, *30*(12), 1079-1082. https://doi.org/10.1130/0091-7613(2002)030<1079:CBHFTP>2.0.CO;2

Konhauser, K. O., Newman, D. K., & Kappler, A. (2005). The potential significance of microbial Fe (III) reduction during deposition of Precambrian banded iron formations. *Geobiology*, *3*(3), 167-177. https://doi.org/10.1111/j.1472-4669.2005.00055.x

Konhauser, K. O., Planavsky, N. J., Hardisty, D. S., Robbins, L. J., Warchola, T. J., Haugaard, R., ... & Johnson, C. M. (2017). Iron formations: A global record of Neoarchaean to Palaeoproterozoic environmental history. *Earth-Science Reviews*, *172*, 140-177. https://doi.org/10.1016/j.earscirev.2017.06.012

Konhauser, K. O., Pecoits, E., Lalonde, S. V., Papineau, D., Nisbet, E. G., Barley, M. E., ... & Kamber, B. S. (2009). Oceanic nickel depletion and a methanogen famine before the Great Oxidation Event. *Nature*, 458(7239), 750-753. https://doi.org/10.1038/nature07858

Kopp, R. E., Kirschvink, J. L., Hilburn, I. A., & Nash, C. Z. (2005). The Paleoproterozoic snowball Earth: a climate disaster triggered by the evolution of oxygenic photosynthesis. *Proceedings of the National Academy of Sciences*, *102*(32), 11131-11136. https://doi.org/10.1073/pnas.050487810

Lantink, M. L., Davies, J. H., Mason, P. R., Schaltegger, U., & Hilgen, F. J. (2019). Climate control on banded iron formations linked to orbital eccentricity. *Nature geoscience*, *12*(5), 369-374. https://doi.org/10.1038/s41561-019-0332-8

Lantink, M. L., Lenstra, W. K., Davies, J. H., Hennekam, R., Martin, D. M., Mason, P. R., ... & Hilgen, F. J. (2023). Precessional pacing of early Proterozoic redox cycles. *Earth and Planetary Science Letters*, *610*, 118117. https://doi.org/10.1016/j.epsl.2023.118117

Le Heron, D. P., Busfield, M. E., Smith, A. J., & Wimmer, S. (2022). A grounding zone wedge origin for the Palaeoproterozoic Makganyene Formation of South Africa. *Frontiers in Earth Science*, 10, 905602. https://doi.org/10.3389/feart.2022.905602

Lepp, H., & Goldich, S. S. (1964). Origin of Precambrian iron formations. *Economic Geology*, *59*(6), 1025-1060. https://doi.org/10.2113/gsecongeo.59.6.1025

Li, W., Beard, B. L., & Johnson, C. M. (2015). Biologically recycled continental iron is a major component in banded iron formations. *Proceedings of the National Academy of Sciences*, *112*(27), 8193-8198. https://doi.org/10.1073/pnas.1505515112

Markonis, Y., & Koutsoyiannis, D. (2013). Climatic variability over time scales spanning nine orders of magnitude: Connecting Milankovitch cycles with Hurst–Kolmogorov dynamics. *Surveys in Geophysics*, *34*(2), 181-207. https://doi.org/10.1007/s10712-012-9208-9

Marshall, H. G., Walker, J. C., & Kuhn, W. R. (1988). Long-term climate change and the geochemical cycle of carbon. *Journal of Geophysical Research: Atmospheres*, *93*(D1), 791-801. https://doi.org/10.1029/JD093iD01p00791

Melezhik, V. A. (2006). Multiple causes of Earth's earliest global glaciation. *Terra Nova*, *18*(2), 130-137. https://doi.org/10.1111/j.1365-3121.2006.00672.x

Moore, J. M., Polteau, S., Armstrong, R. A., Corfu, F., & Tsikos, H. (2012). The age and correlation of the Postmasburg Group, southern Africa: Constraints from detrital zircon grains. *Journal of African Earth Sciences*, *64*, 9-19. https://doi.org/10.1016/j.jafrearsci.2011.11.001

Moore, J. M., Tsikos, H., & Polteau, S. (2001). Deconstructing the Transvaal Supergroup, south Africa: implications for Palaeoproterozoic palaeoclimate models. *Journal of African Earth Sciences*, *33*(3-4), 437-444. https://doi.org/10.1016/S0899-5362(01)00084-7

Morris, R. C. (1980). A textural and mineralogical study of the relationship of iron ore to banded iron-formation in the Hamersley Iron Province of Western Australia. *Economic Geology*, *75*(2), 184-209. https://doi.org/10.2113/gsecongeo.75.2.184

Nelson, D. R., Trendall, A. F., & Altermann, W. (1999). Chronological correlations between the Pilbara and Kaapvaal cratons. *Precambrian Research*, *97*(3-4), 165-189. https://doi.org/10.1016/S0301-9268(99)00031-5

Oonk, P. B. H. (2017). Fraction-specific geochemistry across the Asbestos Hills Bif of the Transvaal Supergroup, South Africa (thesis). http://hdl.handle.net/10962/50721

Oonk, P. B., Tsikos, H., Mason, P. R., Henkel, S., Staubwasser, M., Fryer, L., ... & Williams, H. M. (2017). Fraction-specific controls on the trace element distribution in iron formations: Implications for trace metal stable isotope proxies. *Chemical Geology*, *474*, 17-32. https://doi.org/10.1016/j.chemgeo.2017.10.018

Pavlov, A. A., Kasting, J. F., Brown, L. L., Rages, K. A., & Freedman, R. (2000). Greenhouse warming by CH4 in the atmosphere of early Earth. *Journal of Geophysical Research: Planets*, *105*(E5), 11981-11990. https://doi.org/10.1029/1999JE001134

Pecoits, E., Smith, M. L., Catling, D. C., Philippot, P., Kappler, A., & Konhauser, K. O. (2015). Atmospheric hydrogen peroxide and Eoarchean iron formations. *Geobiology*, 13(1), 1-14. https://doi.org/10.1111/gbi.12116

Percak-Dennett, E. M., Beard, B. L., Xu, H., Konishi, H., Johnson, C. M., & Roden, E. E. (2011). Iron isotope fractionation during microbial dissimilatory iron oxide reduction in simulated Archaean seawater. *Geobiology*, 9(3), 205-220. https://doi.org/10.1111/j.1472-4669.2011.00277.x

Pickard, A. L. (2003). SHRIMP U–Pb zircon ages for the Palaeoproterozoic Kuruman Iron Formation, northern Cape Province, South Africa: evidence for simultaneous BIF deposition on Kaapvaal and Pilbara cratons. *Precambrian Research*, 125(3-4), 275-315. https://doi.org/10.1016/S0301-9268(03)00113-X

Planavsky, N. J., Asael, D., Hofmann, A., Reinhard, C. T., Lalonde, S. V., Knudsen, A., ... & Rouxel, O. J. (2014). Evidence for oxygenic photosynthesis half a billion years before the Great Oxidation Event. *Nature Geoscience*, *7*(4), 283-286. https://doi.org/10.1038/ngeo2122

Planavsky, N., Bekker, A., Rouxel, O. J., Kamber, B., Hofmann, A., Knudsen, A., & Lyons, T. W. (2010). Rare earth element and yttrium compositions of Archean and Paleoproterozoic Fe formations revisited: new perspectives on the significance and mechanisms of

deposition. Geochimica et Cosmochimica Acta, 74(22), 6387-6405.
https://doi.org/10.1016/j.gca.2010.07.021

Polteau, S., Moore, J. M., & Tsikos, H. (2006). The geology and geochemistry of the
Palaeoproterozoic Makganyene diamictite. *Precambrian Research*, *148*(3-4), 257-274.
https://doi.org/10.1016/j.precamres.2006.05.003

Rampino, M. R., & Self, S. (1992). Volcanic winter and accelerated glaciation following the
Toba super-eruption. *Nature*, *359*(6390), 50-52. https://doi.org/10.1038/359050a0

Rao, T. G., & Naqvi, S. M. (1995). Geochemistry, depositional environment and tectonic
setting of the BIF's of the Late Archaean Chitradurga Schist Belt, India. *Chemical
Geology*, 121(1-4), 217-243. https://doi.org/10.1016/0009-2541(94)00116-P

Rasmussen, B., Krapež, B., Muhling, J. R., & Suvorova, A. (2015). Precipitation of iron silicate
nanoparticles in early Precambrian oceans marks Earth's first iron age. *Geology*, 43(4), 303-
306. https://doi.org/10.1130/G36309.1

Roberts, J. D. (1976). Late Precambrian dolomites, Vendian glaciation, and synchroneity of
Vendian glaciations. *The Journal of Geology*, *84*(1), 47-63. https://doi.org/10.1086/628173

Rosing, M. T., & Frei, R. (2004). U-rich Archaean sea-floor sediments from Greenland–
indications of> 3700 Ma oxygenic photosynthesis. *Earth and Planetary Science
Letters*, *217*(3-4), 237-244. https://doi.org/10.1016/S0012-821X(03)00609-5

Senger, M. H., Davies, J. H. F. L., Ovtcharova, M., Beukes, N., Gumsley, A., Gaynor, S. P., ... &
Schaltegger, U. (2023). Improving the chronostratigraphic framework of the Transvaal
Supergroup (South Africa) through in-situ and high-precision U-Pb
geochronology. *Precambrian Research*, 392, 107070.
https://doi.org/10.1016/j.precamres.2023.107070

Schirrmeister, B. E., de Vos, J. M., Antonelli, A., & Bagheri, H. C. (2013). Evolution of
multicellularity coincided with increased diversification of cyanobacteria and the Great
Oxidation Event. *Proceedings of the National Academy of Sciences*, *110*(5), 1791-1796.
https://doi.org/10.1073/pnas.1209927110

Schrag, D. P., Berner, R. A., Hoffman, P. F., & Halverson, G. P. (2002). On the initiation of a snowball Earth. *Geochemistry, Geophysics, Geosystems*, 3(6), 1-21. https://doi.org/10.1029/2001GC000219

Siahi, M., Tsikos, H., Rafuza, S., Oonk, P. B., Mhlanga, X. R., van Niekerk, D., ... & Harris, C. (2020). Insights into the processes and controls on the absolute abundance and distribution of manganese in Precambrian iron formations. *Precambrian Research*, *350*, 105878. https://doi.org/10.1016/j.precamres.2020.105878

Steiner, J., & Grillmair, E. (1973). Possible galactic causes for periodic and episodic glaciations. *Geological Society of America Bulletin*, 84(3), 1003-1018. https://doi.org/10.1130/0016-7606(1973)84<1003:PGCFPA>2.0.CO;2

Sun, S., Konhauser, K. O., Kappler, A., & Li, Y. L. (2015). Primary hematite in Neoarchean to Paleoproterozoic oceans. *GSA Bulletin*, *127*(5-6), 850-861. https://doi.org/10.1130/B31122.1

Thomas, G. S. P., & Summers, A. J. (1981). Drop-stone and allied structures from Pleistocene waterlain till at Ely House, County Wexford. *Journal of Earth Sciences*, 109-119. http://www.jstor.org/stable/30002360.

Trendall, A. F. (2002). The significance of iron-formation in the Precambrian stratigraphic record. *Precambrian sedimentary environments: A modern approach to ancient depositional systems*, 33-66. https://doi.org/10.1002/9781444304312.ch3

Trendall, A. F., & Blockey, J. B. (1970). The iron formations of the Precambrian Hamersley Group, Western Australia with special reference to the associated crocidolite (Vol. 119). *Geological Survey of Western Australia*.

Tsikos, H., Siahi, M., Rafuza, S., Mhlanga, X. R., Oonk, P. B. H., Papadopoulos, V., ... & Lyons, T. W. (2022). Carbon isotope stratigraphy of Precambrian iron formations and possible significance for the early biological pump. *Gondwana Research*, 109, 416-428. https://doi.org/10.1016/j.gr.2022.05.007

Visser, J. N. J. (1971). The deposition of the Griquatown glacial member in the Transvaal Supergroup. *South African Journal of Geology*, 74(3), 187-199.

Von Brunn, V., & Gold, D. J. C. (1993). Diamictite in the Archaean Pongola sequence of southern Africa. *Journal of African Earth Sciences (and the Middle East)*, *16*(3), 367-374. https://doi.org/10.1016/0899-5362(93)90056-V

Young, G. M. (1991). The Geologic Record of Glaciation: Relevance to the Climatic History of Earth. *Geoscience Canada*, 18(3). Retrieved from https://journals.lib.unb.ca/index.php/GC/article/view/3731

Young, G. M., Brunn, V. V., Gold, D. J., & Minter, W. E. L. (1998). Earth's oldest reported glaciation: physical and chemical evidence from the Archean Mozaan Group (~2.9 Ga) of South Africa. *The Journal of Geology*, 106(5), 523-538. https://doi.org/10.1086/516039

Young, G. M., & Long, D. G. F. (1976). Ice-wedge casts from the Huronian Ramsay Lake formation (> 2,300 my old) near Espanola, Ontario, Canada. *Palaeogeography, Palaeoclimatology, Palaeoecology*, *19*(3), 191-200. https://doi.org/10.1016/0031-0182(76)90013-4

Zheng, X. Y., Beard, B. L., Reddy, T. R., Roden, E. E., & Johnson, C. M. (2016). Abiologic silicon isotope fractionation between aqueous Si and Fe (III)–Si gel in simulated Archean seawater: Implications for Si isotope records in Precambrian sedimentary rocks. *Geochimica et Cosmochimica Acta*, 187, 102-122. https://doi.org/10.1016/j.gca.2016.05.012

8. Appendix

8.1 Appendix I - Drill core photos

8.1.1 AARPAN core

8.1.2 ERIN

8.1.3 LONDON

8.1.4 HEX
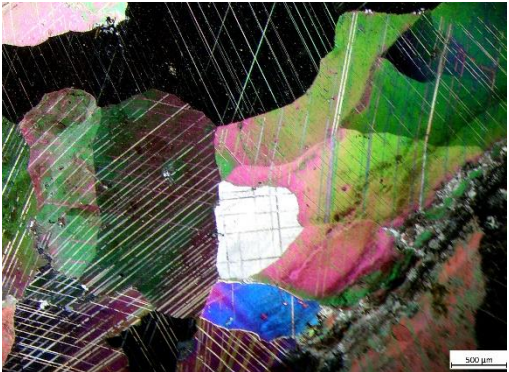
Figure
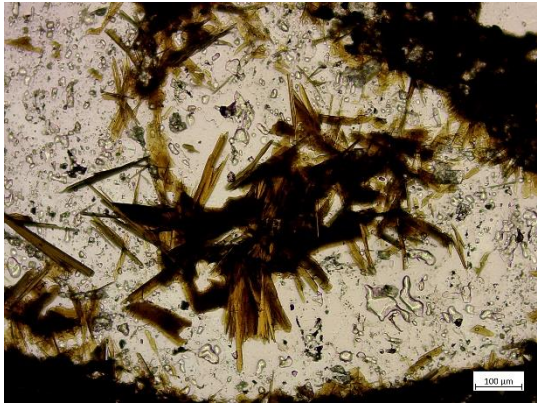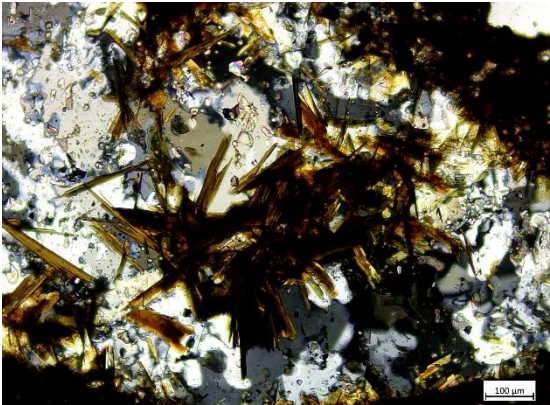
8.2 Appendix II - Minerals

Quartz	AARPAN - TS1
PPL	XPL
Scale bar: 100 μm	Scale bar: 100 μm

Chert	HEX - TS20
PPL	XPL
Scale bar: 500 μm	Scale bar: 500 μm

Calcite	AARPAN - TS1
PPL	XPL
Scale bar: 500 µm	Scale bar: 500 µm

Stilpnomelane	LONDON - TS12
PPL	XPL
Scale bar: 100 µm	Scale bar: 100 µm

8.3 Appendix III - Thin sections

AARPAN - TS1
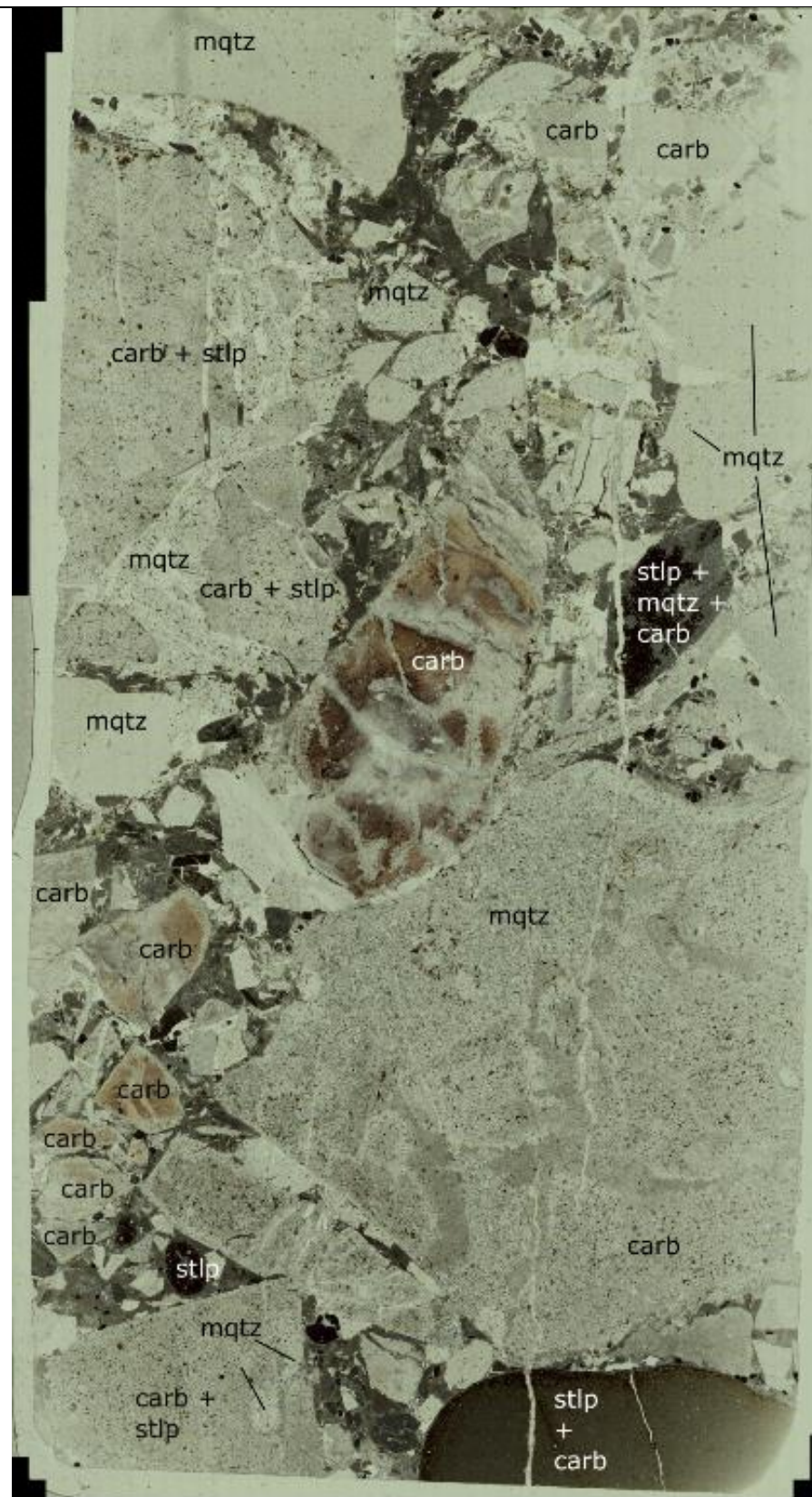
Scan size is approximately 2x4 cm
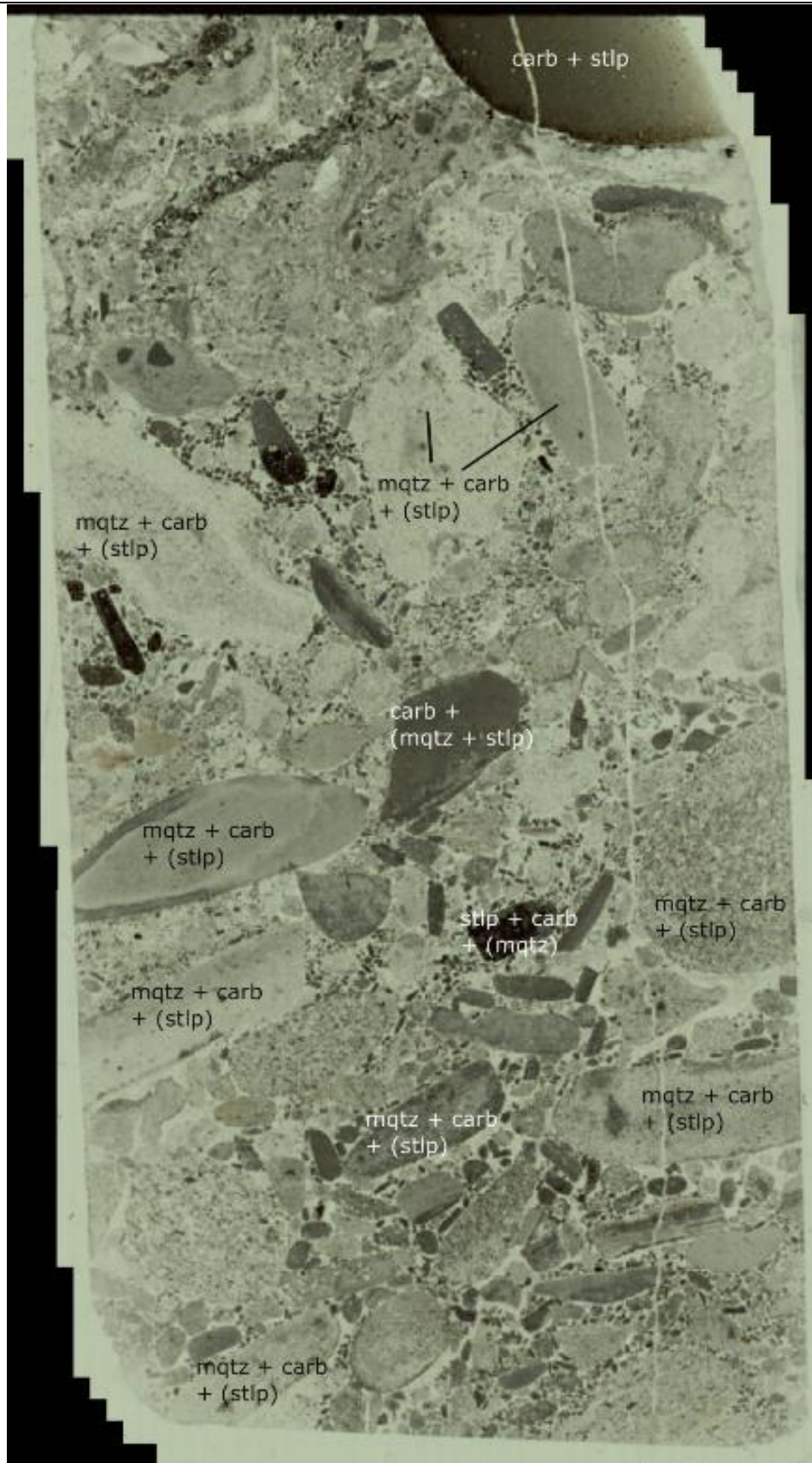
AARPAN - TS2

Scan size is approximately 2x4 cm

AARPAN - TS3

Scan size is approximately 2x4 cm
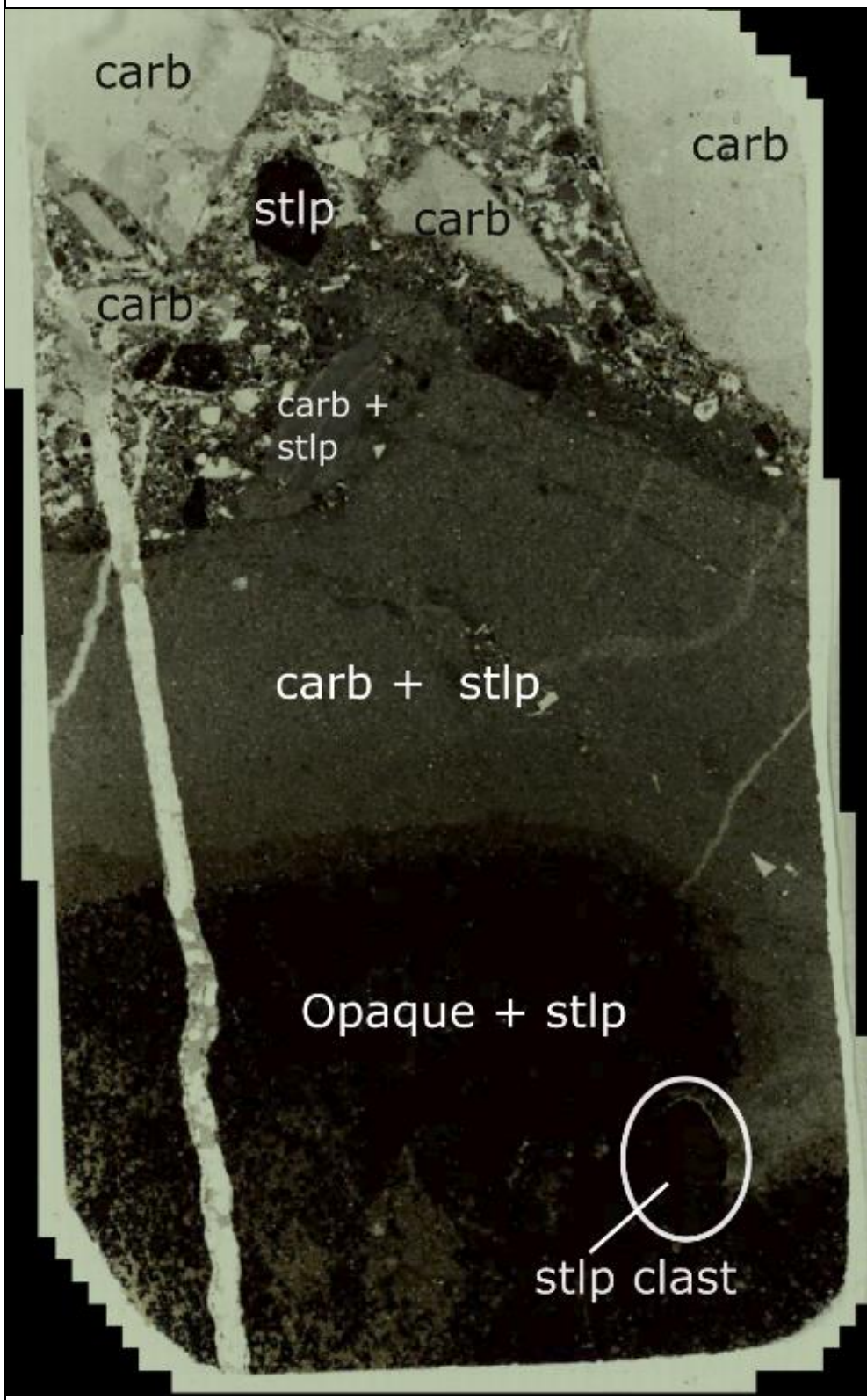
AARPAN - TS4

Scan size is approximately 2x4 cm
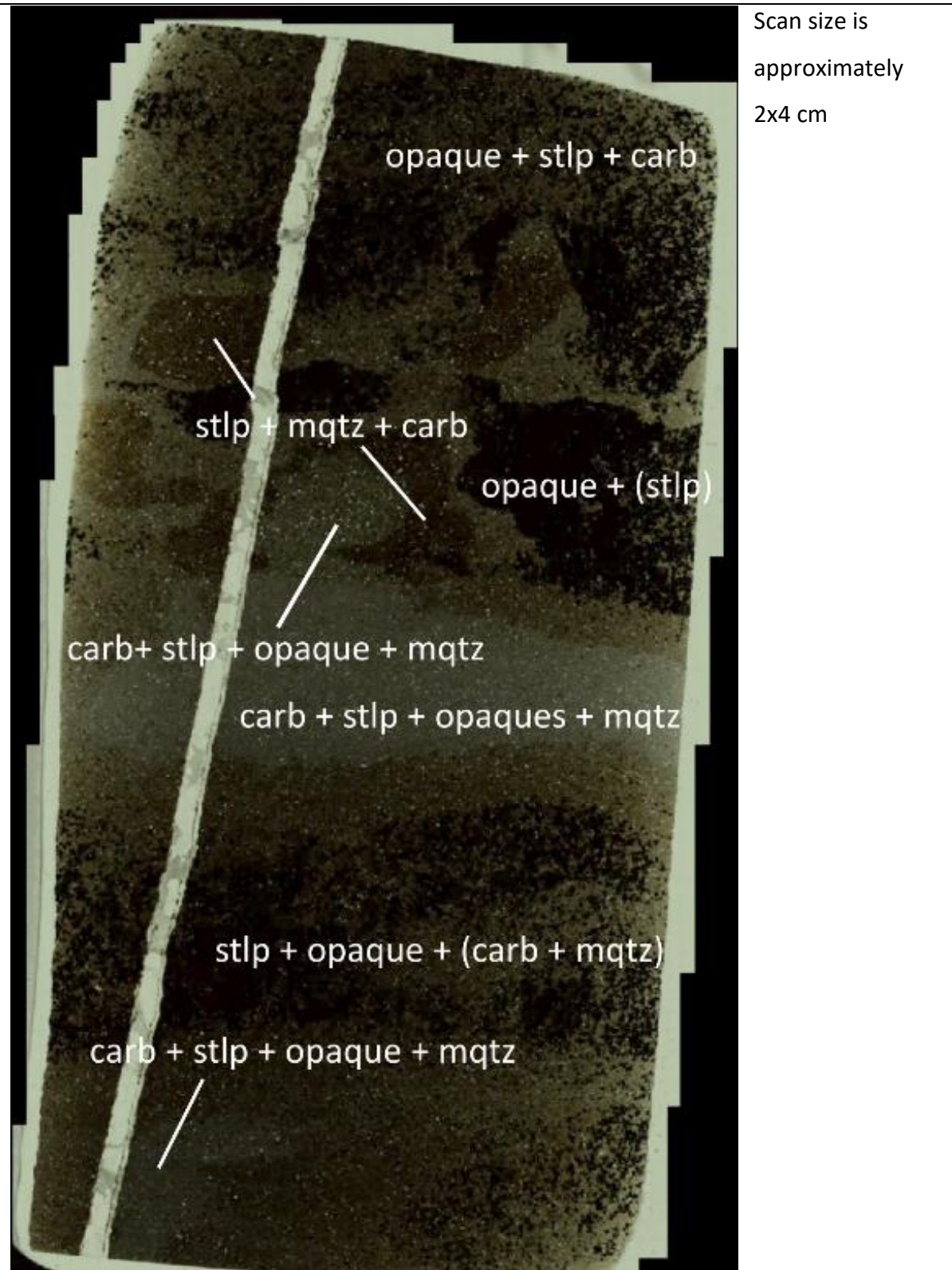
AARPAN - TS5
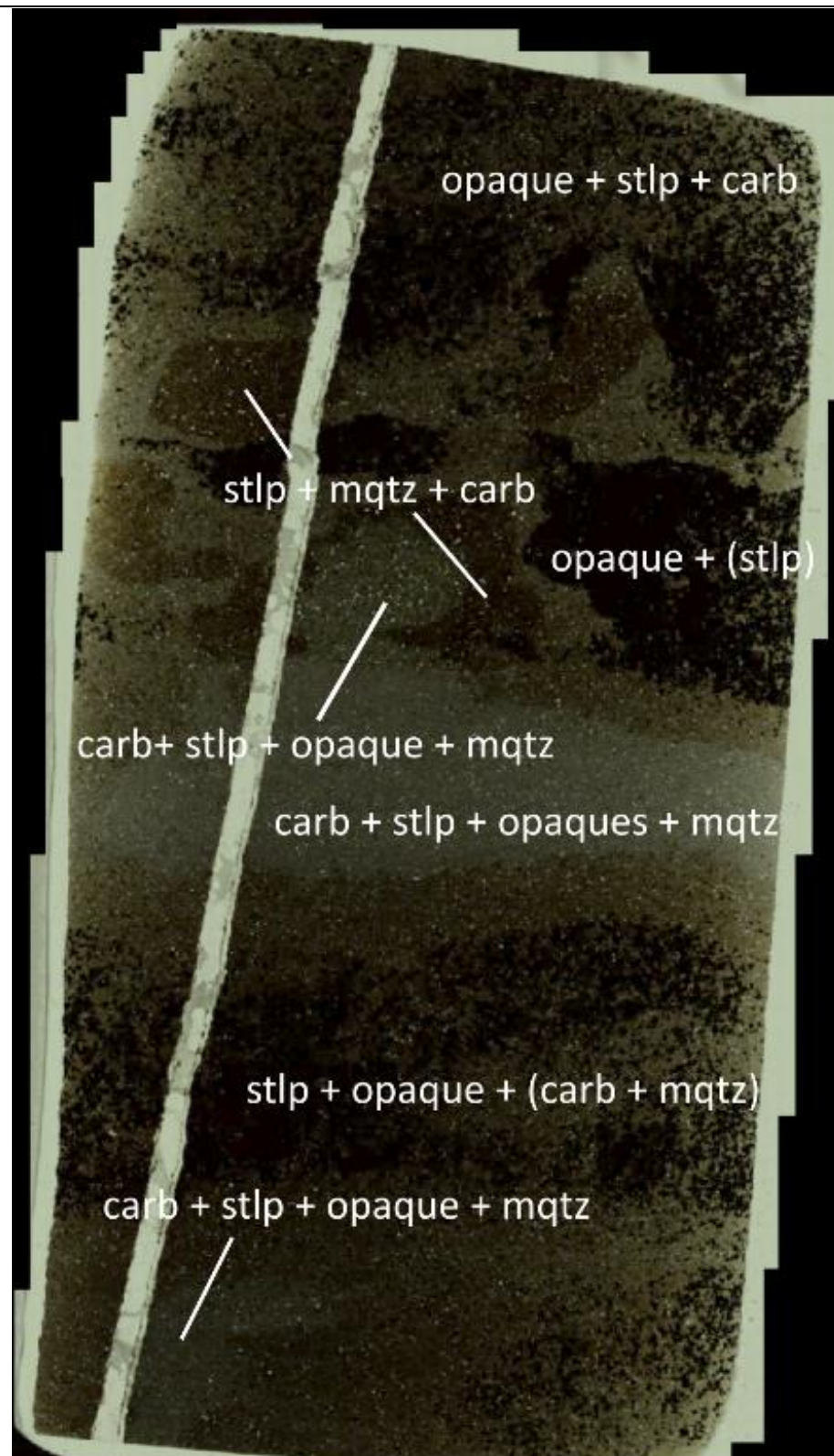
Scan size is approximately 2x4 cm

opaque + stlp + carb

stlp + mqtz + carb

opaque + (stlp)

carb+ stlp + opaque + mqtz

carb + stlp + opaques + mqtz

stlp + opaque + (carb + mqtz)

carb + stlp + opaque + mqtz
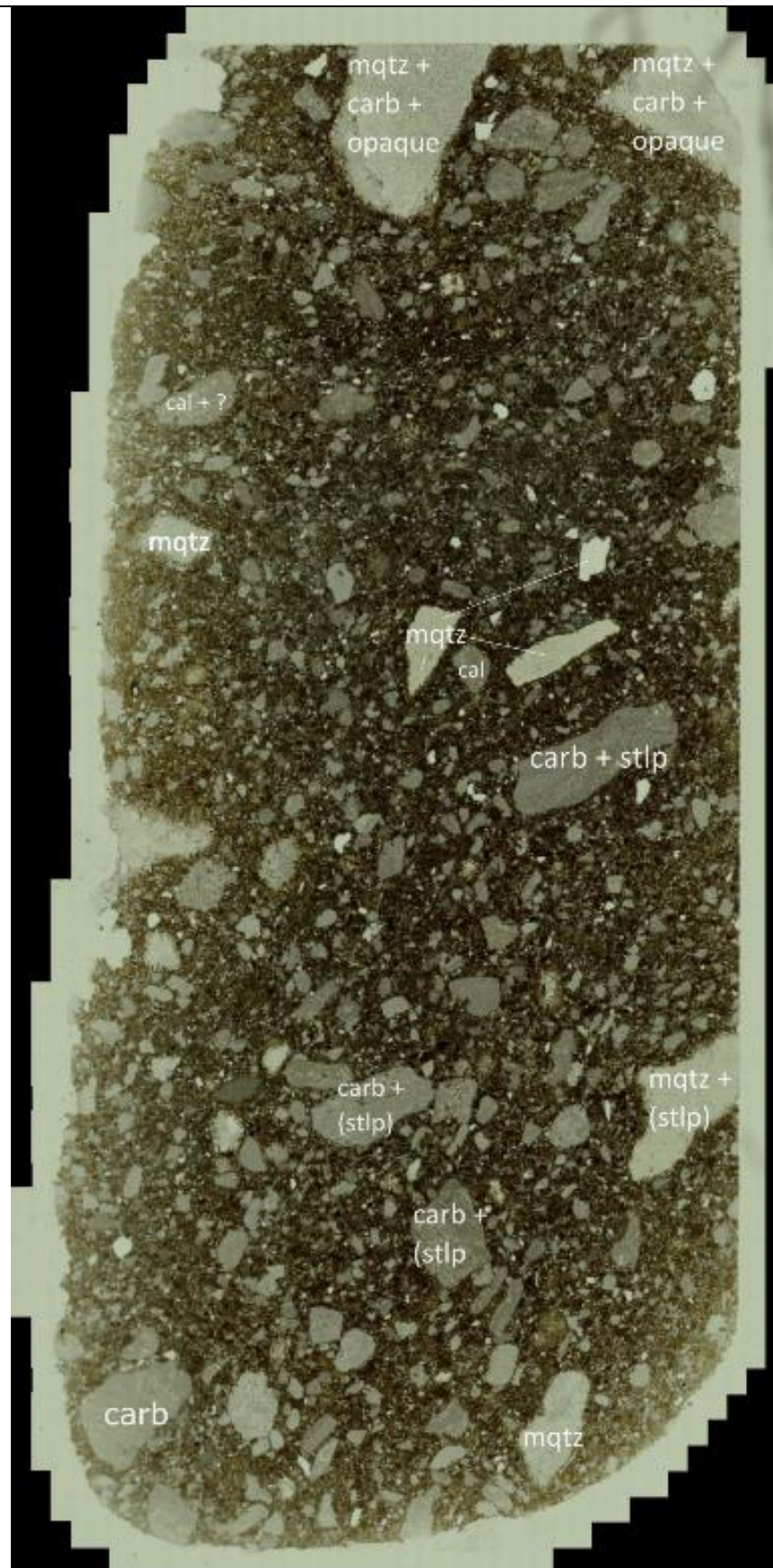
ERIN - TS6

Scan size is approximately 2x4 cm
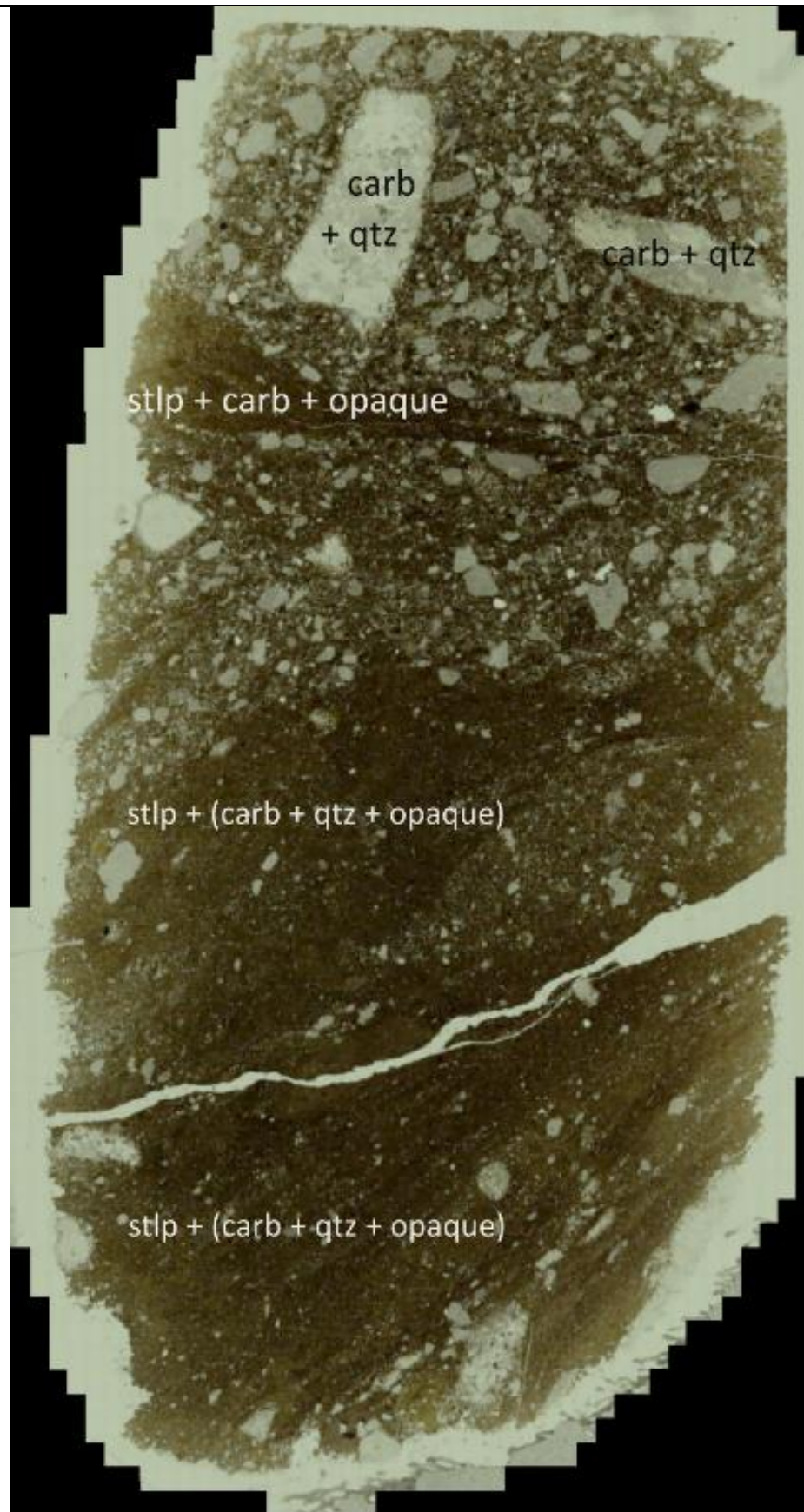
ERIN - TS7

Scan size is approximately 2x4 cm
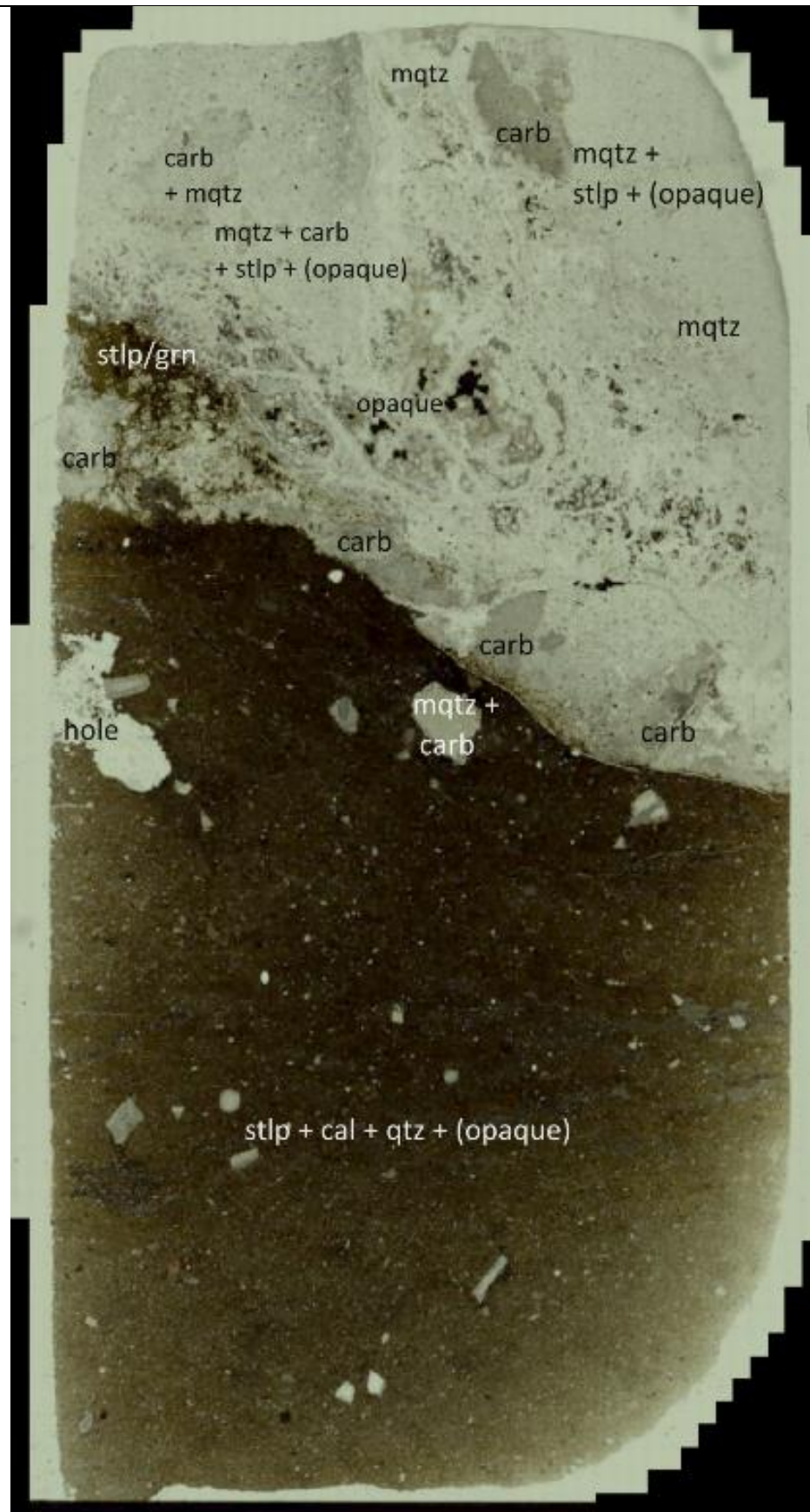
ERIN - TS8

Scan size is approximately 2x4 cm

ERIN - TS9

Scan size is approximately 2x4 cm
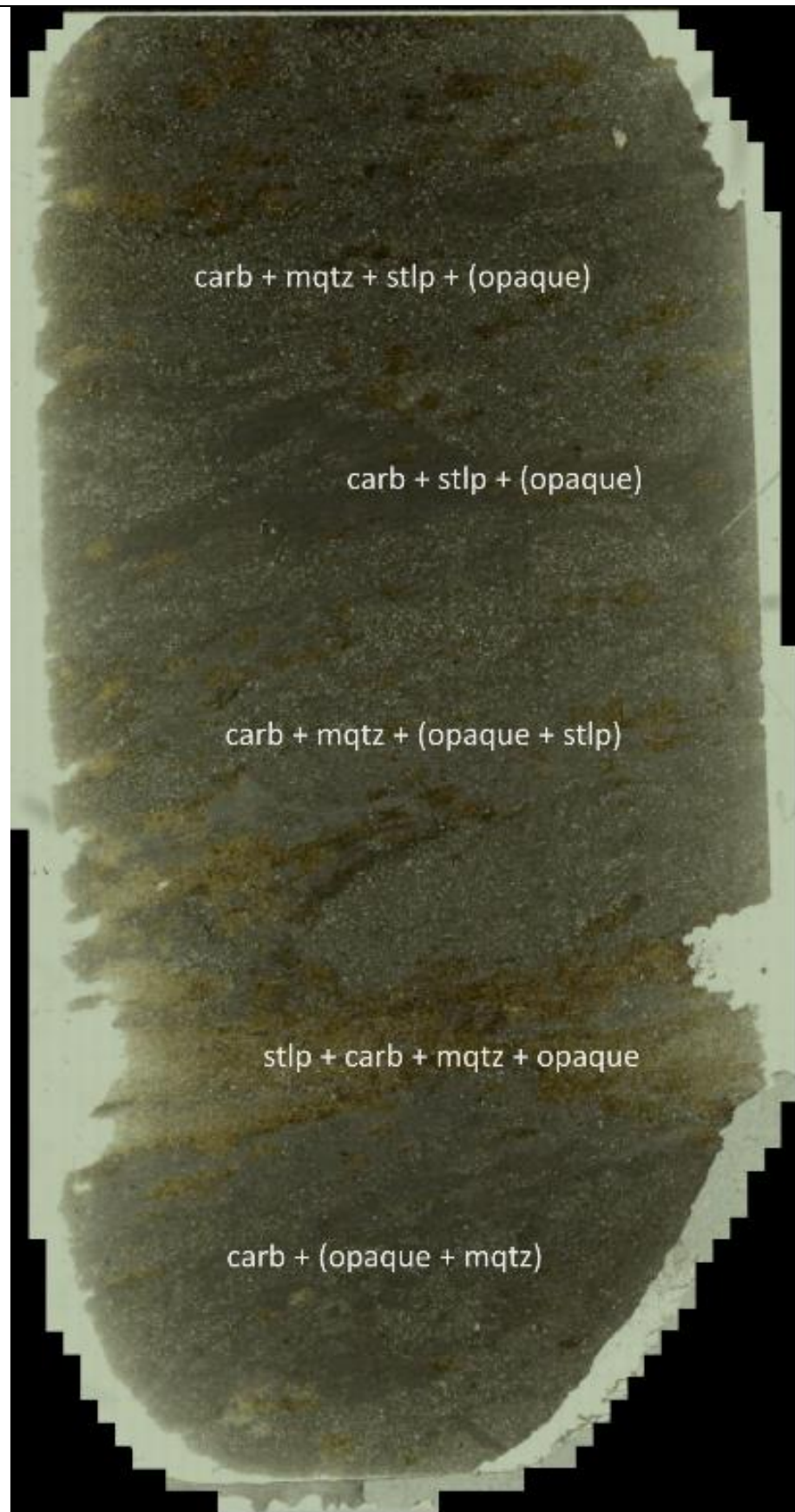
stlp + (carb + mqtz + opaque))

carb + stlp + (mqtz + opaque)

stlp + (mqtz + opaque)

carb + stlp + (mqtz + opaque)

ERIN - TS10

Scan size is approximately 2x4 cm

carb + mqtz + stlp + (opaque)

carb + stlp + (opaque)

carb + mqtz + (opaque + stlp)

stlp + carb + mqtz + opaque

carb + (opaque + mqtz)

ERIN - TS11
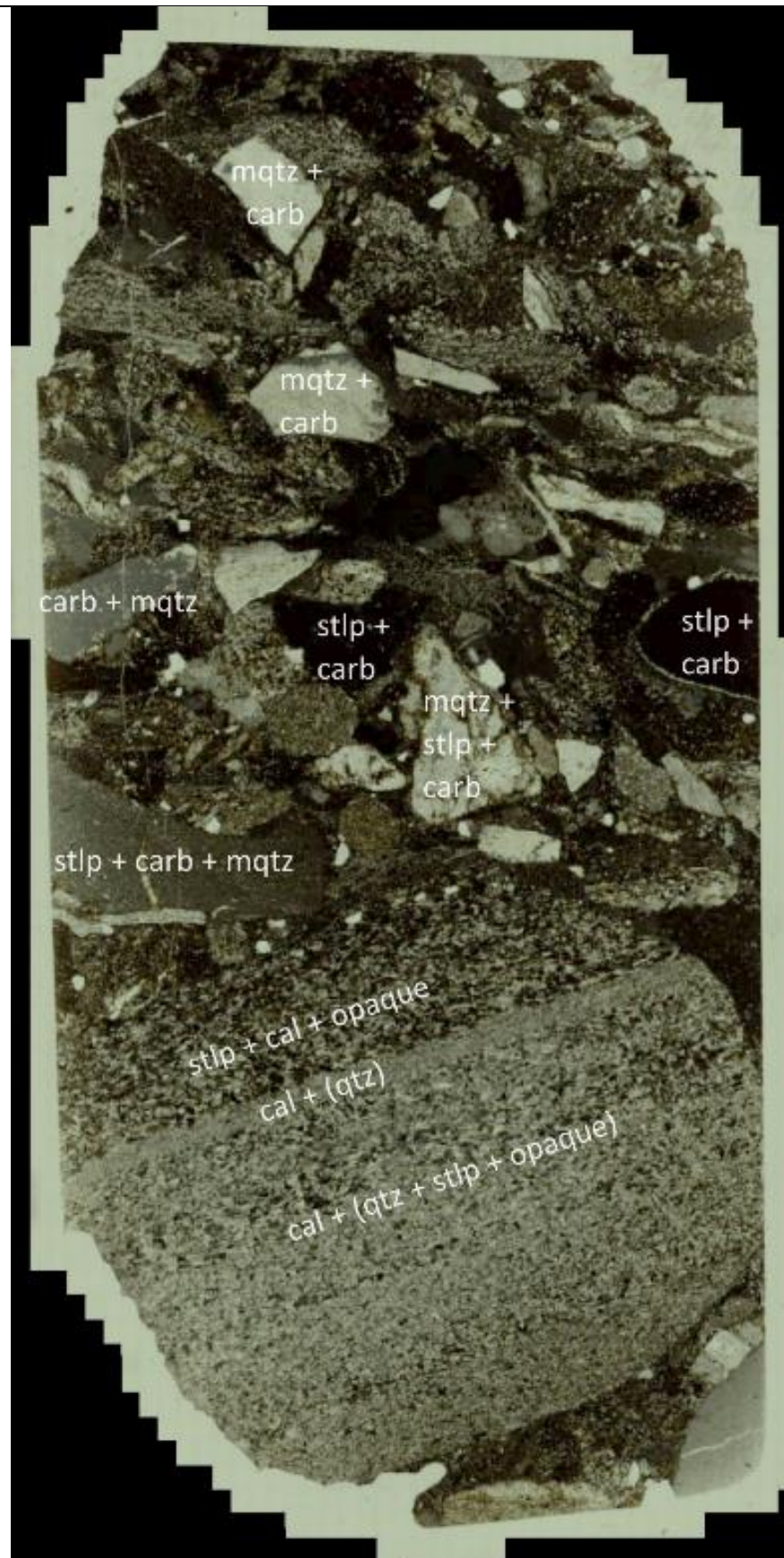
Scan size is approximately 2x4 cm

LONDON - TS12

Scan size is approximately 2x4 cm
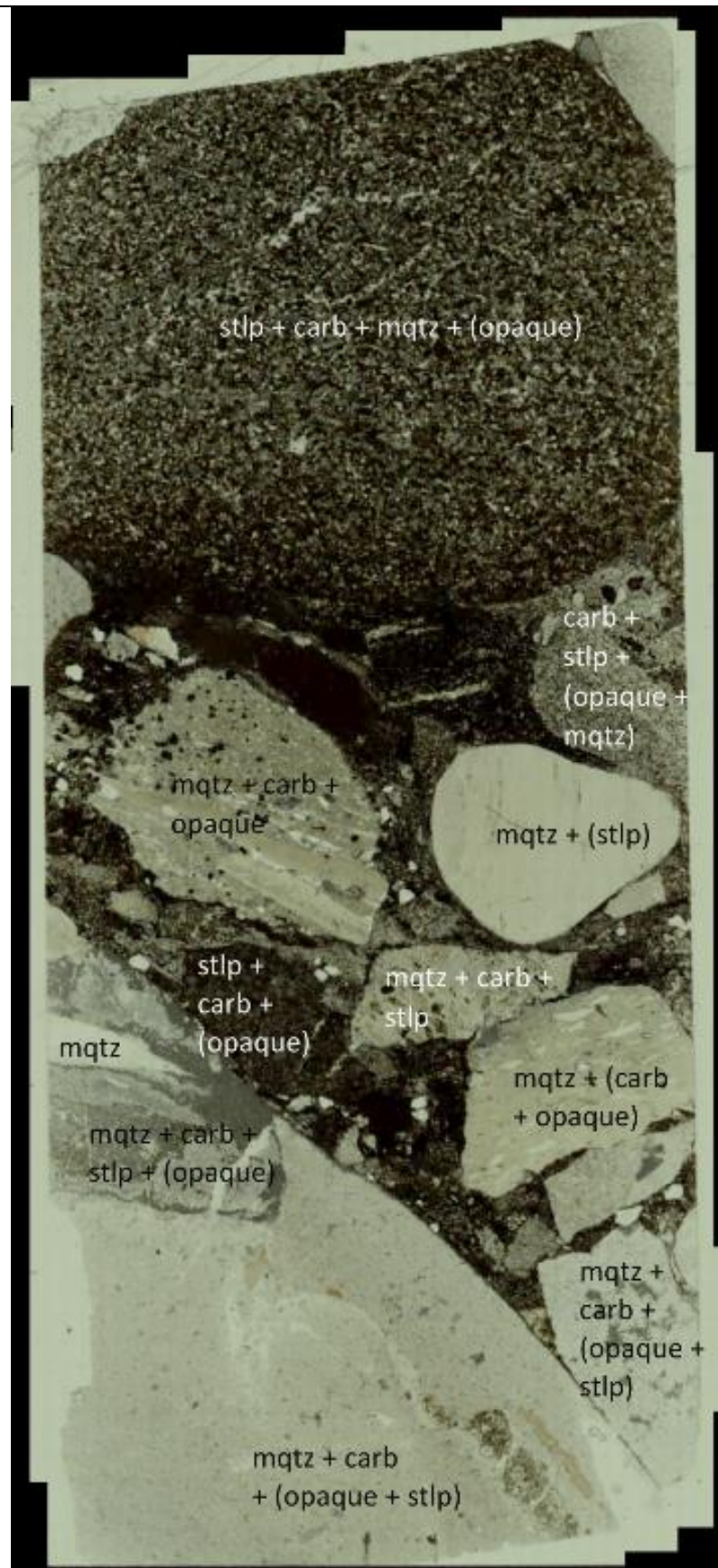
LONDON - TS13

Scan size is approximately 2x4 cm
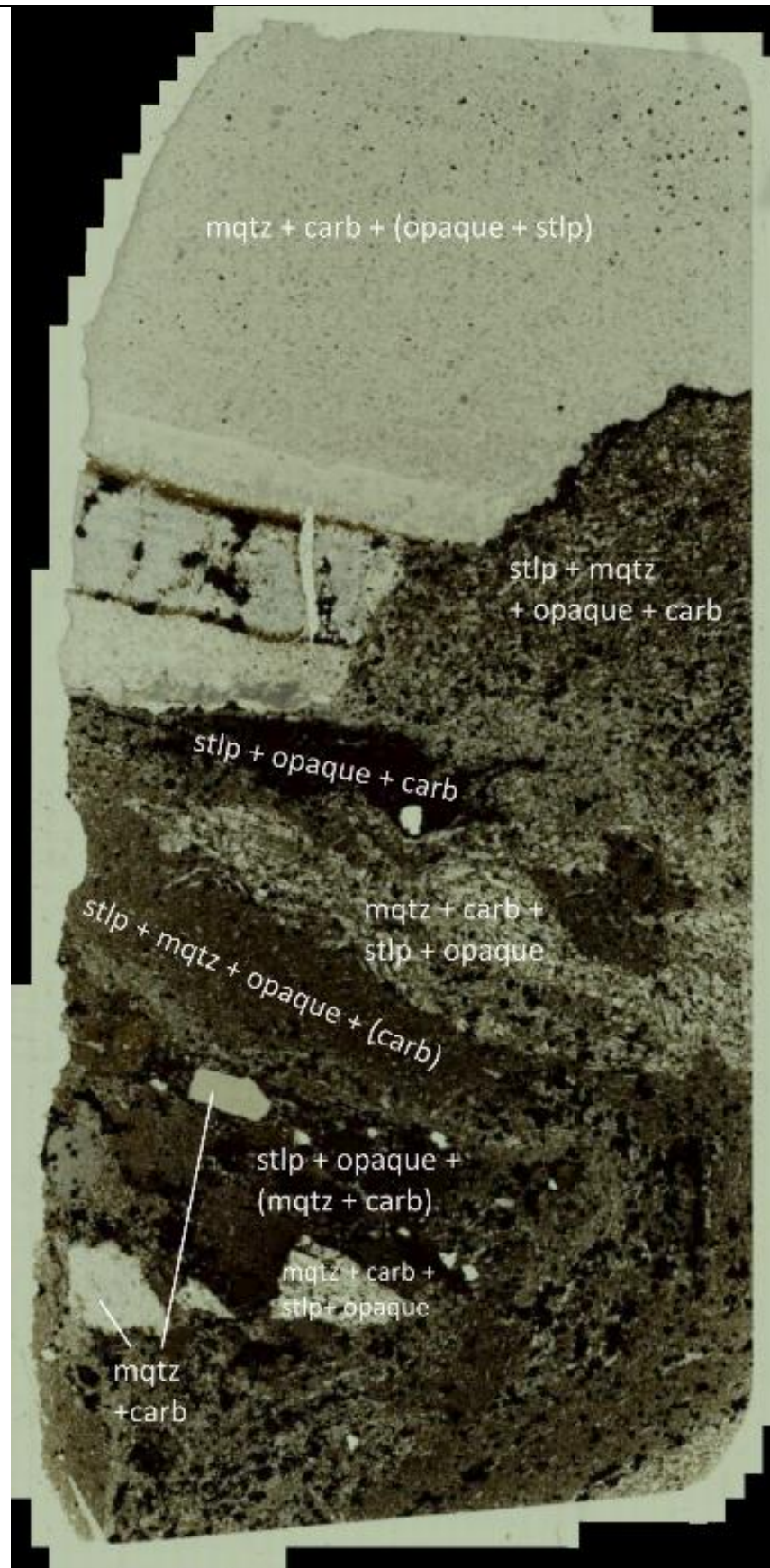
LONDON - TS14

Scan size is approximately 2x4 cm
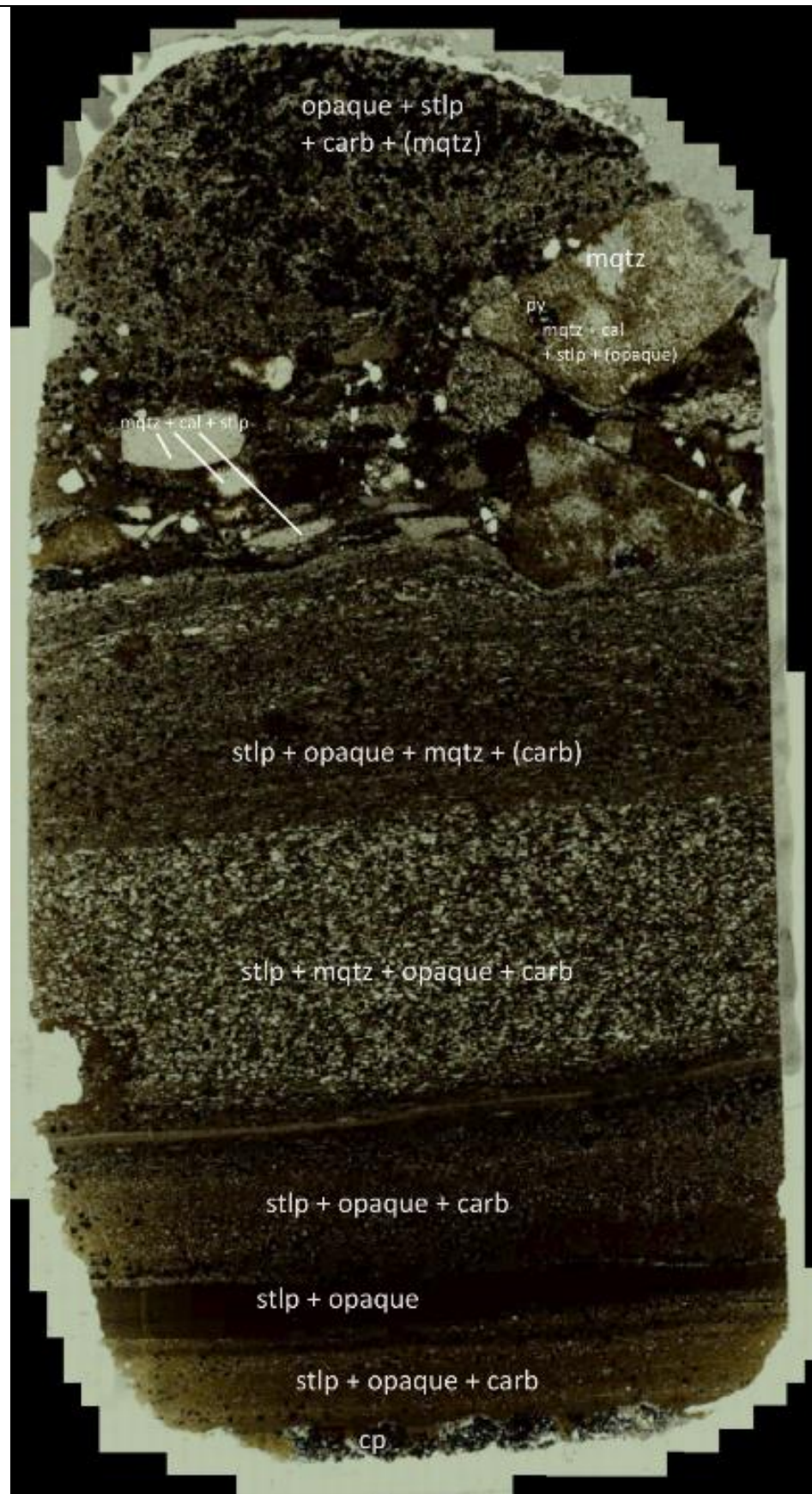
LONDON - TS15

Scan size is approximately 2x4 cm

LONDON - TS16

Scan size is approximately 2x4 cm

stlp + opaque + carb +(mqtz)

stlp + opaque + (carb + mqtz)

stlp + opaque + carb + (mqtz)

stlp + opaque + carb + (mqtz)

stlp + cal + opaque + (mqtz)
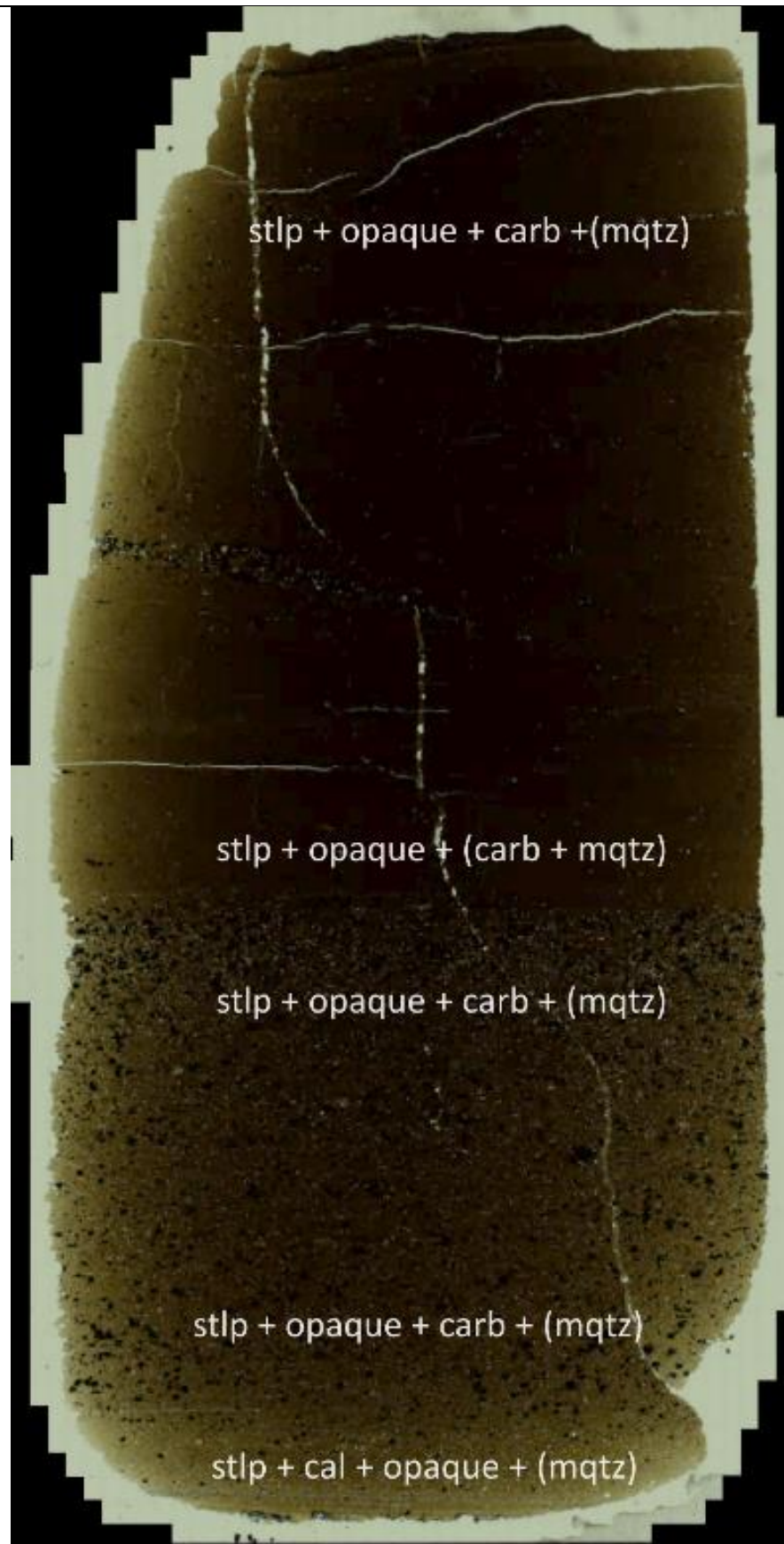
LONDON - TS17

Scan size is

approximately 2x4 cm

carb + stlp + opaque + (mqtz)

mqtz + carb + (opaque + stlp)

stlp + opaque + (mqtz + carb)

mqtz + carb + (opaque + stlp)
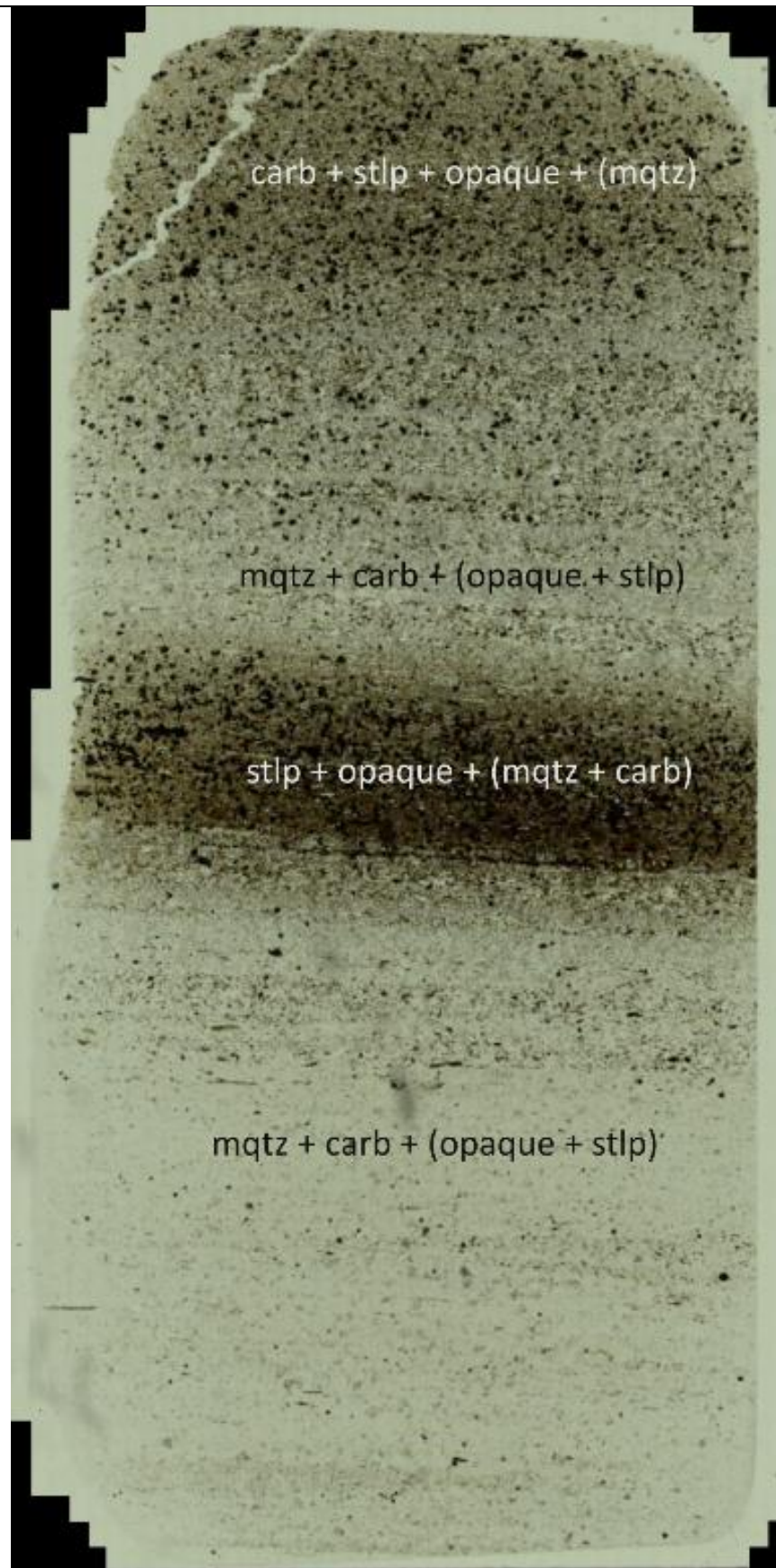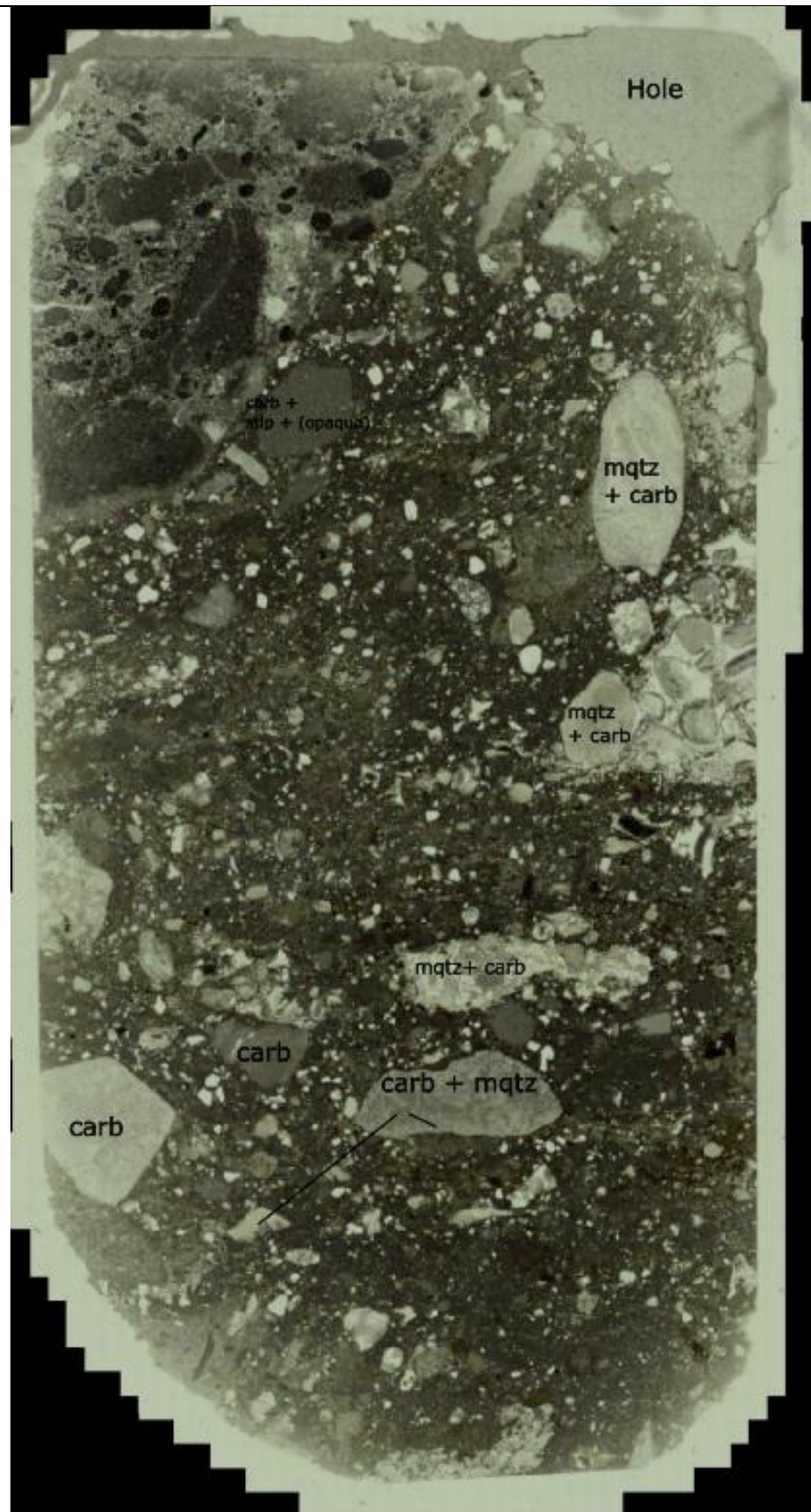
HEX - TS18

Scan size is approximately 2x4 cm

HEX - TS19
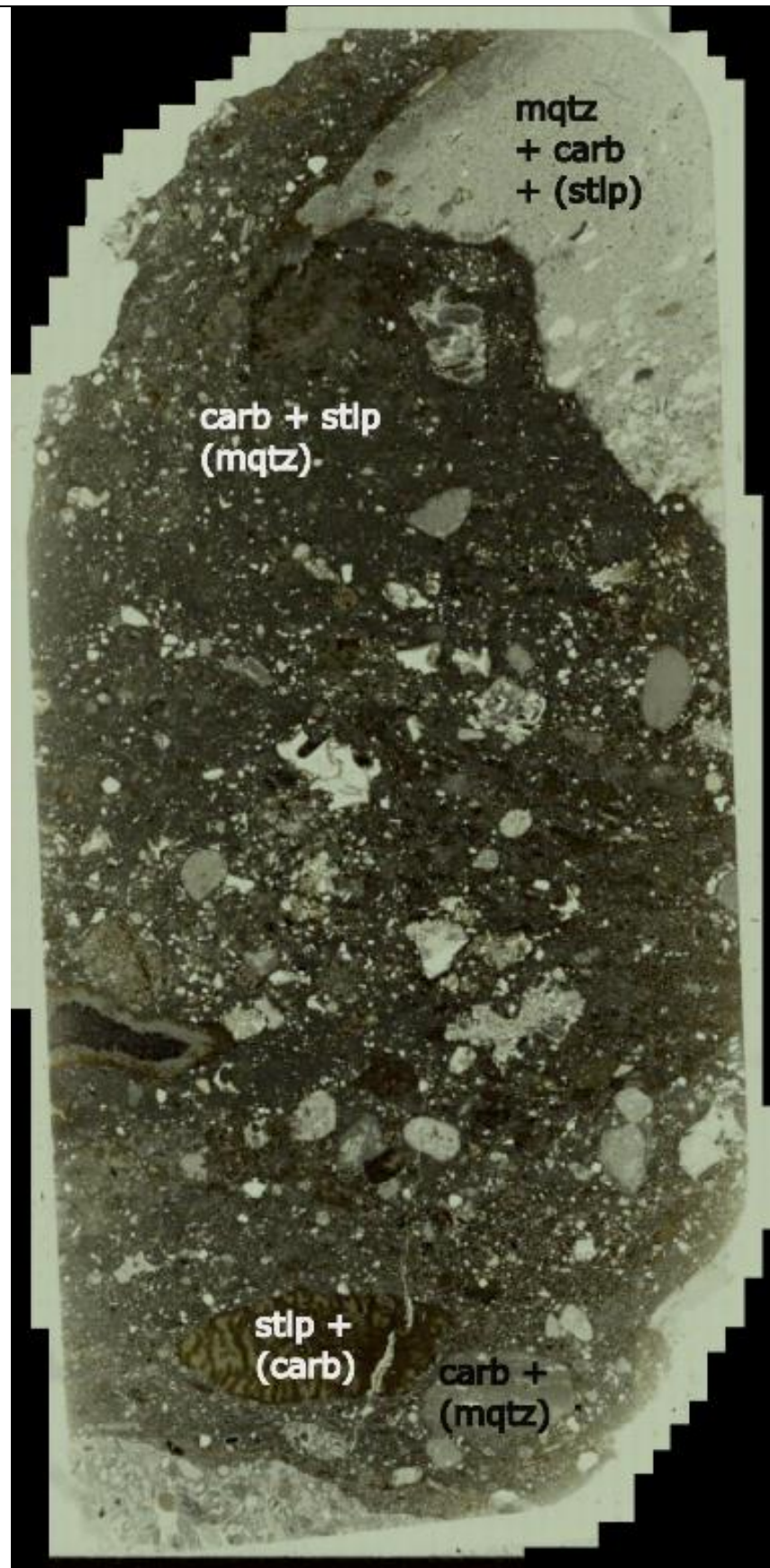
Scan size is approximately 2x4 cm

HEX - TS20

Scan size is approximately 2x4 cm
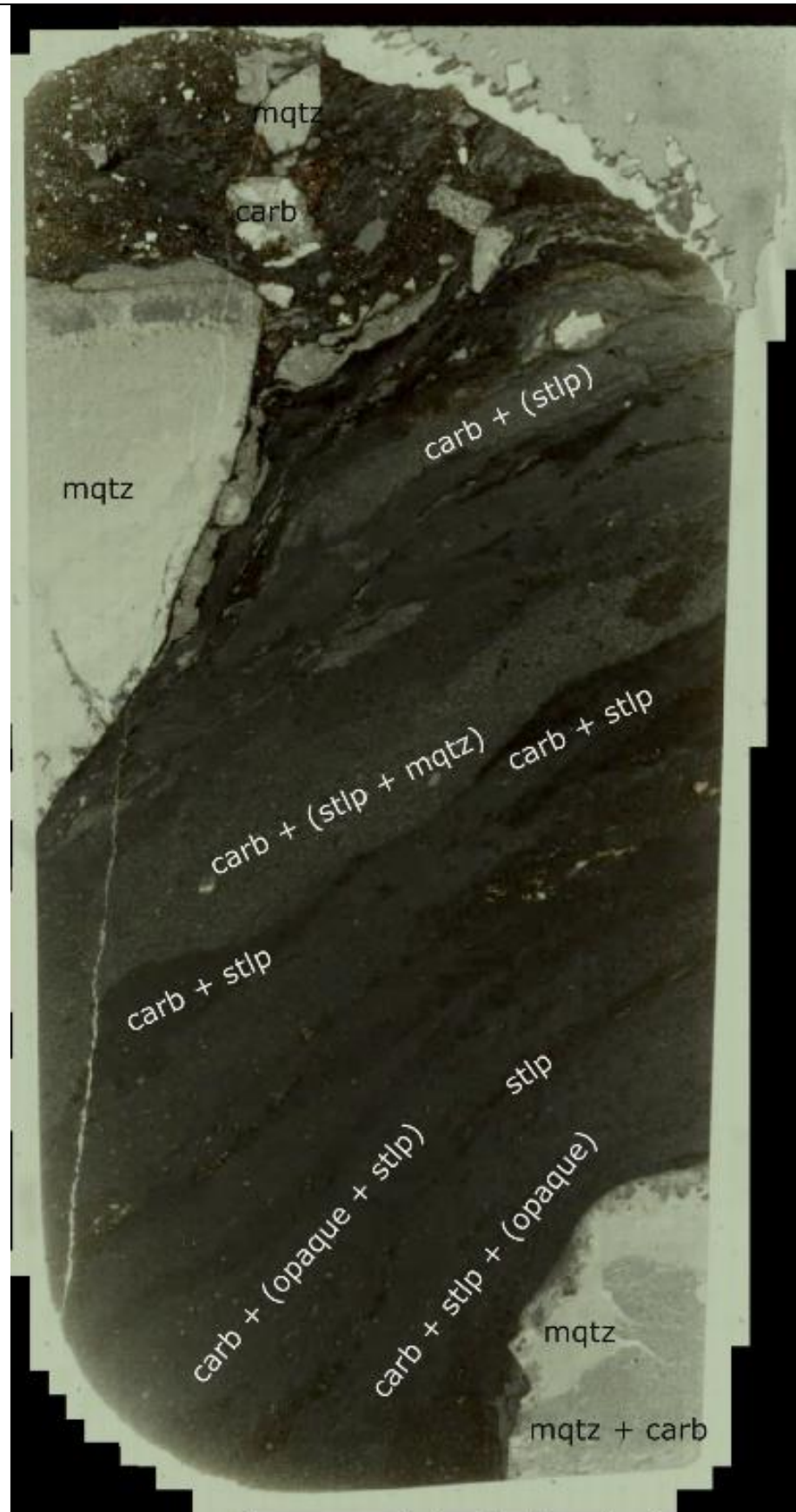
HEX - TS21

Scan size is approximately 2x4 cm
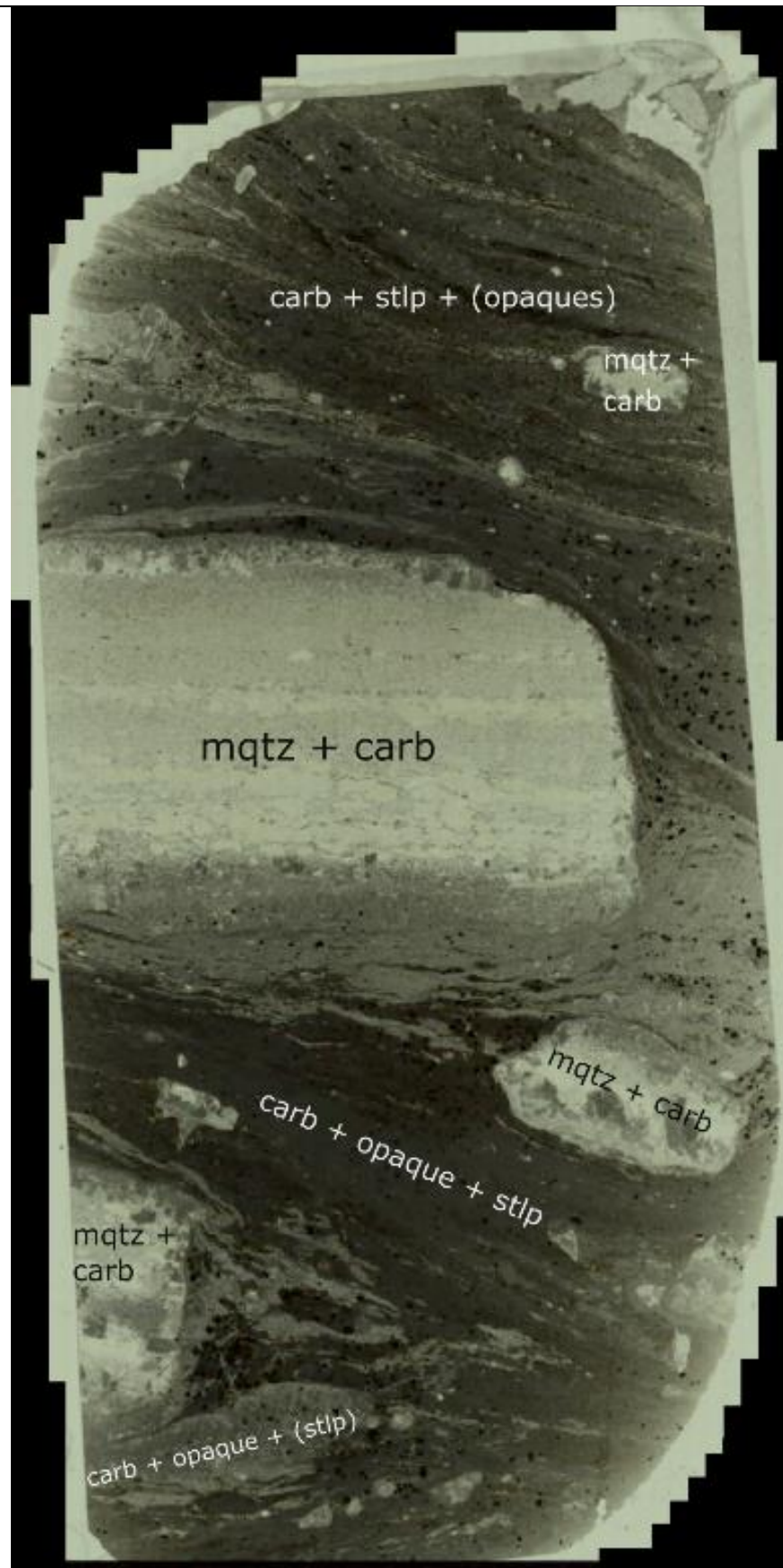
HEX - TS22

Scan size is approximately 2x4 cm

HEX - TS23
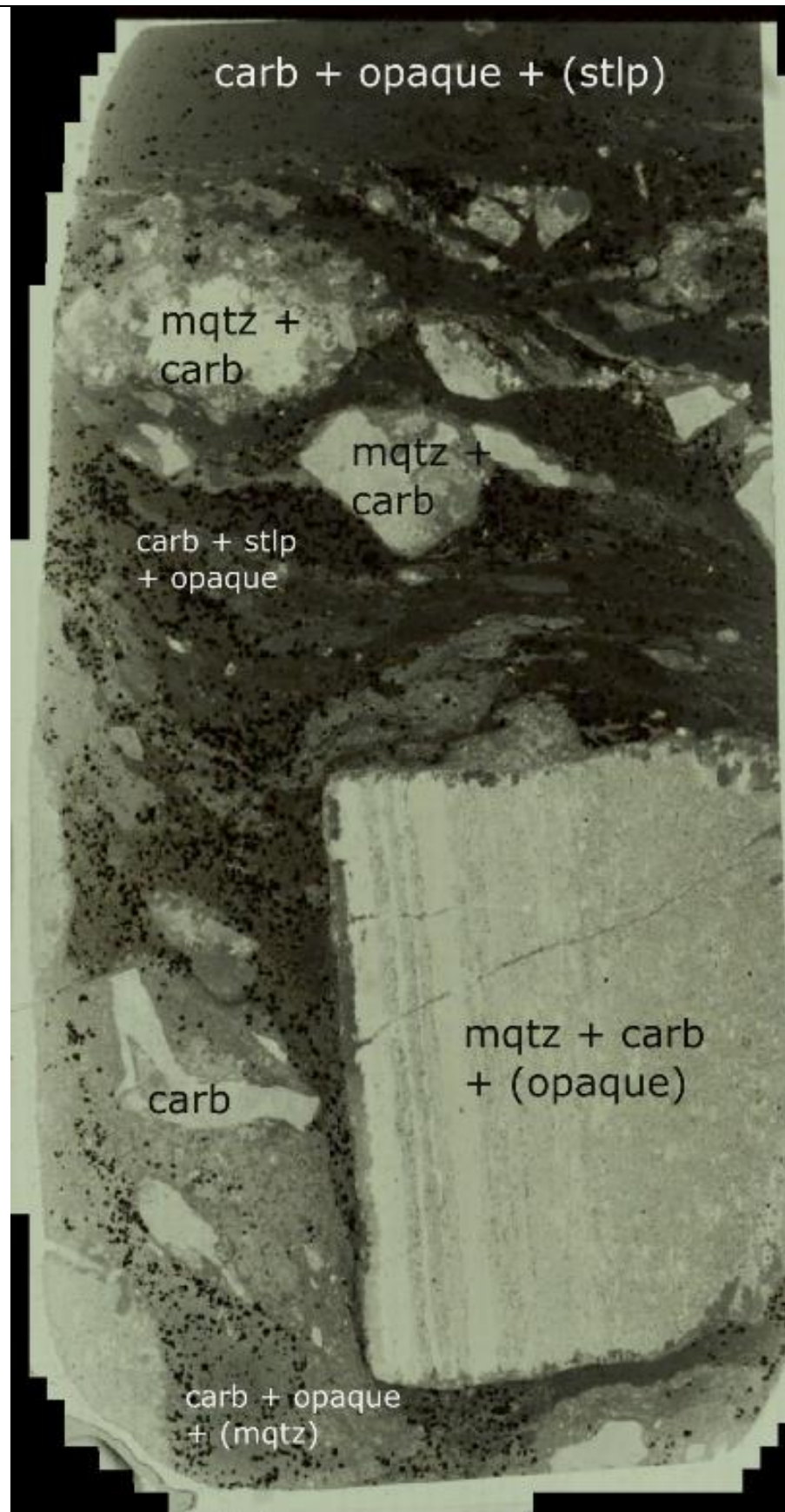
Scan size is approximately 2x4 cm
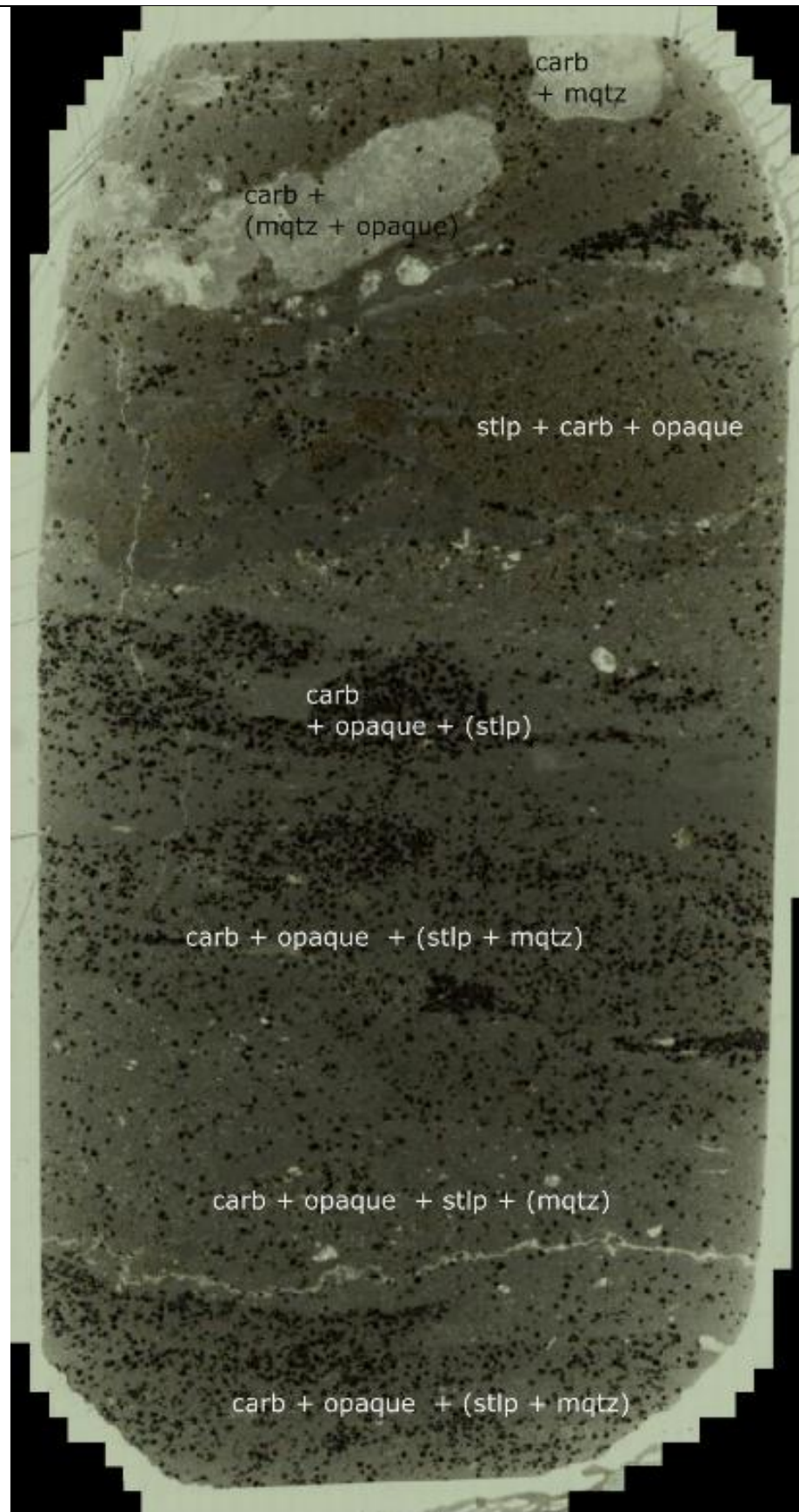
HEX - TS24

Scan size is approximately 2x4 cm

HEX - TS25
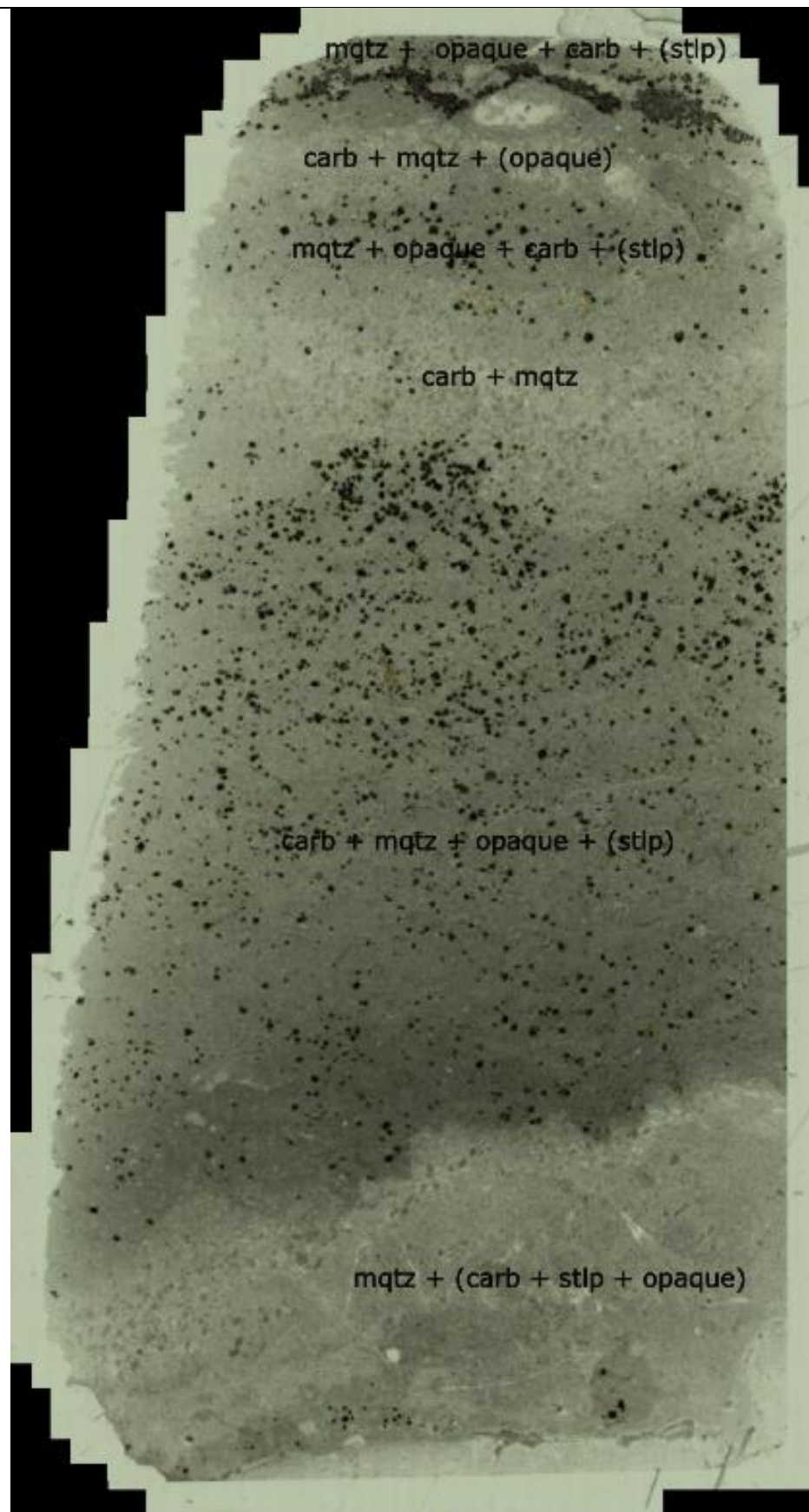
Scan size is approximately 2x4 cm

8.4 Appendix IV - EDS data

8.4.1 EDS data AARPAN core

Thin section	analysis number	mineral	point	CaO	O	Na2O	MgO	Al2O3	SiO2	K2O	SO3	MnO	FeO
1	27	calcite	1	96.15	0		0.38					nd	3.47
1	27	calcite	2	96.35	0		0.1					0.66	2.88
1	27	calcite	3	97.2	0		nd					1.15	1.65
1	27	calcite	4	94.28	0		0.47					3.39	1.85
1	27	calcite	5	87.62	0		1.21					2.91	8.26
1	28	ankerite	1	44.53	0		7.52					9.39	38.56
1	28	ankerite	2	48.43	0		9.82					9.76	31.99
1	28	ankerite	3	45.19	0		9.04					15.82	29.96
1	28	ankerite	4	48.66	0		9.47					10.4	31.47
1	28	ankerite	5	44.46	0		6.99					12.59	35.96
1	28	ankerite	6	52.69	0		8.09					7.54	31.68
2	26	calcite	1	92.93	0		0.96					3.47	2.64
2	26	calcite	2	92.37	0		nd					3.22	4.4
2	26	calcite	3	92.46	0		1.75					2.46	3.33
2	26	calcite	4	97.78	0		0.34		0.09			1.79	
2	26	calcite	5	95.28	0		nd					3.35	1.37
2	26	calcite	6	92.22	0		nd					4.6	3.18
2	27	calcite	1	92.03	0		0.05					0.73	7.18
2	27	siderite	2	1.89	0		8.31					13.59	76.21
2	27	siderite	3	1.75	0		5.39					19.18	73.68
2	27	calcite	4	94.46	0		1.61					2.65	1.28
2	27	siderite	5	3.36	0		5.55					13.51	77.58
2	27	calcite	6	96.13	0		nd					0.43	3.44
2	28	siderite	1	3.18	0		4.31					9.92	82.59
2	28	siderite	2	1.42	0		6.41					10.7	81.47
2	28	siderite	3	2.09	0		8.66					9.37	79.89
2	28	siderite	4	0.89	0		8.09					18.75	72.27
2	28	siderite	5	0.44	0		6.85					16.13	76.58
2	28	siderite	6	0.28	0		7.48					11.12	81.12
3	17	ankerite	1	47.84	0		10.3		4.93			6.7	30.23
3	17	ankerite	2	48.5	0		6.7					13.02	31.78
3	17	ankerite	3	47.29	0		10.02					10.13	32.57
3	17	ankerite	4	46.38	0		6.78					11.9	34.94
3	17	ankerite	5	46.39	0		7.25					10.35	36.01
3	17	stilpnomelane	6	nd	0	0.34	2.09	5	53.71	1.19		nd	37.67
3	18	stilpnomelane	1	nd	0	1.73	3.7	2.41	51.43	2.88		1.51	36.34
3	18	ankerite	2	45.85	0		9.27					11.7	33.18
3	18	ankerite	3	54.42	0		16.81					16.22	12.56
3	18	ankerite	4	52.33	0		21.12					8.26	18.29
3	18	ankerite	5	45.42	0		10.48					9.61	34.49
3	18	ankerite	6	43.46	0		8.62		2.65			8.71	36.56

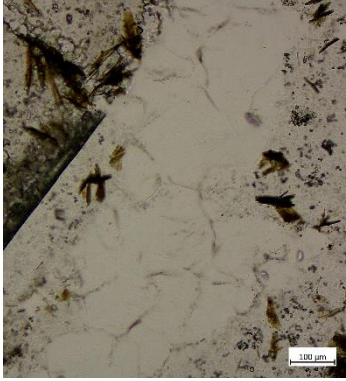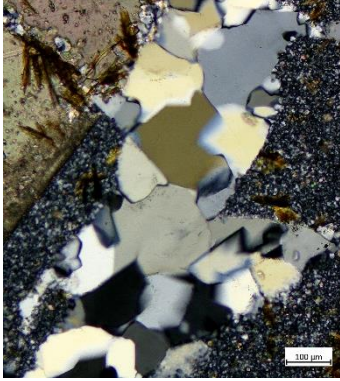|													
3	19	ankerite	1	43.43	0		7.34					13.67	35.55
3	19	ankerite	2	51.63	0		7.11					9.86	31.4
3	19	ankerite	3	50.13	0		7.28					8.49	34.09
3	19	ankerite	4	52	0		7.17					8.49	32.34
3	19	ankerite	5	49.45	0		6.53					11.17	32.85
3	19	ankerite	6	49.28	0		6.75					9.55	34.41
4	23	ankerite	1	55.45	0		8.69					7.55	28.31
4	23	ankerite	2	50.99	0		17.38					5.6	26.03
4	23	ankerite	3	48.92	0		7.33					11.92	31.83
4	23	ankerite	4	49.85	0		8.03					8.16	33.96
4	23	ankerite	5	42.36	0		19.63					18.01	20
4	23	ankerite	6	46.32	0		9.9					8.69	35.1
4	24	stilpnomelane	1	nd	0	nd	2.94	4.86	47.41	1.99		0.28	42.51
4	24	ankerite	2	40.06	0		19.27					17.61	23.06
4	24	ankerite	3	46.39	0		6.29					14.15	33.17
4	24	ankerite	4	48.64	0		7.1					9.58	34.69
4	24	ankerite	5	52.41	0		21.84					16.18	9.57
4	24	ankerite	6	41.23	0		6.51					7.51	44.74
4	25	ankerite	1	46.45	0		8.36					13.55	31.64
4	25	ankerite	2	49	0		8.23					12.14	30.62
4	25	HMC	3	58.16	0		38.77					0.17	2.9
4	25	ankerite	4	49.37	0		6.48					11.53	32.62
4	25	ankerite	5	51.18	0		5.7					7.45	35.67
4	25	ankerite	6	48.32	0		17.22					16.31	18.16
4	26	HMC	1	51.34	0		27.15					10.5	11.01
5	20	ankerite	1	51.57	0		7.02					6.91	34.5
5	20	ankerite	2	44.56	0		5.85					13.78	35.81
5	20	ankerite	3	45.58	0		21.05					21.92	11.45
5	20	ankerite	4	47	0		19.09					11.76	22.15
5	20	ankerite	5	45.98	0		7.98					11.9	34.15
5	20	ankerite	6	45.71	0		11.92					11.06	31.32
5	21	ankerite	1	45.27	0		9.1					11.15	34.48
5	21	ankerite	2	49.03	0		10.06					9.29	31.63
5	21	ankerite	3	55.06	0		7.63					9.47	27.84
5	21	ankerite	4	45.45	0		10.18					10.02	34.35
5	21	ankerite	5	48.33	0		5.05					10.59	36.03
5	21	ankerite	6	45.26	0		16.68					12.33	25.73
5	22	ankerite	1	50.27	0		10.71					12.68	26.34
5	22	ankerite	2	44.68	0		6.52					12.91	35.9
5	22	ankerite	3	46.83	0		9.25					11.45	32.48
5	22	ankerite	4	50.25	0		8.5					10.39	30.87
5	22	ankerite	5	50.09	0		6.46					13.46	29.99
5	22	ankerite	6	49.8	0		7.07					11.29	31.84

Onset of the Makganyene Glaciation

8.4.2 EDS data ERIN core

Thin section	Analysis number	mineral	point	CaO	O	Na2O	MgO	Al2O3	SiO2	K2O	SO3	MnO	FeO	TiO2
6	29	calcite	1	94.69	0		nd					3.21	2.09	
6	29	HMC	2	62.2	0		37.37					nd	0.44	
6	29	HMC	3	53.44	0		29.09					7.71	9.76	
6	29	stilpnomelane	4	nd	0	1.43	4.06	4.89	51.67	2.47		nd	35.47	
6	29	stilpnomelane	5	nd	0	1.33	3.78	3.54	48.25	2.02		2.62	38.46	
6	29	stilpnomelane	6	0.46	0	1.6	3.48		54.14	3.43		nd	36.89	
6	30	calcite	1	90.62	0		1.39					nd	8	
6	30	HMC	2	59.97	0		39.59					nd	0.44	
6	30	HMC	3	56.52	0		22.71					3.98	16.78	
6	30	HMC	4	58.18	0		33.49					0.84	7.5	
6	30	ankerite	5	50.9	0		28.58					8.95	11.56	
6	30	stilpnomelane	6	0.18	0	1.06	4.44	6.84	48.62	2.6		1.53	34.73	
6	31	HMC	1	60.31	0		29.72					0.93	9.04	
6	31	HMC	2	58.39	0		29.95					0.35	11.31	
6	31	HMC	3	52.79	0		22.75					4.18	20.29	
6	31		4	66.25	0		0.3		25.1			4.36	3.98	
6	31	stilpnomelane	5	nd	0	1.87	3.43	4.73	48.84	3.41		0.24	37.47	
6	31	stilpnomelane	6	nd	0	0.2	6.17	5.87	45.63	0.91		1.13	40.08	
6	32	calcite	1	96.24	0		0.4					1.3	2.05	
6	32	HMC	2	58.96	0		36.81					2.84	1.39	
6	32	ankerite	3	50.08	0		22.49					2.97	24.46	
6	32	HMC	4	56.14	0		31.91					3.65	8.3	
6	32	HMC	5	56.06	0		28.92					5	10.02	
6	32	calcite	6	87.08	0		0.97					4.12	7.82	
7	33	calcite	1	95.64	0		0.64					0.53	3.2	
7	33	calcite	2	87.92	0		1.45					5.78	4.85	
7	33	siderite	3	0.64	0		8.8					7.78	82.79	
7	33	siderite	4	3.78	0		7.44					4.3	84.47	
7	33	calcite	5	88.54	0		0.44					2.83	8.19	
7	33	siderite	6	2.93	0		6.61					8.14	82.32	
7	34	siderite	1	nd	0		6.89					9.31	83.8	
7	34	calcite	2	89.6	0		nd					3.51	6.89	
7	34	ankerite	3	46.98	0		20.86					6.98	25.18	
7	34	ankerite	4	54.94	0		7.94					7.73	29.39	
7	34	HMC	5	54.26	0		34.62					1.98	9.15	
7	34	HMC	6	59.95	0		33.39					3.17	3.49	
7	35	HMC	1	58.26	0		39.27					2	0.46	
7	35	HMC	2	58.65	0		33.85					0.74	6.75	
7	35	ankerite	3	49.42	0		23.17					6.24	21.17	
7	35	siderite	4	0.64	0		nd					nd	99.36	
7	35	calcite	5	87.86	0		1.17					2.87	8.1	
7	35	calcite	6	87.35	0		3.07					3.6	5.98	
7	36	quartz	1		0				100					

Thin section	analysis number	mineral	point	CaO	O	Na2O	MgO	Al2O3	SiO2	K2O	SO3	MnO	FeO	Cu	V2O5
7	36	HMC	2	60.29	0		39.71						nd		
7	36	HMC	3	58.75	0		31.96						9.29		
7	36	HMC	4	51.2	0		30.62					5.7	12.47		
7	36	stilpnomelane	5	0.75	0	1.05	2	7.37	51.24	1.57			36.02		
7	36	stilpnomelane	6	0.84	0	1.12	4.57	3.9	50.88	2.03		0.84	35.82		
8	1	stilpnomelane	1		0		5.39	6.82	38.44				49.35		
8	1	calcite	2	92.74	0				6.5			0.75			
8	1	calcite	3	90.68	0			1.09	3.32			2.23	2.68		
8	1	quartz	4		0				100						
8	2	calcite	1	81.76	0				2.2			4.04	12		
8	2	calcite	2	85.27	0		2.08		3.25			nd	9.41		
8	2	calcite	3	84.75	0				6.08			0.58	8.59		
8	3	calcite	1	96.28	0		3.72								
8	3		2	58.93	0		41.07								
8	3	ankerite	3	69.18	0		6.41						24.41		
8	3	calcite	4	96.46	0		3.54								
8	3	ankerite	5	66.84	0								30.97	2.19	
11	4	calcite	1	90.14	0			2.07	7.79						
11	4	stilpnomelane	2		0	1.3	3.77	4.24	50.08	3.35			37.25		
11	4	calcite	3	91.36	0				8.64						
11	4	quartz	4		0				100						
11	4	quartz	5		0				100						

8.4.3 EDS data LONDON core

Thin section	analysis number	mineral	point	CaO	O	Na2O	MgO	Al2O3	SiO2	K2O	SO3	MnO	FeO	Cu	V2O5
12	1	ankerite	1	45.78	0		12.84					4.3	37.07		
12	1	ankerite	2	54.79	0		10.35					2.72	32.15		
12	1	ankerite	3	51.98	0		11.48					4.52	32.02		
12	1	magnetite	4		0							0.8	99.2		
12	1	magnetite	5		0				2.68			nd	97.32		
12	1	quartz	6		0				100			nd			
12	2	ankerite	1	54.94	0		8.77					3.9	32.39		
12	2	ankerite	2	51.13	0		11.04					4.92	32.91		
12	2	ankerite	3	52.83	0		10.33					7.11	29.73		
12	2	siderite	4		0		8.54					5.65	85.81		
12	2	siderite	5	3.52	0		8.14					6.89	81.45		
12	2	stilpnomelane	6		0		4	5.56	50.06	2.44		0.65	37.29		
12	3	ankerite	1	58.86	0		9.3	0.9				1.66	29.28		
12	3	ankerite	2	57.54	0		25.29					nd	17.17		
12	3	ankerite	3	52.53	0		6.49					2.04	38.95		
12	3	ankerite	4	50.56	0		9.33					2.15	37.96		
12	3	ankerite	5	46.58	0		10.68					2.04	40.71		
13	4	ankerite	1	49.39	0		9.76		0.43			6.71	33.71		
13	4	ankerite	2	51.38	0		8.44					5.1	35.08		

13	4	ankerite	3	66.36	0		32.92					nd	0.72		
13	4	ankerite	4	51.12	0		26.29			1.65		6.79	12.86		1.29
13	4	ankerite	5	50.06	0		8.47					3.18	38.29		
13	4	ankerite	6	48.35	0		8.2					4.9	38.54		
13	5	ankerite	1	47.78	0		11.05					4.6	36.58		
13	5	ankerite	2	52.53	0		10.46					7.07	29.94		
13	5	siderite	3	1.73	0		11.4					5.39	81.48		
13	5	stilpnomelane	4		0	1.25	2.8	5.86	47.15	2.81		0.25	39.87		
13	5	siderite	5		0		11.26					4.71	84.02		
13	5	ankerite	6	50.62	0		11.45					3.62	34.31		
14	6	ankerite	1	51.03	0		10.38	nd				3.65	34.94		
14	6	ankerite	2	52.48	0		10.77					3.81	32.94		
14	6	ankerite	3	54.69	0		26.85			1.94		1.54	14.98		
14	6	ankerite	4	50.96	0		13.76					4.42	30.85		
14	6	stilpnomelane	5		0		4.04	4.23	50.77	2.6		nd	38.36		
14	6	stilpnomelane	6		0		3.62	5.1	53.4	0.25		0.47	37.16		
14	7	ankerite	1	50.17	0		12.05					8.47	29.31		
14	7	ankerite	2	51	0		9.11					2.45	37.43		
14	7	ankerite	3	49.71	0		9.83					0.13	40.33		
14	7	ankerite	4	53.65	0		8.86					6.77	30.72		
14	7	ankerite	5	48.41	0		11.55					5.83	34.22		
14	7	ankerite	6	50.68	0		26.93			2.34		6.7	13.35		
15	1	chalcopyrite	1		0						32.88		28.96	38.17	
15	1	chalcopyrite	2		0						36.19		30.44	33.36	
15	1	magnetite	3		0								100		
15	2	ankerite	1	49.56	0		9.55					7.42	33.47		
15	2	ankerite	2	49.21	0		10.12					5.88	34.78		
15	2	ankerite	3	48.21	0		9.88					7.67	34.24		
15	3	ankerite	2	48.25	0		7.3					9.91	34.54		
15	3	ankerite	3	48.92	0		10.93					7.87	32.28		
15	3	ankerite	4	52.63	0		8.92					4.86	33.6		
15	3	ankerite	5	49.89	0		6.96					5.71	37.44		
15	3	magnetite	6		0								100		
16	8	ankerite	1	49.39	0		12.33					5.9	32.38		
16	8	ankerite	2	51.3	0		11.13			2.93		8.95	25.7		
16	8	ankerite	3	50.22	0		12.71					2.25	34.82		
16	8	ankerite	4	50.18	0		12.74					3.84	33.24		
16	8	ankerite	5	56.08	0		24.77					6.86	12.28		
16	8	ankerite	6	50.63	0		28.36					6.26	14.75		
16	9	magnetite	1		0								100		
16	9	magnetite	2		0								100		
16	9	ankerite	3	48.94	0		10.69					3.08	37.29		
16	10	ankerite	1	48.94	0		11.57					6.93	32.56		
16	10	ankerite	2	48.67	0		10.2					6.64	34.49		
16	10	ankerite	3	41.72	0		13.03					4.99	40.25		
16	10	stilpnomelane	4		0	0.86	4.46	5.7	50.56	1.78			36.64		

16	10	stilpnomelane	5		0	3.03	5.32		49.24	1.44			40.98		
16	10	magnetite	6		0								100		
17	11	ankerite	1	53.3	0		12.41					2.73	31.56		
17	11	ankerite	2	51.73	0		11.84					1.08	35.35		
17	11	ankerite	3	47.86	0		10.52					4.76	36.87		
17	11	ankerite	4	48.06	0		10.15					7.89	33.91		
17	11	ankerite	5	54.89	0		13.59					3.1	28.42		
17	11	ankerite	6	45.22	0		12.54					6.99	35.24		
17	12	HMC	1	61.17	0		27.94					1.55	9.34		
17	12	ankerite	2	49.44	0		11.17					8.97	30.42		
17	12	ankerite	3	46.8	0		9.38	1.65				2.58	39.58		
17	12	ankerite	4	53.29	0		13.4					4.5	28.81		
17	12	ankerite	5	53.56	0		9.49					2.6	34.35		
17	12	ankerite	6	53.12	0		8					6.67	32.21		
17	13	ankerite	1	48.41	0		10.06					5.9	35.63		
17	13	ankerite	2	51.69	0		10.79					6	31.52		
17	13	ankerite	3	50.59	0		9.43					1.7	38.29		
17	13	ankerite	4	50.84	0		11.28					4.47	33.41		
17	13	ankerite	5	48.45	0		9.74					4.27	37.53		
17	13	ankerite	6	48.32	0		9.66					3.11	38.91		
17	14	stilpnomelane	1	0.55	0	0.21	6.15	4.33	52.07	2.68			34		
17	14	stilpnomelane	2	0.39	0	nd	3.06	2.93	52.18	1.97			39.46		
17	14	magnetite	3		0								100		
17	14	magnetite	4		0								100		
17	14	stilpnomelane	5	16.94	0	nd	5.98	3.68	32.95	0.95			39.49		
17	14	stilpnomelane	6	0.1	0	0.23	3.08	3.55	54.55	1.81			36.67		
17	15	ankerite	1	46.41	0		9.45					6.22	37.92		
17	15	ankerite	2	51.22	0		9.51					3.17	36.1		
17	15	ankerite	3	49.36	0		9.7					6.48	34.46		
17	15	ankerite	4	50.03	0		11.27					6.64	32.06		
17	15	ankerite	5	49.59	0		10.77					3.73	35.91		
17	15	ankerite	6	50	0		10.76					3.07	36.18		
17	16	ankerite	1	50.16	0		9.09					6.33	34.42		
17	16	ankerite	2	53.6	0		12.8					5.9	27.7		
17	16	ankerite	3	49.12	0		10.95					3.25	36.68		
17	16	ankerite	4	55.19	0		8.77					4.15	31.89		
17	16	ankerite	5	50.12	0		10.79					4.07	35.03		
17	16	ankerite	6	47.11	0		8.7					8.28	35.9		

8.4.4 EDS data HEX core

Thin section	analysis number	mineral	point	CaO	O	Na2O	MgO	Al2O3	SiO2	K2O	SO3	MnO	FeO
18	1	siderite	1	0.83	0		9.89					7.83	81.44
18	1	siderite	2	0.18	0		12.83					3.94	83.05
18	1	siderite	3	2.52	0		8.77					4.61	84.11
18	1	siderite	4	nd	0		6.55					9.09	84.36
18	1	siderite	5	0.63	0		12.11					4.45	82.81
18	1	ankerite	6	50.51	0		8.24					4.14	37.1
18	2	ankerite	1	56.91	0		9.31					0.22	33.56
18	2	HMC	2	59.39	0		23.42					4.52	12.67
18	2	HMC	3	56.49	0		24.75					5.84	12.92
18	2	ankerite	4	46.63	0		9.88					3.1	40.39
18	2	siderite	5	2.13	0		8.97					3.93	84.97
18	2	siderite	6	1.35	0		9.69					1.28	87.68
18	3	ankerite	1	51.44	0		12.23					1.47	34.86
18	3	ankerite	2	47.4	0		10.11					3.46	39.03
18	3	ankerite	3	49.52	0		7.74					2.31	40.43
18	3	ankerite	4	51.61	0		6.86					4.2	37.33
18	3	HMC	5	56.18	0		26.16					5.44	12.22
18	3	HMC	6	61.03	0		23.4					2.11	13.45
18	4	calcite	1	89.92	0		0.68					3.55	5.85
18	4	quartz	2		0				100				
18	4	quartz	3		0				100				
18	4	calcite	4	89.2	0		1.24					1.96	7.6
18	4	ankerite	5	58.73	0		8.26					5.27	27.74
18	4	calcite	6	88.44	0		0.69					4.58	6.29
18	5	siderite	1	1.68	0		6.87					1.8	89.64
18	5	siderite	2	nd	0		7.8					3.69	88.51
18	5	siderite	3	1.15	0		6.5		2.42			5.89	84.04
18	5	stilpnomelane	4	nd	0	0.51	3.25	6.32	50.08	3.48		1.37	35
18	5	stilpnomelane	5	nd	0	nd	5.3	4.57	49.32	2.18		nd	38.63
18	5	stilpnomelane	6	1.34	0	nd	4.88	5.79	43.24	1.1		1.21	42.44
19	6	ankerite	1	51.99	0	11.39						7.83	28.8
19	6	ankerite	2	55.58	0	26.1						3.65	14.68
19	6	siderite	3	2.27	0	9.29			9.66			6.98	71.79
19	6	siderite	4		0	8.52						1.35	90.12
19	6	siderite	5	1.99	0	7.92						2.73	87.35
19	6	ankerite	6	51.88	0	11.29						6.56	30.27
19	7	pyrite	1								69.04		30.96
19	7	HMC	2	57.04	0		28.08					0.57	14.32
19	7	ankerite	3	47.1	0		10.31					7.9	34.69
19	7	siderite	4	0.78	0		9.08					8.1	82.04
19	7	siderite	5	1.27	0		8.01					6.14	84.58
19	7	siderite	6	0.51	0		7.3					8.32	83.87
19	8	HMC	1	59.62	0		27.13					1.01	12.23

19	8	ankerite	2	45.48	0		13.63					3.7	37.19
19	8	ankerite	3	58.23	0		21.53					2.12	18.12
19	8	HMC	4	65.02	0		31.76					0.24	2.98
19	8	ankerite	5	28.5	0		10.83					3.32	57.36
19	8	ankerite	6	52.95	0		9.96					3.52	33.57
19	9	HMC	1	54.65	0		27.76					4.7	12.89
19	9	ankerite	2	51.95	0		11.73					1.1	35.22
19	9	ankerite	3	48.5	0		12.01					4.97	34.52
19	9	HMC	4	56.14	0		26.93					4.07	12.87
19	9	ankerite	5	44.08	0		12.61					2.64	40.67
19	9	siderite	6	0.43	0		7.74					6.7	85.12
19	10	siderite	1	0.83	0		10.03					nd	89.14
19	10	siderite	2	0.97	0		10.21					4.37	84.46
19	10	siderite	3	0.96	0		8.86					8.07	82.11
19	10	stilpnomelane	4	nd	0	1.3	2.59	6.46	48.34	2.61		nd	38.7
19	10	stilpnomelane	5	0.42	0	0.57	3.61	5	49.44	2.91		1.06	37
20	11	HMC	1	52.37	0		26.54					3.65	17.45
20	11	siderite	2	50.8	0		12.55					nd	36.66
20	11	ankerite	3	50.99	0		10.87					4.97	33.17
20	11	ankerite	4	50.43	0		11.04					3.4	35.14
20	11	stilpnomelane	5	nd	0	nd	2.8	7.13	50.61	1.96			37.5
20	11	stilpnomelane	6	nd	0	nd	2.88	4.63	51.75	1.54		nd	39.2
20	12	ankerite	1	55.66	0		29.06					1.17	14.12
20	12	ankerite	2	50.39	0		12.22					2.91	34.48
20	12	HMC	3	60.26	0		34.09					1.41	4.25
20	12	ankerite	4	54.1	0		10.87					2.18	32.84
20	12	ankerite	5	51.83	0		12.41					4.78	30.98
20	12	ankerite	6	52.91	0		10.35					0.44	36.3
20	13	ankerite	1	53.08	0		9.66					3.39	33.87
20	13	ankerite	2	47.93	0		11.73					5.85	34.49
20	13	pyrite	3								67.08		32.92
20	13	ankerite	4	52.91	0		10.54					6.28	30.28
20	13	ankerite	5	47.35	0		11.9					2.43	38.32
20	13	ankerite	6	47.63	0		12.49					8.21	31.67
21	23	siderite	1	2.19	0		11.41					4.38	82.02
21	23	siderite	2	2.07	0		8.48					4.03	85.41
21	23	siderite	3	0.48	0		8.9					3.28	87.34
21	23	siderite	4	2.45	0		7.87					4.99	84.69
21	23	sstil	5	0.46	0	nd	2.9	5.02	53.22	1.84		1.09	35.47
21	23	stilpnomelane	6	0.3	0	0.87	3.45	6.1	48.59	1.68		0.05	38.96
21	24	ankerite	1	48.85	0		12.69					6.53	31.93
21	24	siderite	2	0.57	0		10.54					5.03	83.86
21	24	siderite	3	0.13	0		9.57					6.02	84.27
21	24	siderite	4	0.54	0		10.84					4.3	84.32
21	24	stilpnomelane	5	nd	0	0.34	3.67	6.52	50.34	1.24		0.85	37.04
21	24	siderite	6	1.26	0		10.94					4.15	83.65

21	25	calcite	1	91.73	0		1.33					2.4	4.54
21	25	siderite	2	0.98	0		8.83					6.72	83.48
21	25	ankerite	3	47.91	0		11.58					4.07	36.45
21	25	siderite	4	1.06	0		11.69					1.69	85.55
21	25	ankerite	5	52.28	0		18.17					3.77	25.78
21	25	stilpnomelane	6	1.32	0	0.95	3.17	3.2	50.39	2.73		nd	38.25
23	19	ankerite	1	51.07	0		12.05					4.41	32.47
23	19	ankerite	2	48.26	0		13.07					1.46	37.22
23	19	ankerite	3	51.99	0		10.55					3.61	33.85
23	19	ankerite	4	46.89	0		10.51					4.31	38.29
23	19	magnetite	5		0								100
23	20	ankerite	1	52.98	0		8.06					3.62	35.33
23	20	calcite	2	95.64	0		0.13					4.23	nd
23	20	ankerite	3	50.52	0		9.4					1.94	38.14
23	20	ankerite	4	48.18	0		11.96					2.49	37.37
23	20	ankerite	5	52.45	0		8.84					2.49	36.22
23	20	siderite	6	0.38	0		7.22					2.3	90.09
23	21	ankerite	1	46.7	0		9.08					4.15	40.07
23	21	siderite	2	0.29	0		6.28		6.38			8.37	78.68
23	21	ankerite	3	60.3	0		4.71					3.23	31.75
23	21	siderite	4	2.36	0		6.62					6.45	84.57
23	21	siderite	5	nd	0		9.9		16.08			4.96	69.07
23	21	HMC	6	58.46	0		34.85					nd	6.69
23	22	siderite	1	1.13	0		11.25					3.85	83.76
23	22	siderite	2	0.67	0		10.42					8.16	80.74
23	22	siderite	3	nd	0		10.75					5.05	84.21
23	22	siderite	4	1.25	0		6.07					4.81	87.88
23	22	siderite	5	0.71	0		10.69					5.17	83.44
23	22	calcite	6	95.28	0		0.92					0.41	3.39
25	14	ankerite	1	53.55	0		11					2.21	33.25
25	14	ankerite	2	56.26	0		7.56					2.47	33.71
25	14	ankerite	3	50.09	0		10.17					3.4	36.35
25	14	ankerite	4	51.35	0		9.15					2.11	37.4
25	14	siderite	5	1.75	0		11.94					4.58	81.73
25	14	ankerite	6	52.29	0		13.71					3.17	30.84
25	15	ankerite	1	45.68	0		11.48					5.3	37.53
25	15	ankerite	2	48.39	0		10.2					7.57	33.84
25	15	ankerite	3	44.03	0		10.95					6.39	38.64
25	15	ankerite	4	49.04	0		13.09					6.78	31.09
25	15	ankerite	5	49.65	0		10.99					1.01	38.36
25	15	ankerite	6	38.55	0		8.79					3.03	49.63
25	16	ankerite	1	51.98	0		7.65					2.74	37.63
25	16	siderite	2	1.5	0		10.46					6.6	81.44
25	16	ankerite	3	49.48	0		8.99					3.28	38.25
25	16	siderite	4	12.63	0		12.96					3.74	70.67
25	16	ankerite	5	55.5	0		7.76					5.36	31.38

25	16	ankerite	6	76.58	0		3.07					2.95	17.4
25	17	ankerite	1	33.49	0		6.71		38.19			2.27	19.33
25	17	ankerite	2	55.2	0		3.93					2.81	38.05
25	17	ankerite	3	48.3	0		11.44					1.5	38.76
25	17	ankerite	4	52.04	0		5.11					0.77	42.08
25	17	ankerite	5	48.94	0		12.03					1.29	37.74
25	17	ankerite	6	49.68	0		9.78					7.02	33.52
25	18	calcite	1	95.87	0		1.27					nd	2.86
25	18	ankerite	2	55.39	0		7.74					5.76	31.11
25	18	ankerite	3	49.04	0		9.27					1.19	40.49
25	18	ankerite	4	48.81	0		8.93					1.92	40.34
25	18	ankerite	5	50.57	0		9.08					2.64	37.72
25	18	ankerite	6	49.07	0		9.94					1.28	39.71

8.5 Appendix V - LA-ICP-MS Data

Type	Carb/Stilp	Carb/Stilp	Stilp/Carb	Stilp/Carb	Stilp/Carb	Chert	Chert	Carb/Stilp
#scans	15	12	13	11	11	9	11	12
	clast	clast	clast	clast	clast	clast	clast	clast
	TS12-A-5	TS12-B-6	TS12-C-7	TS12-E-8	TS12-F-9	TS12-H-14	TS12-I-15	TS6-A1-33
Na	325	880	4135	1124	664	306	311	389
Mg	10512	13722	14055	41902	60429	1452	637	102587
Al	1904	3063	16606	5771	3354	154	330	841
Ca	36983	20795	2830	8401	38774	5176	1152	192968
Sc	1.083	4.250	4.050	5.020	5.160	6.970	7.020	1.470
Ti	5.5	16	606	12	2.2	12	37	51
V	1.9	5.0	24	6.9	3.6	0.6	1.3	3.0
Cr	1.2	5.4	16	9.0	11	3.2	73	29
Mn	4839	9226	1255	34791	48587	860	292	9752
Fe	65750	177070	214215	600965	815288	17174	11539	56442
Co	0.04	0.09		0.15	0.25	0.28	0.13	0.23
Ni	0.62	2.9	5.0	5.3	4.9	2.6	3.0	1.2
As	0.09	0.85	1.5	0.46	0.07	0.76	1.3	0.56
Rb	9.0	15	92	25	13	2.6	1.6	2.9
Sr	6.3	4.2	4.5	2.9	5.9	1.0	0.71	57
Y	3.4	2.7	1.1	4.4	7.0	0.42	0.12	5.6
Zr	0.43	1.8	7.0	1.5	17	0.26	2.7	2.6
Nb	0.20	0.28	2.8	0.32	0.11	0.05	0.28	0.08
Mo	0.07	0.21	1.8	0.15	0.09	0.02	0.28	0.05
Cs	1.5	2.7	16	5.9	2.0	0.32	0.20	0.42
Ba	1.9	6.2	24	7.2	2.5	0.95	0.44	7.4
La	0.60	0.60	0.70	1.7	1.6	0.22	0.43	4.3
Ce	1.6	1.3	1.6	2.9	2.7	0.52	0.51	7.1
Pr	0.22	0.19	0.19	0.38	0.27	0.38	0.03	0.78
Nd	0.93	0.78	0.79	1.4	1.2	0.20	0.21	2.9
Sm	0.27	0.23	0.18	0.34	0.31	0.03	0.02	0.56
Eu	0.18	0.14	0.05	0.12	0.14	0.02	0.02	0.16
Gd	0.33	0.27	0.16	0.37	0.46	0.13	0.05	0.67
Tb	0.06	0.06	0.02	0.08	0.08	0.00	0.01	0.09
Dy	0.41	0.32	0.20	0.37	0.54	0.04	0.02	0.69
Ho	0.08	0.07	0.03	0.12	0.17	0.01	0.01	0.15
Er	0.28	0.23	0.07	0.36	0.65	0.02	0.03	0.39
Tm	0.05	0.04	0.01	0.06	0.06	0.00	0.00	0.06
Yb	0.21	0.32	0.05	0.51	1.3	0.03	0.01	0.41
Lu	0.04	0.04	0.01	0.10	0.20	0.01	0.03	0.05
Hf	0.04	0.09	0.27	0.06	0.43	0.11	0.01	0.06
Ta	0.02	0.04	0.28	0.06	0.01	0.00	0.01	0.02
Pb	0.09	0.47	0.27	0.23	0.50	0.39	0.47	0.48
Th	0.06	0.22	1.1	0.38	1.7	0.02	0.04	0.72
U	0.14	0.30	0.88	0.16	0.52	0.12	0.02	0.34

Type	Carb/Stilp	Chert	Chert	Chert	Chert	Carb/Stilp	Carb/Stilp	Carb/Stilp
#scans	12	9	8	7	14	7	8	12
	clast	clast	clast	clast	clast	clast	clast	clast
	TS6-A2-34	TS6-B1-35	TS6-B2-36	TS6-C1-37	TS6-C2-38	TS6-D1-41	TS6-D2-42	TS6-F1-45
Na	244	30	100	280	451	155	766	942
Mg	40708	606	964	1538	1583	60712	67240	488600
Al	657	141	177	1592	1690	538	647	61
Ca	79385	909	1994	4501	813	126591	150865	746893
Sc	0.726	6.100	7.280	7.100	6.850	2.000	2.810	1.680
Ti	8.4	23	101	62	67	46	126	4.5
V	1.3	0.5	2.4	6.3	11.3	1.9	2.1	1.3
Cr	1.9	1.8	2.8	1.8	2.0	4.0	6.0	11
Mn	3869	717	1684	624	510	7138	9183	40896
Fe	23945	30805	52666	32084	45624	34843	49420	109244
Co	0.09	0.10	0.12	0.15	0.49	0.12	4.2	0.01
Ni	0.69	2.0	3.2	2.7	3.5	0.64	4.0	3.0
As	0.16	1.9	4.5	0.82	1.8	0.56	5.2	0.76
Rb	5.3	0.65	0.76	11	14	1.9	2.8	0.11
Sr	29	0.72	1.2	2.2	1.4	23	27	113
Y	2.7	0.46	0.34	0.47	0.29	5.6	8.3	6.7
Zr	0.82	0.32	0.21	2.5	1.8	0.59	0.94	0.08
Nb	0.03	0.03	0.02	0.63	0.67	0.06	0.25	0.04
Mo	0.03	0.16	0.29	0.02	0.05	0.01	0.03	0.16
Cs	0.63	0.08	0.13	1.3	1.4	0.19	0.39	0.02
Ba	9.3	0.42	0.54	11	8.0	2.8	6	21
La	1.7	0.36	0.26	0.24	1.4	4.9	7	5
Ce	2.9	0.81	0.78	0.55	0.65	9.2	11	7
Pr	0.31	0.08	0.06	0.05	0.04	0.97	1.2	0.88
Nd	1.3	0.27	0.28	0.25	0.10	3.8	4.2	3.1
Sm	0.28	0.04	0.03	0.06	0.06	0.64	0.89	0.67
Eu	0.10	0.01	0.00	0.08	0.01	0.16	0.25	0.20
Gd	0.33	0.07	0.07	0.07	0.07	0.60	1.01	0.59
Tb	0.05	0.01	0.02	0.01	0.04	0.10	0.12	0.08
Dy	0.30	0.05	0.05	0.06	0.06	0.73	0.97	0.84
Ho	0.07	0.02	0.00	0.02	0.01	0.18	0.25	0.15
Er	0.19	0.03	0.03	0.03	0.02	0.55	0.67	0.58
Tm	0.03	0.01	0.00	0.02	0.00	0.07	0.10	0.10
Yb	0.22	0.01	0.03	0.03	0.04	0.37	0.74	0.81
Lu	0.04	0.01	0.01	0.01	0.01	0.06	0.12	0.09
Hf	0.03	0.01	0.02	0.04	0.06	0.01	0.02	
Ta	0.00	0.02	0.01	0.01	0.01	0.01	0.02	0.00
Pb	0.24	0.07	0.12	0.26	0.36	0.66	1.7	2.0
Th	0.33	0.01	0.02	0.06	0.08	1.9	1.4	0.20
U	0.12	0.02	0.02	0.08	0.11	0.61	0.56	1.2

Onset of the Makganyene Glaciation

Type	Carb/Stilp	Chert/Carb	Stilp/Carb/Chert	Stilp/Carb	Chert	Stilp/Carb	Carb/Chert	Chert/Carb
#scans	11	21	42	55	26	45	26	34
	clast	clast	clast	clast	clast	clast	clast	clast
	TS6-F2-46	TS15-A-5	TS15-B-6	TS13-A-16	TS13-B-17	TS13-C-18	TS13-E-20	TS13-F-21
Na	243	97	1604	60	15	1063	700	16
Mg	53667	3305	4280	16787	93	43699	25579	184
Al	2287	204	5889	223	59	4426	2092	50
Ca	122455	15821	592	72166	633	187344	92239	370
Sc	1.9	2.9	3.6	2.7	3.0	3.3	3.7	1.9
Ti	67	13	15		0.6	69	183	26
V	5.8	1.5	3.8	0.6	0.3	4.2	5.7	0.4
Cr	11	1.3	2.0	1.6	1.6	3.9	8.2	1.0
Mn	8729	1580	287	11781	3.8	35439	16694	178
Fe	64695	17859	83192	104686	1278	207228	274717	4019
Co	0.87	0.07		5.6	0.16	0.06		0.03
Ni	2.0	1.7	3.06	9.6	5.0	2.5	1.5	1.1
As	0.73	0.68	0.57	27	0.66	0.16	0.11	0.30
Rb	4.3	1.1	40	0.75	0.11	22	10	0.26
Sr	30	4.5	0.58	11	0.19	34	15	1.4
Y	6.5	3.9	0.14	6.8	0.54	10	10	0.07
Zr	1.9	0.38	1.2		0.11	0.49	0.78	1.3
Nb	0.16	0.06	0.34	0.01	0.01	0.22	0.37	0.05
Mo	1.1	0.06	0.14	0.04		0.13	0.18	0.08
Cs	0.70	0.15	4.5	0.10	0.02	3.2	1.7	0.02
Ba	9.2	0.78	7.7	1.1	0.49	10	4.9	
La	3.8	0.43	0.03	4.7	2.6	7.4	2.3	0.06
Ce	7.2	0.98	0.07	5.0	8.1	12	4.5	0.08
Pr	0.76	0.16	0.01	0.60	0.74	1.3	0.57	0.01
Nd	3.1	0.64	0.03	2.5	2.7	5.3	2.8	0.03
Sm	0.64	0.20	0.02	0.52	0.48	1.1	0.66	0.01
Eu	0.27	0.12	0.01	0.28	0.10	0.51	0.46	0.01
Gd	0.76	0.34		0.68	0.47	1.1	0.94	
Tb	0.12	0.05		0.11	0.05	0.17	0.15	
Dy	0.78	0.46	0.02	0.82	0.24	1.2	1.2	0.03
Ho	0.18	0.11	0.00	0.19	0.04	0.24	0.21	0.00
Er	0.54	0.38	0.01	0.56	0.06	0.73	0.62	0.01
Tm	0.09	0.06	0.00	0.09	0.01	0.11	0.11	0.00
Yb	0.54	0.36	0.02	0.59	0.05	0.64	0.56	0.01
Lu	0.09	0.07		0.15	0.00	0.08	0.11	
Hf	0.06	0.02	0.04	0.00	0.00	0.03	0.02	
Ta	0.03	0.00	0.06			0.01	0.05	0.00
Pb	0.47	0.14	0.09	9.3	0.10	0.38	0.24	0.06
Th	0.87	0.02	0.07	0.11	0.16	0.34	0.25	0.01
U	0.38	0.03	0.20	0.00	0.02	0.06	0.11	0.01

Type	Chert/Carb	Chert/Stilp	Carb/Chert	Stilp/Carb/Chert	Chert	Chert	Stilp matrix	Stilp matrix
#scans	26	10	12	22	29	4	18	24
	clast	clast	clast	clast	clast	clast	Makganyene	Makganyene
	TS14-A-24	TS14-B-25	TS14-C-26	TS14-E-28	TS8-A-32	TS8-B-33	TS12-J-16	TS12-K-17
Na	27			1121	120	767	2901	4850
Mg	580	63	71	3197	882	356	11339	17225
Al	111	258	18	4403	518	798	11373	20127
Ca	3264	228	234	705	828	886	2077	1720
Sc	3.1			3.5	3.1	4.9	3.6	3.9
Ti	25			5.5	56	100	796	1297
V	0.64			1.2	1.7	1.0	18	28
Cr	0.99	16	16	1.6	2.7	7.0	14	23
Mn	252	7.0	2.4	306	664	46	3449	2745
Fe	5751	133	163	54256	14742	16995	209027	250118
Co	0.03	0.05	0.07			0.33	0.13	0.02
Ni	1.7			2.5	2.3	6.2	4.0	5.4
As	0.50	0.25	0.09	0.33	0.38	9.94	0.77	1.6
Rb	0.74		0.09	22	2.5	1.1	59	107
Sr	0.60	0.08		0.85	1.6	2.5	2.6	6.8
Y	0.28			0.17	0.18	0.26	1.5	1.1
Zr	0.41			0.45	0.51	36	7.8	7.9
Nb	0.05	0.00		0.17	0.12	0.07	2.1	4.5
Mo				0.07	0.28	0.28	0.48	0.65
Cs	0.15			4.1	0.28	0.23	11	18
Ba				4.7	2.9	2.0	18	40
La	0.43	0.15		0.04	0.10	179	1.2	0.62
Ce	1.1	0.18		0.10	0.24	0.38	2.8	1.3
Pr	0.13	0.06		0.07	0.03	0.09	0.31	0.16
Nd	0.37	0.09		0.05	0.07	0.34	1.4	0.71
Sm	0.06	0.07		0.01	0.05	0.06	0.32	0.16
Eu	0.02	0.01		0.01	0.02	1.1	0.10	0.06
Gd	0.08	0.02		0.04	0.04	0.02	0.30	0.18
Tb	0.01	0.00				0.02	0.03	0.02
Dy	0.08	0.01	0.01		0.03	0.06	0.21	0.15
Ho	0.00		0.00	0.01	0.00	0.01	0.05	0.03
Er	0.06			0.01	0.02	0.05	0.13	0.07
Tm	0.00			0.01		0.01	0.02	0.01
Yb	0.02		0.01	0.03	0.02	0.02	0.12	0.07
Lu	0.01		0.00	0.00	0.00	0.01	0.02	0.01
Hf				0.01	0.01	0.37	0.25	0.34
Ta	0.01			0.03	0.00	0.01	0.16	0.44
Pb	0.14			0.12	0.12	0.08	0.26	0.23
Th	0.02	0.00		0.07	0.03	0.01	1.2	1.2
U	0.01			0.12	0.01	0.09	0.56	1.3

Onset of the Makganyene Glaciation

Type	Stilp matrix + carb	Stilp	Stilp	Carb/Stilp	Stilp	Stilp/Carb	Stilp/Carb	Stilp/Carb
#scans	18	41	63	41	27	30	33	36
	Makganyene	Makganyene	Makganyene	Makganyene	Makganyene	Makganyene	Makganyene	Griquatown
	TS12-L-18	TS15-G-11	TS15-H-12	TS13-D-19	TS14-D-27	TS14-F-29	TS8-F-37	TS15-C-7
Na	3748.34	776	95	1910	195	2787	2582	591
Mg	28558	2515	312	28657	490	14436	20914	35387
Al	14608.06	1969	345	8251	351	12322	11059	2515
Ca	64241.28	5397	424	112173	434	37363	216076	158736
Sc	4.58	1.3	0.31	3.0	4.1	5.0	5.5	7.3
Ti	80.61	294	59	404	45	1098	2024	223
V	20.05	21	28	8.4	1.3	4.2	18	1.8
Cr	26.95	8.1	22	8.2	1.2	3.6	38	8.5
Mn	11595.55	663	47	13320	108	3343	19037	15211
Fe	278010.3	560053	592058	220158	27168	161896	260922	156474
Co	0.41	0.20	0.34	0.07	0.04		2.3	0.05
Ni	6	5.3	6.4	3.8	1.7	4.7	12	1.8
As	4.58	2.1	4.8	0.76	3.6	0.42	4.9	0.32
Rb	70.31	8.1	1.6	35	2.2	52	66	12
Sr	14	2.7	0.75	19	1.3	7.9	77	36
Y	6.11	2.6	0.30	12	0.31	6.4	16	16
Zr	3.69	3.1	0.83	1.8	0.48	14	16	0.82
Nb	1.464	0.94	0.26	1.13	0.16	1.5	4.4	0.31
Mo	1.16	0.24	0.18	0.53		0.76	0.23	0.12
Cs		1.5	0.28	6.3	0.33	7.4	11	1.1
Ba	26.9	3.3	1.43	10	1.6	12	56	6.9
La	1.843	1.6	0.37	3.5	0.14	2.5	13	2.4
Ce	3.82	3.0	0.69	6.3	0.37	4.5	21	5.5
Pr	0.527	0.33	0.08	0.83	0.03	0.59	2.3	0.71
Nd	2.42	1.5	0.22	3.9	0.19	2.4	9.6	3.2
Sm	0.608	0.32	0.04	1.02	0.03	0.57	2.1	0.95
Eu	0.368	0.10	0.02	0.68	0.01	0.24	0.69	0.49
Gd	0.661	0.30		1.5		0.77	1.9	1.4
Tb	0.108	0.05	0.01	0.19		0.12	0.34	0.22
Dy	0.662	0.31	0.04	1.5	0.02	0.78	2.0	1.8
Ho	0.182	0.08	0.01	0.31	0.01	0.17	0.45	0.46
Er	0.485	0.23	0.02	0.96	0.03	0.61	1.3	1.4
Tm	0.054	0.03	0.01	0.13	0.01	0.09	0.19	0.24
Yb	0.535	0.17	0.02	0.89	0.07	0.46	1.1	1.7
Lu	0.0814	0.03	0.01	0.14		0.08	0.21	0.28
Hf	0.245	0.08	0.03	0.11	0.00	0.32	0.36	0.03
Ta	0.363	0.05	0.01	0.13		0.11	0.36	0.02
Pb	0.561	0.73	0.77	0.60	0.32	0.25	2.7	0.30
Th	0.563	0.58	0.21	0.41	0.07	1.1	2.9	0.17
U	1.03	0.15	0.12	0.46	0.04	0.54	0.52	0.06

Onset of the Makganyene Glaciation

Type	Stilp/Carb	Stilp/Carb	Stilp/Carb	Carb	Stilp/Carb	Stilp	Stilp/Carb	Stilp/Carb
#scans	49	35	39	9	45	24	42	38
	Griquatown	Griquatown	Griquatown	Griquatown	Griquatown	Griquatown	Griquatown	Griquatown
	TS15-D-8	TS15-E-9	TS15-F-10	TS11-D-44	TS11-E-45	TS11-F-46	TS9-A-49	TS9-B-50
Na	1489	27084	4205	22	422	1633	5247	970
Mg	5358	88455	19998	1170	14687	16430	37820	15896
Al	5822	122394	21164	24	5656	9998	31653	8720
Ca	9012	10229	24972	433899	9493	205505	27758	15358
Sc	4.0	51	7.2	1.6	3.0	8.2	10	4.4
Ti	379	11628	310	1.1	526	1008	977	881
V	11	86	15	0.15	12	16	54	20
Cr	30	19	29	3.2	19	36	67	29
Mn	866	4860	3115	8062	17299	10119	22974	13992
Fe	198503	1392710	236799	15138	249317	187719	510813	238951
Co			0.05	2.0	0.31	1.7	1.5	0.23
Ni	4.3	43	6.5		5.0	8.1	22	7.4
As	0.88	7.7	1.8	0.30	2.9	3.6	8.6	3.7
Rb	31	701	102	0.05	16	50	145	38
Sr	2.96	14	11.67	43	4.7	67	15	7.7
Y	4.8	4.0	6.9	22	5.0	16	9.0	8.0
Zr	9.5	20	18	0.14	6.2	13	13	18
Nb	0.79	21	2.2		0.84	2.0	3.3	1.4
Mo	0.42	0.58	0.23	0.06	0.13	0.29	0.15	0.11
Cs	5.7	184	19	0.01	2.3	6.8	43	5.8
Ba	6.6	119	41	0.34	19	38	144	38
La	2.8	2.4	3.6	16	3.0	18	6.3	6.4
Ce	6.1	5.3	6.8	25	4.0	24	9.1	11
Pr	0.73	0.67	0.89	2.6	0.48	2.7	1.1	1.2
Nd	3.4	3.2	3.95	9.4	2.0	10	4.3	5.1
Sm	0.73	0.61	0.87	1.7	0.49	1.9	1.1	1.1
Eu	0.20	0.20	0.27	0.55	0.14	0.68	0.32	0.27
Gd	0.74	0.60	0.90	2.1	0.55	2.2	1.1	0.98
Tb	0.11	0.18	0.13	0.33	0.08	0.36	0.17	0.16
Dy	0.74	0.47	0.92	2.5	0.62	2.1	1.4	1.0
Ho	0.14	0.13	0.19	0.58	0.12	0.40	0.23	0.20
Er	0.34	0.25	0.61	2.0	0.41	1.3	0.84	0.67
Tm	0.06	0.06	0.08	0.31	0.07	0.17	0.09	0.08
Yb	0.32	0.38	0.50	2.1	0.45	1.0	0.67	0.67
Lu	0.04	0.03	0.07	0.39	0.08	0.17	0.12	0.12
Hf	0.17	0.44	0.59	0.02	0.18	0.29	0.62	0.43
Ta	0.06	0.51	0.43	0.01	0.08	0.18	0.28	0.10
Pb	0.42	1.4	0.56	0.17	0.26	2.3	1.2	0.45
Th	0.85	2.4	1.4	0.10	0.71	2.3	1.5	1.6
U	0.33	2.2	0.87	0.00	0.17	0.27	1.0	0.41

Onset of the Makganyene Glaciation

Type	Stilp/Carb	Stilp/Carb	Stilp/Carb	Stilp/Carb	Carb/Stilp/Chert/Opq	Carb/Stilp/Chert/Opq	Stilp	Chert/Carb/Stilp
#scans	40	28	43	36	21	46	18	25
	Griquatown	Griquatown	Griquatown	Griquatown	Griquatown	Griquatown	Griquatown	Griquatown
	TS9-C-51	TS9-D-52	TS9-E-53	TS9-F-54	TS17-A-62	TS17-B-63	TS17-C-64	TS17-D-65
Na	1295	1130	554	500	1111	361	422	1657
Mg	18127	19211	17236	19720	40311	1111	34262	5076
Al	11159	9334	5144	5956	4510	211	1329	8228
Ca	53073	67242	26385	31276	175919	3036	199476	2619
Sc	4.1	4.4	3.6	3.8	6.8		6.1	2.0
Ti	669	726	602	538	320	88	4.7	948
V	19	18	11	12	12	34	0.67	8.2
Cr	32	36	23	27	7	34	3.5	5.2
Mn	11695	17999	19637	20871	19639	417	17559	362
Fe	219174	281168	261452	272395	398482	632607	165512	185195
Co	0.19	1.4	0.20	0.51	0.05			
Ni	8.5	7.3	4.8	4.1	5.8	4.6		2.2
As	2.0	3.5	2.3	3.0	1.0	3.2	0.19	0.66
Rb	56	45	24	20	24	1.2	4.4	34
Sr	19	26	11	13	43	3.9	31	3.1
Y	6.8	8.5	8.8	7.8	21	1.1	29	3.5
Zr	11	11	21	9.4	3.4	4.9	0.80	7.1
Nb	1.2	1.1	0.89	0.87	0.58	0.28	0.07	1.4
Mo	0.11	0.24	0.04	0.08	0.14	0.14	0.10	0.35
Cs	8.3	6.5	2.9	2.2	3.4	0.31	0.68	6.2
Ba	57	56	19	20	9.3	16	3.7	9.5
La	5.2	6.1	5.3	6.1	3.8	0.56	2.9	1.8
Ce	9.1	10.0	7.3	8.1	7.9	1.0	6.2	3.5
Pr	0.96	1.0	0.86	0.94	1.1	0.10	1.0	0.50
Nd	3.9	4.4	3.8	4.2	4.5	0.40	5.4	2.5
Sm	0.78	0.99	0.89	0.80	1.3	0.09	1.6	0.59
Eu	0.25	0.32	0.25	0.22	0.56	0.04	0.92	0.14
Gd	0.82	0.99	0.94	0.89	1.5	0.10	2.2	0.49
Tb	0.12	0.13	0.16	0.13	0.33	0.01	0.42	0.08
Dy	0.96	1.0	1.1	1.0	2.1	0.11	3.4	0.54
Ho	0.19	0.22	0.25	0.21	0.58	0.04	0.88	0.10
Er	0.55	0.72	0.70	0.66	1.7	0.10	2.8	0.32
Tm	0.10	0.11	0.11	0.10	0.30	0.03	0.47	0.03
Yb	0.64	0.68	0.90	0.67	2.2	0.20	3.4	0.20
Lu	0.08	0.14	0.16	0.12	0.41	0.03	0.56	0.03
Hf	0.33	0.33	0.56	0.25	0.06	0.06	0.03	0.10
Ta	0.12	0.13	0.07	0.08	0.02	0.01	0.01	0.04
Pb	0.48	0.79	0.35	0.48	0.46	276	0.36	0.19
Th	1.0	1.0	0.99	1.6	0.18	0.29	0.07	0.45
U	0.24	0.24	0.22	0.20	0.09	0.12	0.03	0.20

Type	Chert/Carb/Stilp	Chert/Carb/Stilp
#scans	23	18
	Griquatown	Griquatown
	TS17-E-66	TS17-F-67
Na	1684	124
Mg	399	515
Al	436	625
Ca	278	368
Sc	3.2	2.5
Ti	8.1	20
V	0.89	0.47
Cr	1.6	3.8
Mn	92	90
Fe	9178	8160
Co	0.11	0.09
Ni		1.2
As	0.62	0.33
Rb	2.3	2.0
Sr	0.43	1.0
Y	0.16	0.10
Zr	0.26	0.21
Nb	0.22	0.03
Mo	0.20	0.05
Cs	0.44	0.38
Ba	0.58	0.47
La	0.05	0.23
Ce	0.26	0.10
Pr	0.02	0.03
Nd	0.09	0.39
Sm	0.01	0.01
Eu		0.02
Gd	0.06	0.04
Tb		0.01
Dy		0.01
Ho	0.02	0.01
Er	0.03	0.01
Tm		0.00
Yb	0.00	0.01
Lu	0.00	
Hf		0.02
Ta	0.00	0.01
Pb	0.33	0.17
Th	0.01	0.01
U	0.01	0.04

8.6 Appendix VI - Laser spots

TS6
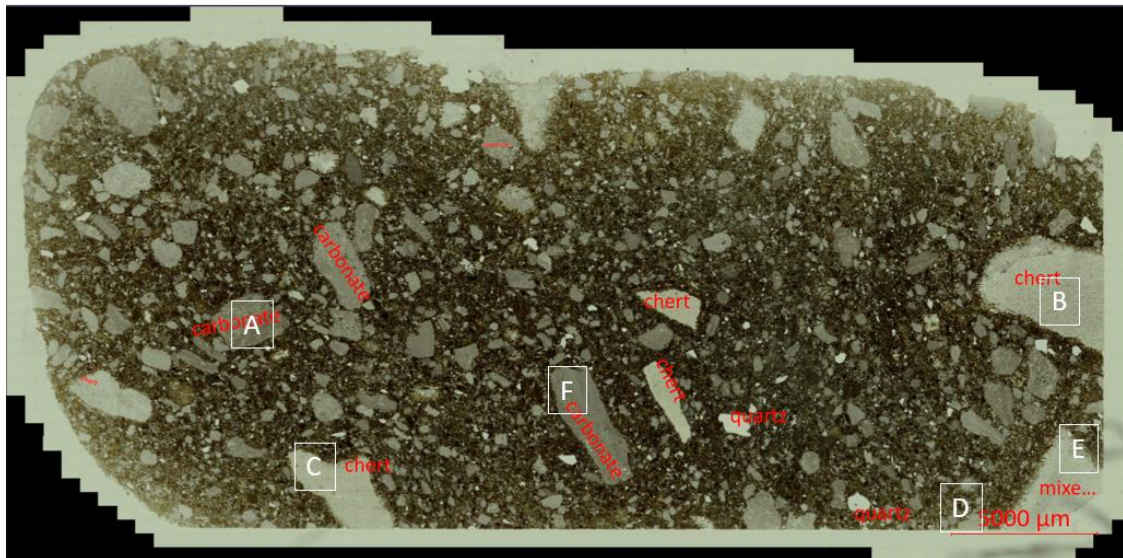
TS8
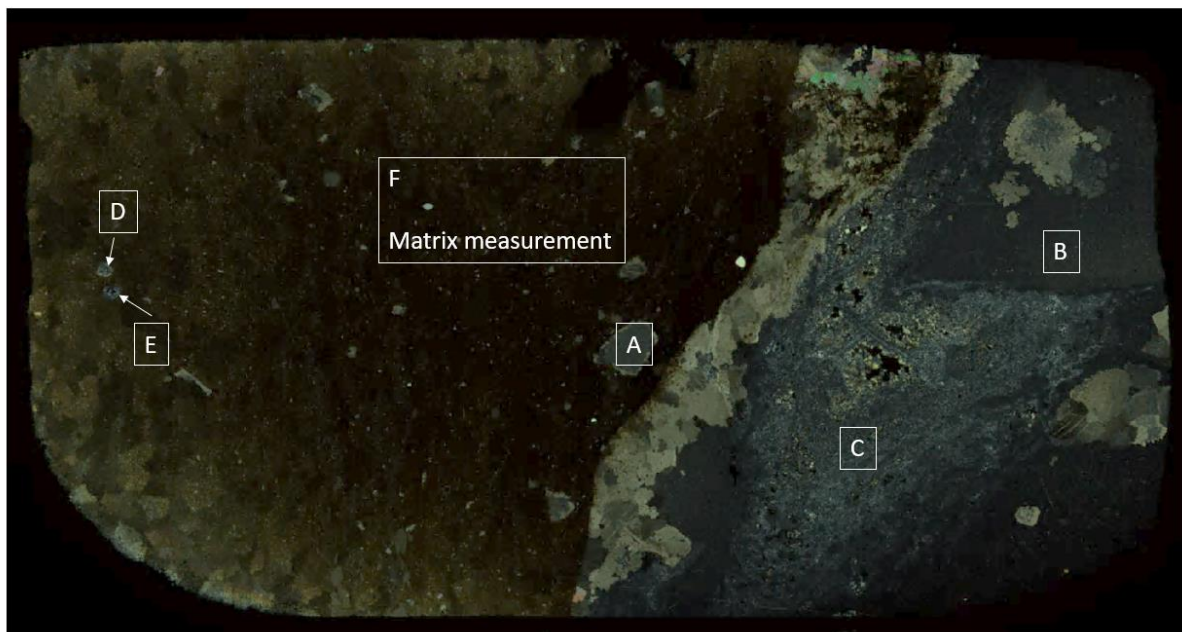
TS9

TS11

TS12

TS13

TS14

TS15

TS17